



Electrostatic Simulation Methodology for Capacitive Touch-Screen Panels

Submitted by: Barry Cannon, BSc Applied Physics

In pursuit of the award: Master of Engineering by Research

Supervisor: Dr. Conor Brennan
School of Electronic Engineering
Dublin City University

July, 2014

DECLARATION

I hereby certify that this material, which I now submit for assessment on the programme of study leading to the award of MEng by research is entirely my own work, and that I have exercised reasonable care to ensure the work is original, and does not to the best of my knowledge breach any law of copyright, and has not been taken from the work of others save and to the extent that such work has been cited and acknowledged within the text of my work.

Signed : _____

Candidate Name: Barry Cannon

ID No.: 57520646

Date: 07/07/2014

ACKNOWLEDGMENTS

I wish to thank Cmdr. Tim Quigley of Sister Cities International for all of his hard work in establishing the first of the Pat McMahon Scholarship Series. I would like to thank Alex Gourevitch of Cypress Semiconductor for guidance during my internship. I'd like to extend a sincere thank you to Mark Finn and the entire staff of Cypress Semiconductor for a rich and educational internship. Finally, I would like to thank Dr. Conor Brennan for his expertise, encouragement and constant enthusiasm throughout the course of this project.

TABLE OF CONTENTS

SECTION TITLE	PAGE NUMBER
Declaration of Authorship	2
Acknowledgments	3
Table of Contents	4
Abstract	6
Abbreviations	8
Symbols	8
1. Introduction & Background:	
1.1 Thesis Introduction	9
1.2 Introduction to Electromagnetism	11
1.3 The Finite Element Method	15
1.4 The Method of Moments	18
1.5 Literature Review	20
2. Sensor Design:	
2.1 The Touch-Sensor Circuit	23
2.2 Features of Sensor Design	24
2.3 Critical Parameters and Metrics	27
2.4 ITO Patterns	29
2.5 Stack-Ups	32
3. Experiments:	
3.1 Parallel Plate Capacitor Verification	34
3.2 Stack-Up Screening Comparison	38
3.3 ITO Pattern Screening Comparison	49
3.4 FEM/MOM Comparison	65
3.5 Simulation Size Comparison	66

3.6 Design of Experiments Methodology	72
3.7 Moving Finger Study	84
4. Conclusions	90
5. References	93

ABSTRACT

In recent years, projected capacitance has become by far the most used method of touch-screen sensing in the consumer electronics industry. Touch-screen panels (TSPs) consist of varying transparent layers of lens, substrate, adhesive and indium-tin-oxide (ITO) electrodes. ITO has become the material of choice for manufacturing TSPs due to its high conductivity and high transparency. A touch is detected when there is a change in mutual capacitance between transmitting and receiving electrodes embedded the touch-screen. As a core feature in all aspects of modern electronics, there is a constant need to reevaluate and customize existing designs. Utilizing computer simulations allows a designer to predict the behavior of a design without building the physical sensor. Simulations have 3 main uses for touch-screen developers. (1) Building and testing new prototype designs, (2) optimization of existing designs and (3) testing the linearity and uniformity of existing designs due to vendor process variation. This thesis asks the questions: “What key metrics characterize a good TSP?” and “How can TSP designs be optimized using computer simulations?”

This thesis contains a literature review of recent simulation approaches and review of the rise of projected capacitance technology in the touch-screen industry. The main focus of this thesis is the electrostatic simulation of touch-screen sensors. The relevant physics of electromagnetism is introduced and the dominant mathematical methods of simulation are reviewed and compared - namely the Finite Element Method (FEM) and the Method of Moments (MOM). Both these methods are used in experimental studies. The operation of a typical sensor and the mechanism of mutual capacitance is explained and accompanied by an equivalent circuit diagram. Important features of sensor design are introduced such as typical patterns, stack-ups, and trace routes. Simulations produce a capacitance matrix. From this matrix critical parameters which characterize sensor performance are derived such as signal-to-noise ratio (SNR) and change in mutual capacitance (ΔC_m).

Several experimental studies of contrasting pattern designs and stack-ups are conducted in order to demonstrate optimization of touch-screen designs. Within each simulation, features of the design are parameterized in order to perform parametric sweeps. These sweeps can include layer thickness, relative permittivity of a layer, sensor pitch and size of a specific geometric feature. In each case, several parameters of the design are varied and the effect on the capacitances are recorded. From these values the critical parameters of the sensor are determined along with the overall performance

of the sensor. A design-of-experiments (DOE) methodology is also described in order to demonstrate the optimal simulation for a touch-screen design with an exhaustive number of variable parameters.

This thesis also examines some of the implications of limited computational resources and its effect on solution time and convergence. Methods of decreasing the computational load will also be discussed.

In summary, this body of work serves as a complete guide in the designing, running and analysis of electromagnetic simulations for modern TSPs.

ABBREVIATIONS

FEM	– Finite Element Method
MOM	– Method of Moments
TSP	– Touch-Screen Panel
DOE	– Design of Experiments
ITO	– Indium-tin-oxide
SNR	– Signal-To-Noise Ratio
BC	– Boundary Condition
FPCB	– Flexible Printed Circuit Board
FEM-BEM	– Finite Element Method Boundary Element Method
FEM-DCBI	– Finite Element Method Dirichlet Boundary Condition Method
GG	– Glass-On-glass
SOL	– Sensor-On-Lens
GF	– Glass-Film
GFF	– Glass-Film-Film

SYMBOLS

ΔC_m	= Change in mutual capacitance between Rx and Tx electrodes
C_m	= mutual capacitance of untouched touch-screen panel
C_m'	= Mutual capacitance of touched electrodes touch-screen panel
C_{pTX}	= Parasitic capacitance between the Tx electrode and common ground
C_{pRX}	= Parasitic capacitance between the Rx electrode and common ground
C_{fTX}	= Capacitance between the Tx electrode and finger
C_{fRX}	= Capacitance between the Rx electrode and finger
SNR_{TOUCH}	= Signal-to-noise ratio in touched case
$SNR_{DISPLAY}$	= Signal-to-noise ratio in untouched case
τ	= RC time constant

CHAPTER 1

INTRODUCTION & BACKGROUND

1.1 THESIS INTRODUCTION

In the year 2014, touch-screens are ubiquitous in consumer electronics. Phones, tablets, pay-stations, games consoles, watches, laptops and computers all use this technology. There is a constant stream of new applications emerging for consumption. This places a high strain on designers to constant revamp and refine their touch-screen designs as applications come in a vast range of display configurations and sizes. It is therefore, extremely beneficial and desirable for an engineer to be able to build, test and roll-out new designs as quickly and efficiently as possible. At the same time, producing prototype TSPs requires correspondence with a vendor, turn around time, a sample limitation and a fee per panel and relying on these test panels alone results for an extremely slow production flow. This thesis demonstrates the advantage of using electrostatic simulation methodologies to design, modify and test TSP designs in a virtual environment. The aim being that these simulations will be accurate and fast. It also identifies several figures of merit that characterize a good TSP design which can be determined using the capacitive matrix obtained from electrostatic simulations.

To begin, there will be a brief introduction chapter which will cover basic electromagnetism and the most widely used simulation methods of the present day – the “Finite Element Method” (FEM) and the “Method of Moments” (MOM). These are numerical methods which are designed to break down a large domain into many small “elements”, solving the governing equation and creating a full solution through interpolation functions. There will also be a literature review where the most recent work on touch-screens and electromagnetic simulation methodologies will be discussed.

Chapter 2 will cover “sensor design”. This includes the basic components of a TSP and how the sensing mechanism is achieved and sent to the chip, the sensor circuit of electrodes which describes how a finger draws charge away from the panel in order to trigger a response at a location, the figures of merit and capacitances that characterize each sensor, the prevalent electrode patterns used in consumer electronics, and the various stack-up layers that comprise the full sensor unit.

The simulation chapter will span the entire set of simulations investigated by this work. There is a

huge variety of experimental approaches to take. The selection of simulation methodology depends on a number of factors. These could be customer expectations, time constraints, vendor processing variations, non-linearity testing, capability testing, redesigning or numerical model building. Firstly, the capability to simulate should be assessed. This is done by creating two parallel-plate capacitor models – one in an FEM solver, another in an MOM solver. Both verify the integrity of the numerical methods.

The “screening” methodologies is then presented with respect to differing stack-ups on an identical TSP pattern using FEM. This shows the effect of varying stack-up layer thicknesses on the sensitivity of a sensor. In contrast, the next section demonstrates how apply this screening analysis to TSP pattern parameters such as sensor pitch, deletion and bridge width, again using FEM. The FEM/MOM section gives a comparison between identical patterns sweeps carried out by FEM and MOM techniques, the former using COMSOL multiphysics and the later using Ansys Q3D software packages. Again, it is shown that there is a high degree of agreement between the two techniques. However, it is not possible to draw a reasonable comparison between the two with respect to solution time. This is due to contrasting computer resources at the time this work was carried out – as access to high-end FEM computing resources was disabled, access to MOM resources on reasonable computing resources was gained. This made parallel FEM/MOM simulations impossible. However, the comparison is useful in noting the agreement and in illustration.

Until this point, all simulations have been a 3x3 cell miniature format. The next approach is to vary the number of unit cells simulated. As more and more cells are added to the simulation, the smaller the difference between the actual physical sensor and the simulation model becomes. The expectation is that adding more cells will improve the convergence of the simulation at the cost of solution time. A 5x5 is built and compared to the previously used 3x3 and an additional 1x1 matrix which utilizes periodic boundary conditions. The aim of the 1x1 is to provide an extremely quick result. While it is flawed in that the small simulation domain introduces a large error in the measurement of parasitic and finger capacitances, it is shown that the measurement of sensitivity is in good agreement with the much larger models. Demonstrating its viability in a time sensitive situation.

While some panel designs are simple, others are extremely complex and have a many layer thicknesses, permittivities and panel dimensions which could be varied over a large range of values. The “Design of Experiments” (DOE) section explores the DOE methodology for a fractional-

factorial design applied to a TSP simulation. Instead of running the full range of possible experiments for each factor over many levels, a carefully designed but limited set of experiments is conducted. Data collected from these experiments is then used to create numerical models which predict the behavior of the sensor for any set of input factors. This methodology has the highest time-saving potential, as full-factorial simulations can run for days or weeks on end.

The moving finger section shows the effect of finger location on the sensitivity of the sensor. As the amount of charge drawn from the unit-cell depends on the location of the touch, sensitivity vs location data can be extremely helpful if supplied as a tuning parameter for a touch sensing algorithm. This methodology demonstrates how to utilize axisymmetry in order minimize the required simulation time. This is due largely to the fact that most TSP unit cells have a quarter cell symmetry which can be exploited by extrapolating results to mirrored location within the unit cell.

In the final chapter findings, unique contributions and possible future work will be outlined.

1.2 INTRODUCTION TO ELECTROMAGNETISM

The capacitance between two conducting bodies is the ability of those bodies to store an electrical charge and is a property of any body that can be electrically charged – including humans. This is what allows a finger to draw charge from a TSP and cause a change in mutual capacitance between the conductors imbedded in it. This chapter will establish the basic mathematics of capacitance before the finite element method (FEM) and method of moments (MOM) are explored in later chapters.

The capacitance C is defined as:

$$C = \frac{Q}{V} \quad (1.1)$$

where C is the capacitance Q is the charge and V is the scalar potential of the charged object. The capacitance of a simple parallel-plate capacitor of area A and separation d can be calculated. If a charge of $+Q$ and $-Q$ are placed on the surfaces of the plates respectively, the charge will separate uniformly over the two surfaces [1]. The surface charge density is therefore given by:

$$\sigma = \frac{Q}{A} \quad (1.2)$$

and provided that the ratio of A/d is sufficiently large so as to approximate two infinite parallel planes each plate will produce an electric field of $E = (\sigma/2\epsilon_0)$ at the surface of *each* plate. Giving rise to a field of $E = +(\sigma/\epsilon_0)$ outside the positive plate, a field of $E = -(\sigma/\epsilon_0)$ outside the negative plate and a field of $E = 0$ inside the two parallel plates. Field lines either side of each plate will cause a field cancellation effect resulting in a field of:

$$E = \frac{Q}{A \epsilon_0} \quad (1.3)$$

and given that the potential:

$$V = \int_0^l E \cdot dl \quad (1.4)$$

therefore:

$$V = \frac{Q \cdot d}{(A \epsilon_0)} \quad (1.5)$$

giving finally:

$$C = \epsilon_0 \frac{A}{d} \quad (1.6)$$

assuming a relative permittivity corresponding to air, $\epsilon_r = 1$. In general for a dielectric insulator between the plates the capacitance can be given by:

$$C = \epsilon_0 \epsilon_r \frac{A}{d} \quad (1.7)$$

Equation (1.7) demonstrates that capacitance is a purely geometrical quantity which is only affected by geometry and separation.

The simulations used in this work deal only with electrostatic case. Therefore the governing equations are not affected by the passage of time. The activation of electrodes is a binary sequential process. In each simulation two “snapshots” of the capacitor are taken – one of the Tx electrode fully charged at 1 volt about to discharge to the Rx electrode, and one of the Rx electrode fully charged after having completed a charge transfer with Tx. Therefore, the relevant governing equations for electrostatics must be considered.

$$\nabla \times E = 0 \quad (\text{Faraday's law of electrostatics}) \quad (1.8)$$

where E is the electric field intensity.

$$\nabla \times \mathbf{H} = \mathbf{J} \quad (\text{Maxwell-Ampère law}) \quad (1.9)$$

where H is the magnetic field intensity.

$$\nabla \cdot \mathbf{J} = 0 \quad (\text{Equation of continuity}) \quad (1.10)$$

where j is the electric current density.

The electrostatic field can be represented in such a way consistent with Faraday's law of electrostatics give by:

$$\mathbf{E} = -\nabla V \quad (1.11)$$

and given that:

$$\nabla \cdot \mathbf{D} = \sigma \quad (\text{Gauss's law}) \quad (1.12)$$

and the relative constitutive relation:

$$\mathbf{D} = \epsilon \mathbf{E} \quad (1.13)$$

one obtains:

$$-\nabla \cdot (\epsilon \nabla V) = \sigma \quad (1.14)$$

which is the famous *Poisson equation*, the second order differential equation governing V . FEM uses variational methods to minimize an error function in order to produce a solution for a quantity of interest in each sub-domain or “element” of the problem space. In the case of electrostatics that quantity of interest is the scalar potential which is governed by Poisson's equation, which can be rewritten for convenience as:

$$\nabla^2 V = -\sigma/\epsilon_0 \quad (1.15)$$

where ρ is the charge density and ϵ_0 is the permittivity of free space. Once the potential is computed throughout space it can be used to compute the capacitance between electrodes. For example an approximate expression for the mutual capacitance between two finite parallel plates is given by:

$$C = \epsilon_0 \epsilon_r A/d \quad (1.16)$$

However, this equation does not allow for the presence of fringing fields or orientation of Tx and Rx electrodes in TSPs because it represents an ideal case. There is no convenient geometry present in an ITO pattern that would allow us to simplify (1.1). These are two dominant numerical techniques implemented by modern electrostatic solvers – the finite element method (FEM) [2] and

the method of moments (MOM) [2]. An FEM or MOM solver must therefore be used to compute a scalar potential solution from which a capacitance matrix can be formed. This matrix consists of parasitic, mutual and finger capacitances which are used to derive critical metrics used to assess the performance of the sensor.

The FEM and MOM solvers also apply required Dirichlet and Neumann boundary conditions to the problem space. The Dirichlet boundary condition specifies the value that a solution needs to take on the boundary of the domain. For a partial differential equation of the form:

$$\nabla^2 V + V = 0 \quad (1.17)$$

the Dirichlet boundary condition on a domain Ω take the form of:

$$V(\mathbf{x}) = f(\mathbf{x}) \quad (1.18)$$

where f is a known function defined on the boundary.

The Neumann boundary condition specifies the value that the derivative of a solution needs to take on the boundary of the domain. It is given by:

$$\frac{\delta V}{\delta \mathbf{n}}(\mathbf{x}) = f(\mathbf{x}) \quad (1.19)$$

the normal derivative is defined as:

$$\frac{\delta V}{\delta \mathbf{n}}(\mathbf{x}) = \nabla V(\mathbf{x}) \cdot \mathbf{n}(\mathbf{x}) \quad (1.20)$$

In the subsequent 1x1 simulation in chapter 3.5 the Neumann boundary condition is set to 0 and the boundary is moved inwards to the edge of the unit cell. This gives a mirror symmetry which allows for simulation of an infinite array.

1.3 THE FINITE ELEMENT METHOD

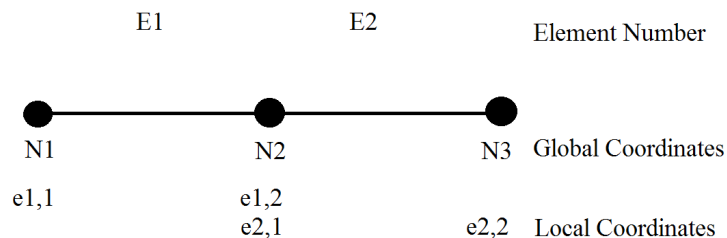
This section will briefly describe the FEM procedure. As can be seen in [jin] the Raleigh-Ritz and Galerkin methods describe the minimization of a particular trial function over an entire domain. These are trial functions which minimize a residual term in order to predict a field quantity of a domain. However, in FEM these methods are used to construct a trial-function in the form of a differential equation consisting of a combination of interpolation functions defined over many sub-domains known as elements which in turn comprise the entire domain.

The finite element method has four basic steps:

1. Discretization or subdivision of the domain.
2. Selection of the interpolation functions.
3. Formulation of the system of equations.
4. Solution of the system of equations.

Discretization:

The discretization stage is critical because it affects the computational storage requirements, solution time and accuracy of the simulation. In 1D, the line is divided into equal line segments



where each “element” is comprised of two “nodes”. Note that it is not always necessary to divide the domain into equal segments. This is the simplest case. Discretization includes the assignment of both local

Fig 1.1 Global and local coordinate systems in 1D.

and global coordinates. Local coordinates refer to the numbering of the nodes within the element whereas global coordinates refer to the numbering of the node in the entire domain. Proper numbering of the nodes is important in order to limit the bandwidth of the tridiagonal matrix used to solve the system of equations. Figure 1.1 gives the discretization of a 1D domain consisting of two elements. Figure 1.2 gives a typical 3D tetrahedral element.

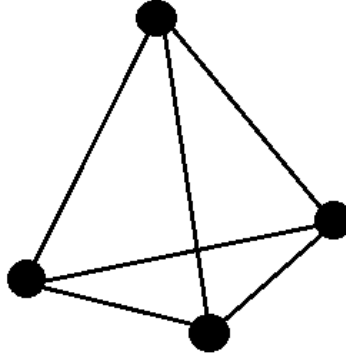


Fig. 1.2 3D tetrahedral element.

Selection of the interpolation functions:

The interpolation function provides an approximation of the unknown solution in an element. Higher order functions (quadratic, cubic) give better results. Since the problem is being solved over small sub-domains, lower order interpolation functions (linear) can be used, leading to simpler formulation of equations compared to the Ritz/Galerkin methods alone. With the order of the function selected, this expression can be derived. In the context of potential V :

$$\tilde{V} = \sum_{(j=1)}^n N_j^e V_j^e = \{N^e\}^T \{V^e\} = \{V^e\}^T \{N^e\} \quad (1.21)$$

where \tilde{V} denotes the trial function to be solved, n is the number of nodes in the element, V_j^e is the value of V at node j of the element, and N_j^e is the interpolation function for node j . It is important to note the the interpolation functions are only non-zero while inside the element and that they vanish outside the element.

Formulation of the system of equations:

We can use the Ritz or Galerkin methods to construct the system of equations. For arguments sake let us examine the Ritz method. The Ritz functional is given by:

$$F(\tilde{V}) = \sum_{e=1}^M F^e(\tilde{V}^e) \quad (1.22)$$

where M is the number of elements in the domain and:

$$F_{(\tilde{V}^e)}^e = \frac{1}{2} \int_{\Omega^e} \tilde{V}^e L \tilde{V}^e d\Omega - \int_{\Omega^e} f \tilde{V}^e d\Omega \quad (1.23)$$

where L is known as the Lagrangian operator, Ω is the domain and $F_{(\tilde{V}^e)}^e$ is the functional to be minimized for each element. This expression can be combined with the trial function (1.21) and expressed in matrix form given by:

$$F_{(\tilde{V}^e)}^e = \frac{1}{2} \{V^e\}^T [K^e] \{V^e\} - \{V^e\}^T \{b^e\} \quad (1.24)$$

where $[K^e]$ is an $n \times n$ matrix and $\{b^e\}$ is an $n \times 1$ column vector given by:

$$K_{ij}^e = \int_{\Omega^e} f N_i^e L N_j^e d\Omega \quad (1.25)$$

and

$$b_i^e = \int_{\Omega^e} f N_i^e d\Omega \quad (1.26)$$

By substituting (1.24) into (1.22) and by using the fact that the operator L is self-adjoint, and by performing the summation and adopting global node numbering, the function can be rewritten as:

$$F_{(\tilde{V}^e)}^e = \frac{1}{2} \{V\}^T [K] \{V\} - \{V\}^T \{b\} \quad (1.27)$$

where $[K]$ is an $N \times N$ symmetric matrix, N is the total number of nodes, $\{V\}$ an $N \times 1$ unknown vector whose elements are the unknown expansion coefficients, and $\{b\}$ an $N \times 1$ known vector. The system of equations is then obtained by enforcing that $\delta F = 0$. Rewriting the result in matrix form gives:

$$[K] \{V\} = \{b\} \quad (1.28)$$

Solution of the system of equations:

In order to solve for the potential V at each node equation (1.28) needs to be rearranged. In order to solve for V , K must be inverted.

$$\{V\} = [K]^{-1} \{b\} \quad (1.29)$$

K is a sparse tridiagonal matrix for which there exist techniques to optimize its inversion. This optimization is an important feature of any FEM solver, but will not be discussed here. For a complete in depth explanation of the finite element method in electromagnetism, see [2].

An FEM solver discretizes the entire volume and describes interactions between unknown field values via a sparse matrix. In addition there is a need to apply suitable boundary conditions at the edge of the computational domain in order to control truncation effects.

1.4 THE METHOD OF MOMENTS

The method of moments is closely related to the finite element method. Like FEM, it transforms the governing equation into a matrix equation that can be solved computationally. The main difference is that instead of a differential formulation, MOM uses an integral formulation for the governing equation. It has become more relevant in recent years due to the rise of fast solvers such as the FFT-based method, the adaptive integral method and the fast multipole method which all serve to reduce the computational load. This section will briefly address the implementation of MOM as it pertained to electrostatic problems.

The method of moments also has four basic steps:

1. Formulation of the problem in terms of an integral equation.
2. Represent the unknown quantity using a set of basis functions.
3. Convert the integral equation into a matrix equation using a set of testing functions
4. Solve the matrix equation and calculate the desired quantities.

For an electrostatic problem, the goal is usually to find the the electric charge distribution on the charged object. Once the charge density is found the capacitance can be solved for. Using the Green's function the governing electrostatic equation can be represented as:

$$V(\mathbf{r}) = \int \int_S G(\mathbf{r}, \mathbf{r}') \sigma(\mathbf{r}') dS' \quad (1.30)$$

where $V(\mathbf{r})$ is the total potential due to the charge distributed on the conductor. $G(\mathbf{r}, \mathbf{r}')$ is the Green's function and S is the surface of the conductor. $V(\mathbf{r})$ is a constant for a metallic surface, therefore:

$$V = \int \int_S G(\mathbf{r}, \mathbf{r}') \sigma(\mathbf{r}') dS' \quad (1.31)$$

and V is a known constant.

Represent the unknown quantity using a set of basis functions:

Dividing the surface S into small triangular patches and assuming a constant surface charge density the set of linear equations can be obtained:

$$\sum_{n=1}^N S_{mn} \sigma_n = b_m \quad (1.32)$$

where σ_n denotes the surface charge density on the n^{th} element. S_{mn} and b_m are given by:

$$S_{mn} = \int \int_{S_m} \int \int_{S_n} G(\mathbf{r}, \mathbf{r}') dS' dS \quad (1.33)$$

and

$$b_m = \Delta_m V \quad (1.34)$$

where S_n and S_m denote the n^{th} and m^{th} patches. Δ_m is the area of the m^{th} patch. The double integrals can be evaluated at which point equation (1.32) can be solved for σ_n . Once solved for, the total charge on the conductor can be solved for as:

$$Q = \sum_{n=1}^N \sigma_n \Delta_n \quad (1.35)$$

with the capacitance given by:

$$C = \frac{Q}{V} \quad (1.36)$$

In contrast to FEM, MOM only discretizes the boundaries between the various materials and thus does not suffer from domain truncation effects. However the resultant interaction matrix is dense. While the matrix produced in FEM is sparse, MOM produces a full, dense matrix and requires the implementation of fast solvers in order to accomplish the same computational efficiency.

In general, MOM is more efficient for open-boundary problems as it satisfies the radiation

condition through Green's function. In contrast, FEM requires the application of an absorbing boundary condition to simulate an unbounded environment as is better suited to impenetrable domains. However, the full matrix calculation time is the limiting factor for MOM.

Ideally, both FEM and MOM would be investigated with parallel identical simulations. However, the nature of the scholarship scheme which supported this work did not make this possible. This is because high-end computer resources with FEM solver software were only available while under placement at Cypress Semiconductor, CA. Upon return to DCU, MOM software using personal computing was available. Therefore, over the course of planning and revising plans with limited access to either solver at a given time and limited computing resources means that this work cannot answer the question of which solution method may be more or less efficient. As a direct result of the availability of high-end computing resources with FEM, the majority of simulation carried out in this work are done so using FEM. However, for contrast and demonstrative purposes some MOM simulations were carried out and compared to FEM results.

1.5 LITERATURE REVIEW

CAPACITIVE TOUCH-SCREEN SENSORS

Over the past decade, the advent of personal computing devices both mobile and home has caused a huge spike in demand for touch-screen technology. With applications being so far-reaching and varying hugely in size and scope, industry has driven designers to create more and more sensitive TSPs. The first touch-screens were resistive and emerged in the early 90s. Since then, new methods of touch detection have emerged such as projected capacitance [3], infrared [4] and acoustic wave [5]. Modern TSPs are typically capacitive sensors and have become the dominant method of touch detection due to their high optical transparency, multi-touch capabilities and durability [6].

However, the signals from these TSPs can be masked heavily by the presence of thick display layers which cause a huge amount of noise. This can result in a low SNR which inhibits the the detection of small object – such as styluses [6]. There is also a limit placed on touch resolution as scan times for panels scale rapidly with sensor pitch [7].

[8 - 10] have produced enhanced noise-immunity circuits in order to improve SNR and [11-13] have demonstrated that touch sensitivity can be improved by patterning sensor electrodes. Unfortunately, most sensor patterns are proprietary and the lack extensive literature describing TSP

ITO pattern design methodology reflects this. However, [14] proposed 3 new sensing ITO patterns – 1-square, 2-square and 5-square. These were simulated in order to determine if the sensitivity of a sensor could be approved by altering the ITO pattern of the classic diamond-like design. Additionally, [15] proposed a snowflake variation on the diamond design integrated on a thin-film-encapsulated display which inspired later simulations in this thesis.

Significant progress has been made in achieving a flexible TSP design [16-18], a foldable/seamless TSP integrated display [19-20] and a robust rollable display [21].

There are multiple techniques which FPCB circuitry uses in order to detect the capacitance variation. These include successive approximation [22], a relaxation oscillator [23-24], an RC-delay technique [25] and a charge transfer approach [26].

This thesis focuses on the parametrization of panel parameters and stack-up thicknesses in electrostatic simulations in order to determine good figures of merit for the design of TSPs in combination with optimizing the methodologies required to achieve this goal.

ELECTROSTATIC SIMULATION METHODOLOGY

Since the need for simulation capabilities has ballooned in recent years there have been 2 emergent methods – The Finite Element Method (FEM) and the Method of Moments (MOM), the most well-known commercial solver counter-parts to being COMSOL multiphysics and Ansys Q3D, respectively. These methods are closely related and have been introduced already. However, there are several hybrid techniques which have been investigated as alternatives.

[27] puts forth a comparison between the competing FEM-BEM (Finite Element Method Boundary Element Method) and FEM-DBCI (Finite Element Method Dirichlet Boundary Condition Iteration) techniques. FEM-BEM is the most widely used numerical method for open boundary problems [28-33]. It divides the open boundary domain into an interior region and an external one by a fictitious truncation boundary. FEM-DCBI [34-37] instead applies two boundary surfaces. One is a fictitious truncation boundary surface while the other is called an integral surface which is surrounded by the truncation one entirely. The comparison showed that FEM-BEM is more accurate than FEM-DBCI, but requires more computing time. It was therefore concluded that FEM-DCBI is more appropriate for applications which demand a shorter computing time – such as parametric TSP studies. Conversely, FEM-BEM is more appropriate in cases in which a high level of precision is required in a single computation.

[38] put forth a new hybrid method named FEM-Actual Charge Method, in which the media in electrostatic fields were replaced by actual charge lying on their surfaces or volumes. It is claimed

that the the computer storage requirements were significantly reduced by this method. The authors also cited the workload of developing the program being an advantage as widely used simulation software such as Ansys can be used to form an iterative loop between itself and the developer program which can be used to compute the boundary-value problem in an iterative procedure.

[39] describes a method known as Infinite Elements. Instead of defining a truncation at the boundary of the domain, infinite elements attempts to surround the domain with layer of elements which scale to infinity. The benefit is increased accuracy at the cost of additional solving time.

The application of hybrid methods seems to be insignificant in the case of FEM-BEM, Infinite Elements and FEM-Actual Charge Method., where a slight increase in accuracy comes at the cost of multiple orders of magnitude in solution time. Therefore, it is unlikely that these methods will become widespread in TSP simulation methodology. FEM-DCBI seems promising but has yet to be implemented in commercial solvers such as Ansys and COMSOL.

This thesis will utilize the FEM and MOM techniques in order to compute a capacitive matrix for TSPs. Implementation of advanced hybrid techniques was not practical as access to high-end computer resources was extremely limited while on placement.

CHAPTER 2

SENSOR DESIGN

2.1 THE TOUCH-SENSOR CIRCUIT

In order to understand the operation of a TSP we need to first describe the basic components of the sensor. The TSP consists of interlocking rows and columns of electrodes. The rows are normally designated as transmission electrodes (Tx) while the columns are designated as receiving electrodes (Rx). Each column and row is connected to a chip which controls the activation of electrodes in the panel. To “scan” the panel, the chip activates a 1 volt signal (capacitance does not depend on voltage, therefore 1 volt is more than enough) on the first Tx electrode and in turn each Rx electrode draws charge from the activated Tx electrode, returning a signal for each Rx electrode back to the controller. When a Tx electrode is active, all other Tx electrodes in the panel are grounded by the chip. Once the active electrode has settled (by industry standard an electrode is considered “settled” according to a time constant of $3RC - 95\%$ settled) the chip then activates the second Tx electrode, followed by the third, and so on until the entire panel has been scanned. The result of this is that the chip can convert the voltages for each Rx electrode into capacitances which are associated with the Tx electrode that caused them. If a finger is present on some Tx/Rx intersection, charge will be drawn away from the electrode and the voltage that arrives at the chip for that activation will be less than recorded previously. Thus, the chip can recognise that a “change

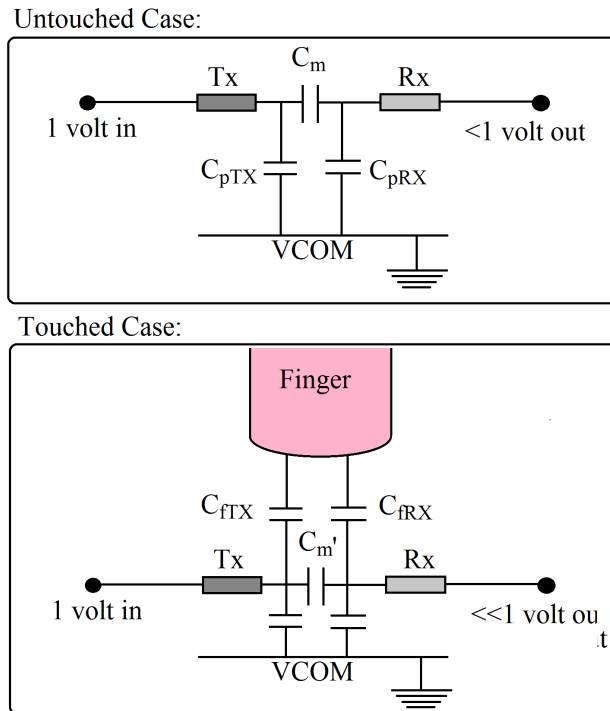


Fig. 2.1 Equivalent circuit diagram showing the various mutual, parasitic and finger capacitances of a TSP.

in mutual capacitance has taken place between these particular electrodes and deduce that there is a finger present at their location. To understand this process better, figure 2.1 has been supplied. Figure 2.1 shows the equivalent circuit diagram for the case of an Tx/Rx circuit with and without the presence of a finger. C_m is known as the mutual capacitance between Tx and Rx in display mode with no finger present while C_m' corresponds to the mutual capacitance between Tx and Rx in a touched case. C_{pTX} is known as the parasitic capacitance between Tx and common ground with no finger present while C_{pRX} corresponds to the parasitic capacitance between Rx and common ground. C_{fTX} is known as the finger capacitance between Tx and a finger present while C_{fRX} corresponds to the finger capacitance between Rx and a finger present. Together these values form the full “capacitance matrix” that the experimentalist is most concerned with for electrostatic simulations.

2.2 FEATURES OF SENSOR DESIGN

Fig. 2.1 gives an impression of the sensing mechanism in the context of a single unit-cell – the repeating ITO pattern consisting of one Tx electrode and one Rx electrode. Consider figure 4 which shows a 3x3 unit cell section of a typical diamond-like pattern.

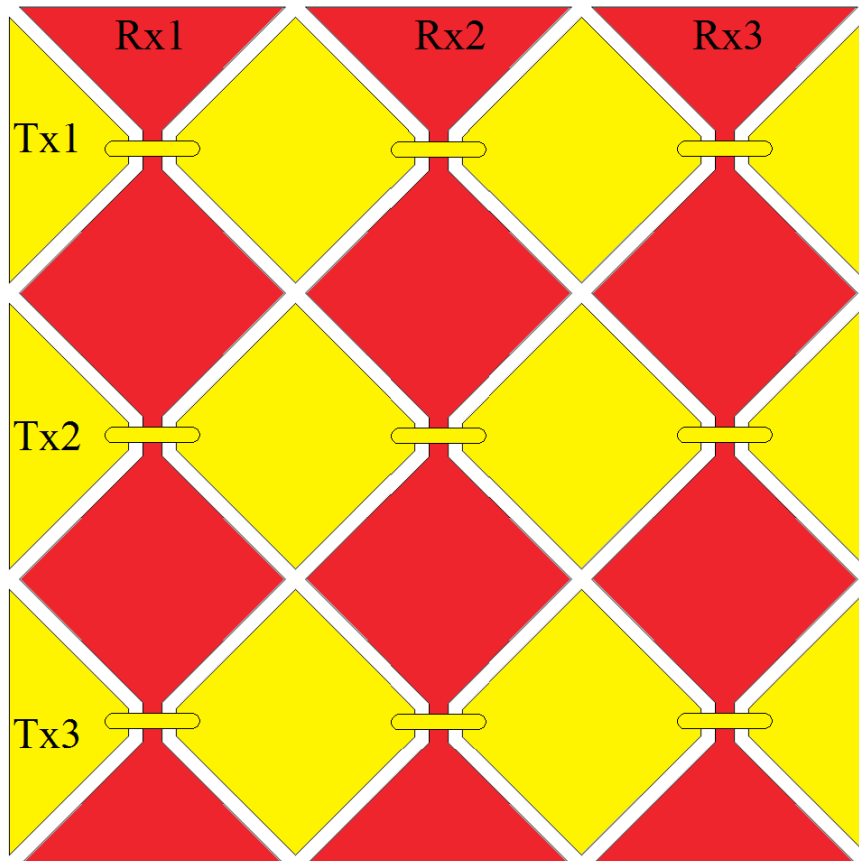


Fig. 2.2 Typical geometry of a diamond pattern ITO scheme for a 3x3 simulation.

Three distinct Tx and Rx electrodes can be seen in figure 2.2. However, an actual TSP will have many more electrodes. They are normally ordered according to a ratio of 16:9 for Tx:Rx, with the

Rx electrodes situated as columns. This is firstly due to the worldwide aesthetic whereby display ratios, among other things, tend toward the golden number. The configuration of Rx electrodes as rows is to allow the fastest routing of the Rx electrodes to the FPCB (flexible printed circuit board) housing the chip, as the routing traces are typically shortest from rows to the FPCB. This can be seen in figure 2.3.

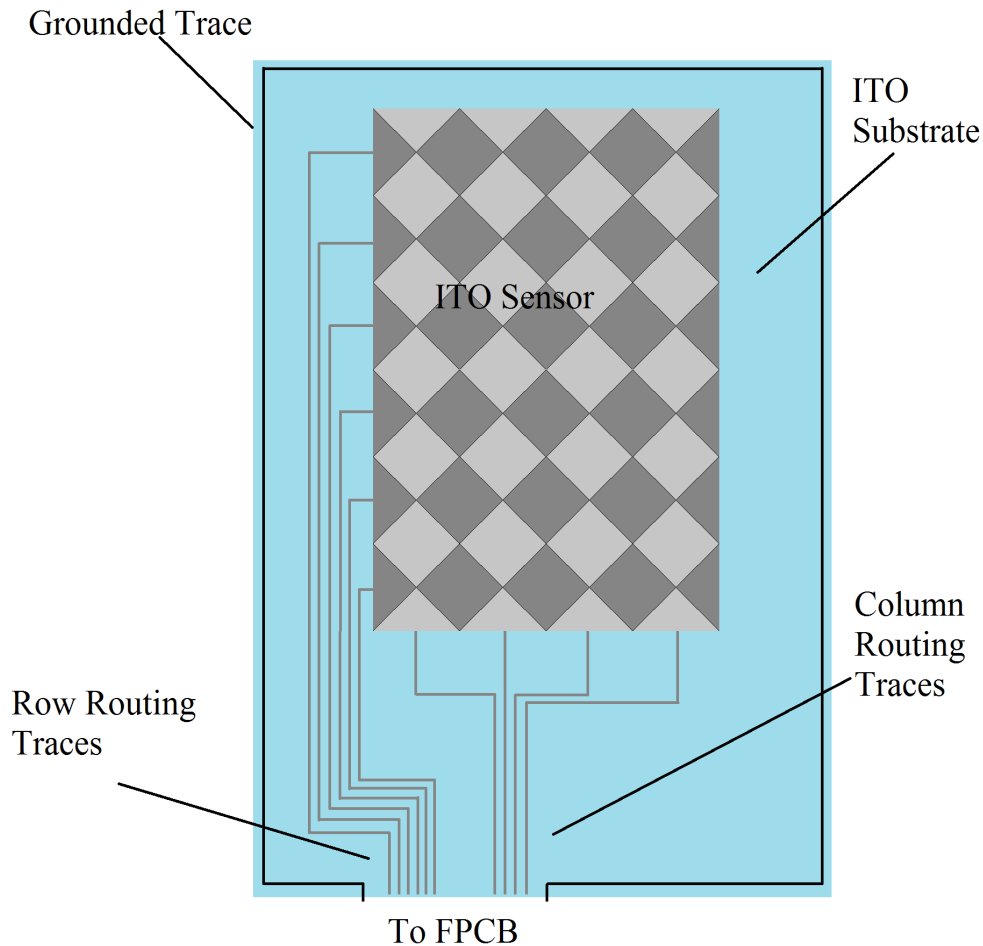


Fig. 2.3 Typical geometry of a diamond pattern ITO scheme for a full panel complete with row and column routing traces to the FPCB. ESD Protective ground trace can also be seen on the perimeter of the ITO substrate layer.

Routing traces are typically 50 microns in width and are spaced 50 microns apart. Metals such as copper and silver are used for their high conductivity to reduce the resistivity and speed up the panel as much as possible. Also noteworthy is a peripheral ground trace which protects against ESD (electrostatic discharge). These are features which are ubiquitous in TSP sensor design.

The final feature of sensor design is the “stack-up”. This refers to the collection of sensor layers that constitute the finished product. Figure 2.4 gives a typical stack-up for a diamond-like pattern.

Glass Cover Optical Clear Adhesive ITO Pattern Glass Substrate Copper Tape	Stack-Up: Glass-on-Glass	
	Thickness = 550 μm ,	Dielectric Constant = 7
	Thickness = 100 μm ,	Dielectric Constant = 3.5
	Diamond Pattern	
	Thickness = 550 μm ,	Dielectric Constant = 7
	Thickness = 508 μm ,	Dielectric Constant = 3.64

Fig. 2.4 Typical stack-up for a diamond-like design. Top later is a transparent glass cover layer which is then bound to the ITO-substrate layer with and adhesive. The sensor can then be bound to copper tape for bench-tests or to a display for use in an application.

It is paramount the relative permittivity and thickness of each layer is noted for simulation. These parameters can have a great effect on the outcome of the sensor's performance. The tape domain is not a conductor but an insulator which binds the sensor to the ground interface which in physical prototype testing would be a grounded copper domain. It is also important to note that simulations are run as time-independent (electrostatic) and are direct current (DC).

Figure 2.5 shows the 3D geometry of a 3x3 diamond panel to be simulated in Ansys Q3D. This combines all features of sensor design (with the exception of routing traces which are simulated separately if required).

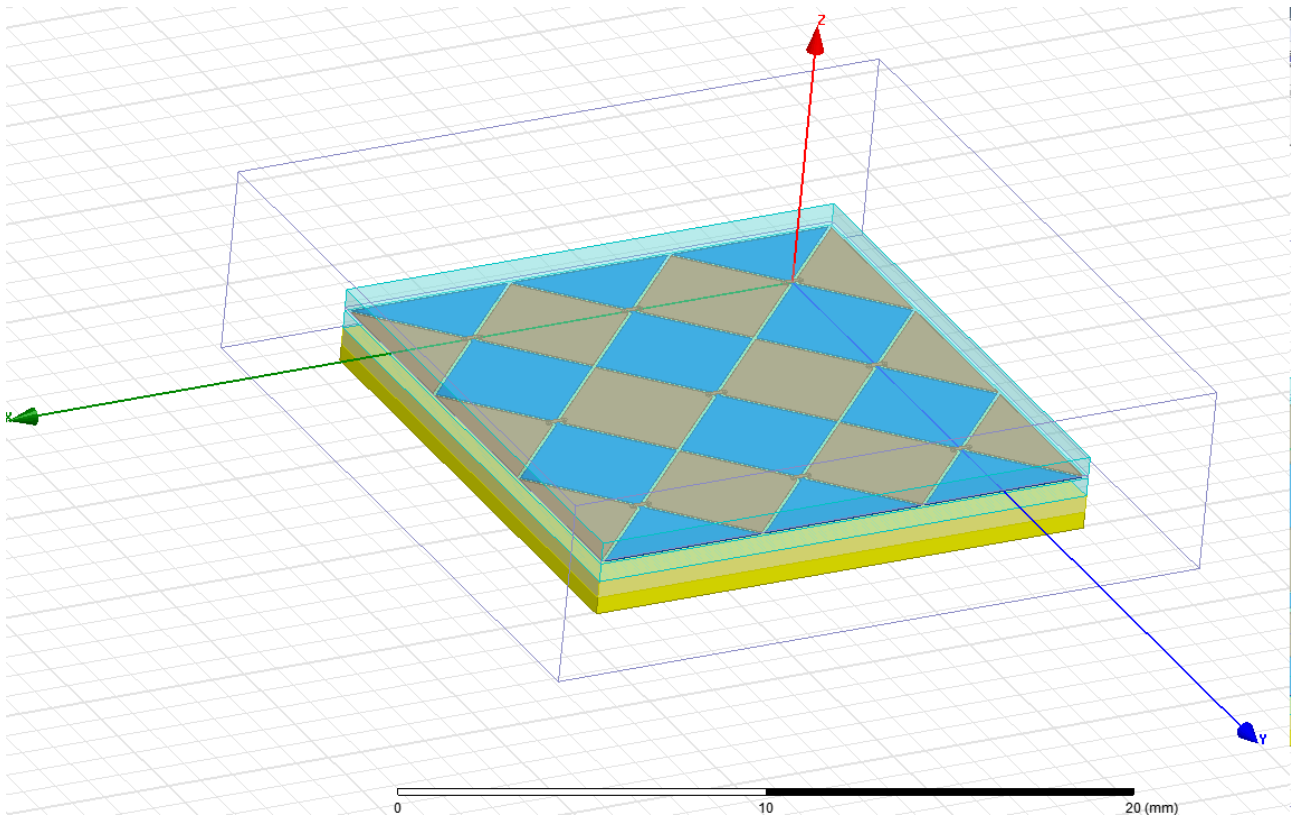


Fig. 2.5 3D geometry of a diamond TSP to be simulated using Ansys Q3D MOM solver.

2.3 CRITICAL PARAMETERS AND METRICS

Figure 2.6 illustrates the orientation of the finger, common ground and ITO pattern in the simulations. The various layers of the stack-up are also indicated in this case.

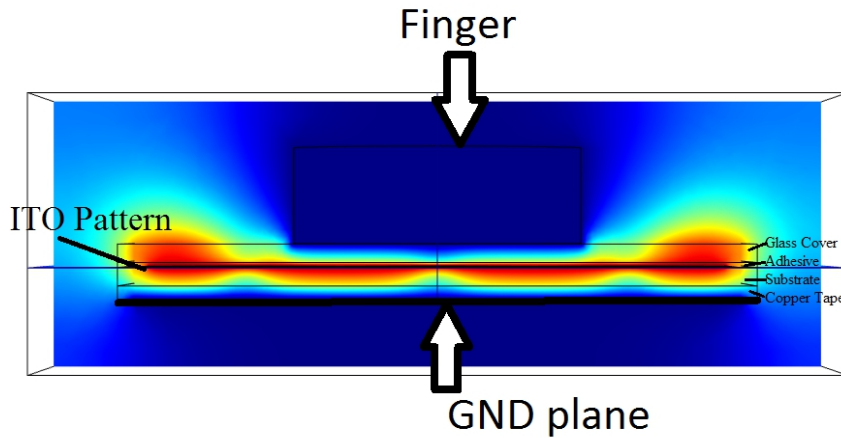


Fig. 2.6 Typical geometry of a TSP being simulated in COMSOL – a Finite Element Solver.

Part of the simulation methodology adopted in this thesis will be to attach all sensor designs to a 20 mil (508 μm) grounded copper tape domain. The reason for this is that simulation results can then be meaningfully compared to real-world test panels. While this is routine practice among designers, it is not the only method of evaluating the design. Often, a specific customer may need an evaluation of the design when attached to the application. In this case the various layers of the display can be added to the simulation. These layers can include liquid-crystal display, colour filter and adhesive layers.

The finger is modelled as a cylindrical grounded conductor. While it is known that the finger itself actually does possess a “body capacitance”, this is very small – on a scale of femto-farads, and is therefore negligible. The geometry is built and parametrised for parametric analysis. The “snowflake” shaped electrodes are set up as Rx electrodes while the larger more “diamond-like” electrodes are set up as Tx. The simulation is run in two “snapshots” - once with the central Tx electrode at 1 volt and a second time with the central Rx electrode at 1 volt. This gives a complete “before and after” view of the charge transfer process. Additionally, each set of simulations is run twice – once without a finger and once with a finger. In this way, a fully populated capacitive matrix is generated. From this matrix, key metrics are derived – such as ΔC_m , $\text{SNR}_{\text{display}}$ and $\text{SNR}_{\text{touch}}$ (defined below). It is also possible to estimate the RC time constant using additional resistance simulations if required.

The resultant datasets for each simulation can be used to evaluate the effect of different parameters on critical metrics such as ΔC_m , $SNR_{display}$ and SNR_{touch} . These metrics are defined as:

$$\Delta C_m = C_m - C_m' \quad (2.1)$$

where C_m is the mutual capacitance between Tx (transmitting electrode) and Rx (receiving electrode) when untouched and C_m' is the mutual capacitance between Tx and Rx electrodes when touched.

$$SNR_{display} = \Delta C_m / C_{pRX} \quad (2.2)$$

where C_{pRX} is the parasitic capacitance from Rx electrode to VCOM.

$$SNR_{touch} = \Delta C_m / C_{fRX} \quad (2.3)$$

where C_{fRX} is the coupled finger capacitance between a touching finger and the Rx electrode. To clarify, SNR_{touch} and $SNR_{display}$ are not related to the “*shot noise*” or “*thermal noise*” seen in electronic devices. Shot noise is due to the discrete nature of electric charge, meaning that current consists of a flow of electrons which contribute to a typically small and random fluctuation of electric current. Thermal noise is due to thermal agitation of electrons. Neither of these are considerations in the simulation of TSPs carried out in this thesis. SNR, in this work, only refers to the ratio of change in mutual capacitance to parasitic capacitance which is a product of cross-talk between the electrodes and the ground plane. These are important figures of merit to the chip algorithm and are typically small numbers <1 .

Additionally, a unit cell estimation for the RC time constant for each electrode can be evaluated using:

$$\tau_{touchedTX} = R_{TX} (C_m' + C_{fTX}) \quad (2.4)$$

$$\tau_{touchedRX} = R_{RX} (C_m' + C_{fRX}) \quad (2.5)$$

for the touched case (C_{pTX} and C_{pRX} are excluded from these formulae as they are significantly smaller than contributions from finger capacitances) or:

$$\tau_{untouchedTX} = R_{TX} (C_m + C_{pTX}) \quad (2.6)$$

$$\tau_{untouchedRX} = R_{RX} (C_m + C_{pRX}) \quad (2.7)$$

for the untouched case (C_{TX} and C_{RX} are excluded from these formulae as they are significantly smaller than contributions from parasitic capacitances),

where R_{TX} is the unit cell resistance of the Tx electrode and R_{RX} is the unit cell resistance of the Rx electrode. Notably, ITO normally has a sheet resistance which ranges between 150 – 230 Ω/\square (Ohms per square) which is used to calculate unit-cell resistances of the electrodes in resistance simulations when required, given by:

$$R_{electrode} = R_s \cdot \frac{L}{W} \quad (2.8)$$

$$R_s = \frac{\rho}{t} \quad (2.9)$$

where R_s is the sheet resistance, ρ is the bulk resistivity of the ITO, t is the thickness of the ITO, L is the length of the electrode and W is the width of the electrode.

2.4 ITO PATTERNS

This thesis will deal with the two most common types of ITO patterns – diamond-like and Manhattan-like. Diamond-like patterns consist of a single ITO layer design of interlocking diamonds separated by a deletion region. One set of electrodes is linked by a continuous ITO bridge etched into the pattern, the other electrodes are linked by bridges which rise above the main pattern layer. These bridges can be seen clearly in figure 2.2. Manhattan-like patterns consist of two separated layers of electrodes, normally fabricated onto separate substrates, separated by adhesive layers within the stack-up. The electrodes are rectangularly shaped and are orthogonal to one another. The Rx electrodes are much smaller than the Tx so as to reduce parasitic capacitance to common ground and maximize the speed of the sensor. Figure 2.7 gives the ITO layout of a typical Manhattan sensor.

The operation of the sensor is identical to that described for a typical diamond pattern in chapter 2.1. The Rx electrode layer is positioned above the Tx electrode layer. This ensures that the Tx layer forms a charge insulating grounded layer between the Rx layer and common ground, thus reducing C_{pRx} and resulting in a high SNR.

In addition to the typical diamond design, this thesis will also focus on a diamond-like design known as the snowflake pattern. This pattern is inspired by [15] and is of particular interest due to its complex geometry. Figure 2.8 gives the ITO pattern layout of the design.

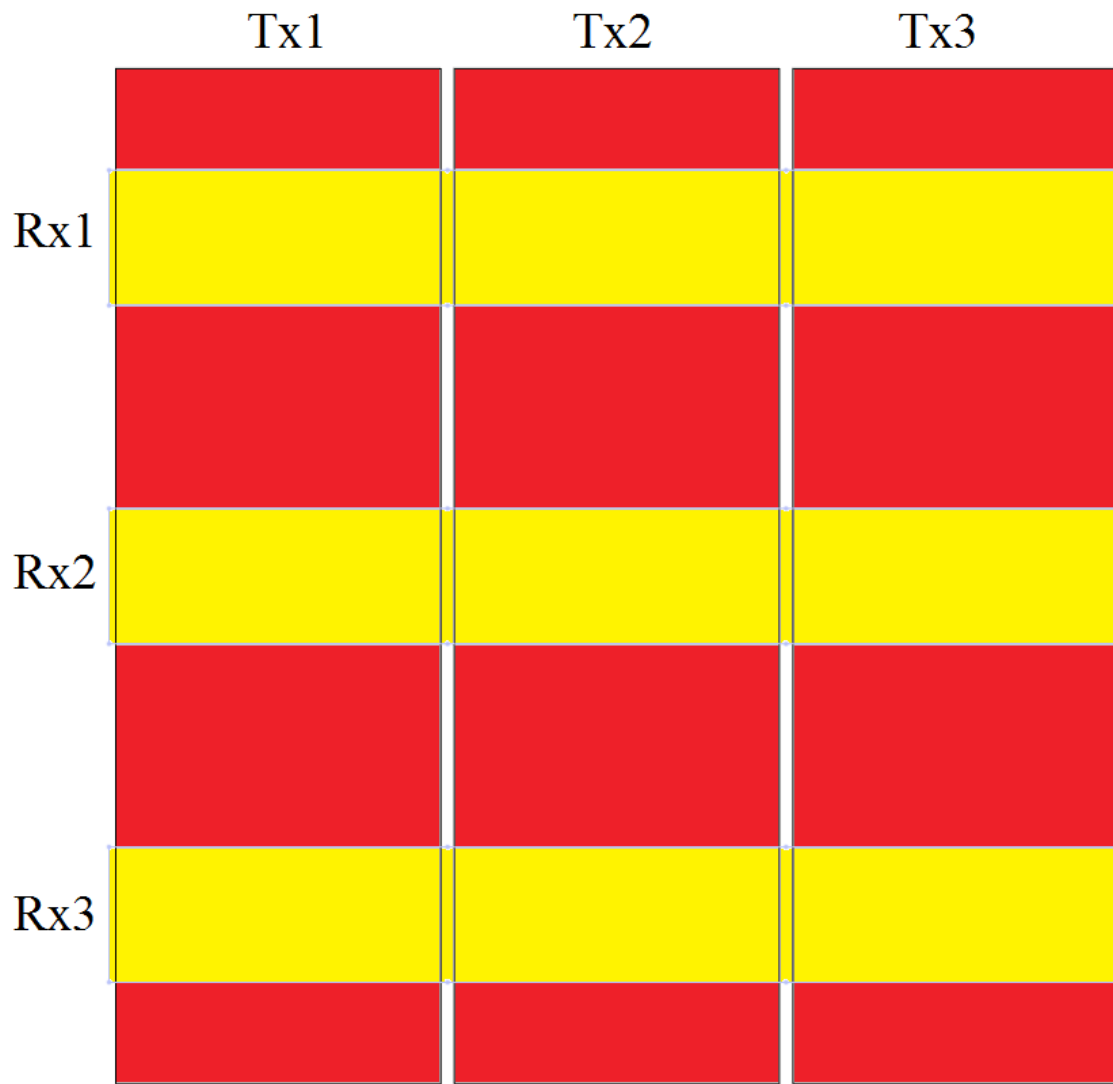


Fig. 2.7 Typical geometry of a Manhattan pattern ITO scheme for a 3x3 simulation.

This pattern has a high number of pattern parameters which could be investigated in a parametric sweep. Additionally, as mentioned previously in the case of Manhattan sensors, Rx electrodes are usually chosen to be the smaller area electrodes in order to maximise the SNR for a given panel. In a typical diamond pattern there is only a slight difference in the size of Tx and Rx electrodes. However, the diagonal bars cut into the snowflake pattern have the effect of significantly reducing the area of a single electrode. Therefore, a snowflake pattern can be considered a diamond pattern which has the Manhattan-like advantage of a high SNR due to a significantly smaller area Rx electrode. This make the snowflake pattern a good prospect for single-layer ultra-thin sensor applications which require a high SNR.

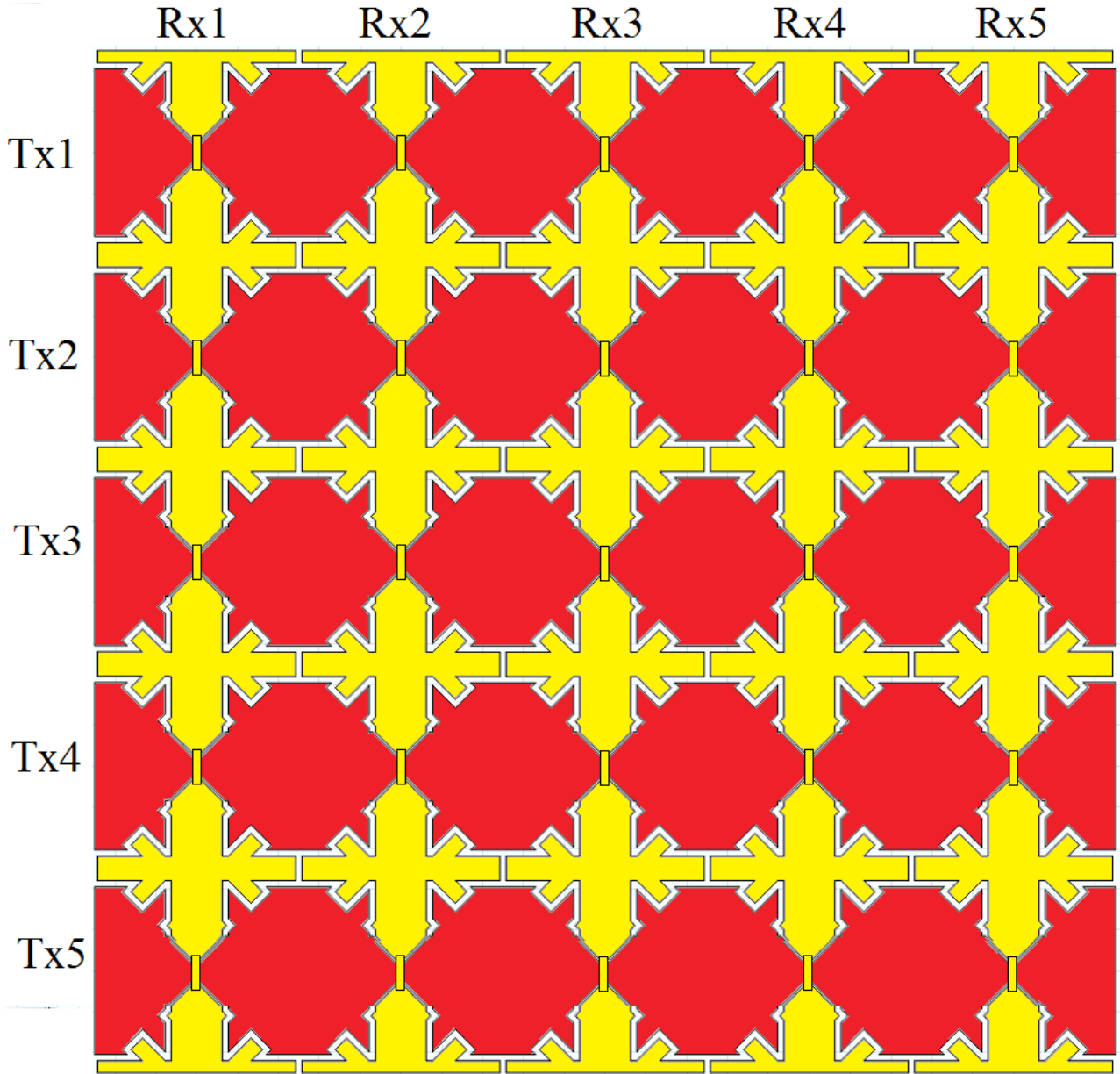


Fig. 2.8 Typical geometry of a diamond pattern ITO scheme for a 5x5 simulation.

In a diamond-like pattern, there is only a single layer of panel ITO. Therefore, one set of electrodes must be connected using raised ITO bridges which protude into and are isolated by the adhesive layer in the stack-up. In simulations, these bridges can be modelled as two cylindrical ITO pins connected by a rectangular ITO bridge. Each cylinder is joined onto the end of each required piece of the electrode. Boolean operations are then carried out so that the collection of conductors can be considered one solid object. The appropriate voltage of 0 or 1 volt is then applied as required.

2.5 STACK-UPS

There exist many different types of stack-ups, with those implemented being hugely dependent on both processing capabilities and customer needs. This thesis will focus on a selection of hand-picked stack-ups which are widely used in industry and will be used in later experimental studies. They will be divided into single-layer ITO and double-layer ITO patterns. The single-layer stack-ups will consist of GG (glass-on-glass) and SOL (sensor-on-lens). The double-layer stack-ups will consist of GFF (glass-film-film) and GF (glass-film). These stack-ups will compete against one another in later experimental studies. Figures 2.9, 2.10, 2.11 and 2.12 show each stack-up, respectively.

Stack-Up: Glass-on-Glass	
Glass Cover	Thickness = 550 μm , Dielectric Constant = 7
Optical Clear Adhesive	Thickness = 100 μm , Dielectric Constant = 3.5
ITO Pattern	Diamond Pattern
Glass Substrate	Thickness = 550 μm , Dielectric Constant = 7
Copper Tape	Thickness = 508 μm , Dielectric Constant = 3.64

Fig 2.9 GG stack-up.

Stack-Up: Sensor-on-Lens	
Glass Cover	Thickness = 550 μm , Dielectric Constant = 7
Optical Clear Adhesive	Thickness = 100 μm , Dielectric Constant = 3.5
ITO Pattern	Diamond Pattern
Copper Tape	Thickness = 508 μm , Dielectric Constant = 3.64

Fig 2.10 SOL stack-up.

Stack-Up: Glass-Film-Film	
Glass Cover	Thickness = 550 μm , Dielectric Constant = 7
OCA1	Thickness = 100 μm , Dielectric Constant = 3.5
Rx ITO	Rx Manhattan Pattern
FILM1	Thickness = 100 μm , Dielectric Constant = 3.5
OCA2	Thickness = 100 μm , Dielectric Constant = 3.5
Tx ITO	Tx Manhattan Pattern
FILM2	Thickness = 100 μm , Dielectric Constant = 3.5
OCA3	Thickness = 100 μm , Dielectric Constant = 3.5
Copper Tape	Thickness = 508 μm , Dielectric Constant = 3.64

Figure 2.11 GFF stack-up.

Stack-Up: Glass-Film	
Glass Cover	Thickness = 550 μm , Dielectric Constant = 7
OCA1	Thickness = 100 μm , Dielectric Constant = 3.5
Rx ITO	Rx Manhattan Pattern
FILM1	Thickness = 100 μm , Dielectric Constant = 3.5
Tx ITO	Tx Manhattan Pattern
OCA2	Thickness = 100 μm , Dielectric Constant = 3.5
Copper Tape	Thickness = 508 μm , Dielectric Constant = 3.64

Figure 2.12 GF stack-up.

Note that in figure 2.10, the ITO pattern is not shorted to the “Copper tape” domain. This tape domain is merely an typical domain used in experimentation which serves as a useful means by which to standardize experiments for the purposes of comparison. A 512 μm “tape” domain is chosen as it allows for a meaningful comparrison to bench testing of physical prototype panels which utilize an adhesive-tape-to-copper-block setup. In reality, there is always an insulating material between the sensor and ground plane. These insulating layers can include an air-gap layer or various display layers – LED, LCD, Colour Filter.

CHAPTER 3

EXPERIMENTS

3.1 PARALLEL PLATE CAPACITOR VERIFICATION

This section summarizes the use of COMSOL Electrostatics to perform the calculation of capacitance between a parallel plate capacitor of varying dimensionality. The simulation results are then compared to data calculated from the empirical equation given by:

$$C = \epsilon_0 \epsilon_r \frac{A}{d} \quad (3.1)$$

where ϵ_0 is the permittivity of free space, ϵ_r is the relative permittivity, A is the area of each plate and d is the separation between the plates. The discrepancy between these calculations is used to illustrate the limitations of such an empirical equation.

Equation (3.1) represents an ideal case for a parallel plate capacitor such that the ratio of area to separation (A/d) is sufficiently large enough such that at the surface of either of the plates the approximation to an infinite 2-dimensional plane is appropriate. In this case, all of the field lines are contained within the cavity between the plates. This formula is a good approximation so long as the area A is much greater than the distance d. To be precise, if $A = w \cdot l$ where w = width and l = length then both $w \gg d$ and $l \gg d$. This is because a very large area capacitor can still be very thin in one dimension, resulting in fringing fields. In this way, the capacitor can be viewed as two infinite conducting planes.

However, all capacitors are made of finite conducting plates, so there is a optimal dimension range corresponding to w, l and d for which (3.1) is valid. The larger the discrepancy between capacitances calculated by COMSOL and those calculated from (3.1), the more fringing there is between plates. This experiment shows the agreement of the FEM solver with the empirical equation in such an ideal case and also highlights the disagreement between the two calculations as capacitive fields between more complex geometries are formed.

As a shorthand, it was determined that for the purposes of this experiment the “dimensional factor” would be expressed as:

$$D_f = A/d = wl/d \quad (3.2)$$

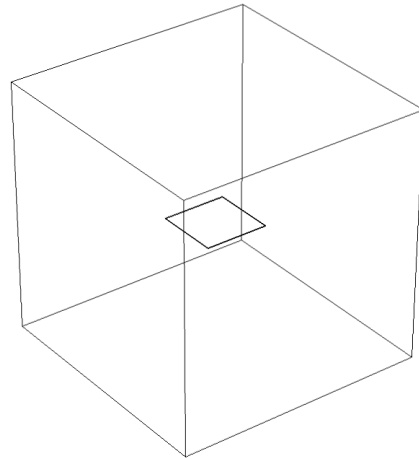
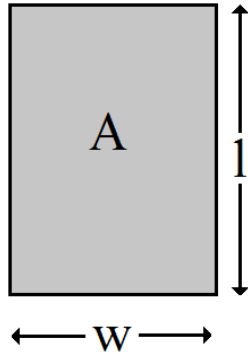
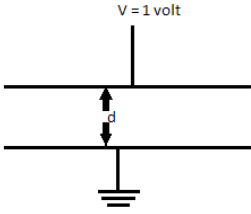


Fig. 3.1 Plate capacitor features and setup

Fig. 3.2 Plate capacitors 3D geometry.

Figures 3.1 and 3.2 shows boundary mesh “element quality” obtained from the solution of the FEM model. Element quality refers to the ratio of edges in a triangular or triangular-face mesh (such tetrahedral in 3D). At a value of 1 the element face is described as being a perfect equilateral triangle while this number decreases towards 0 as the face becomes deformed. This is a feature included by COMSOL which allows the designer to get a quick glance at the “quality” of the mesh. How exactly element faces are valued between 1 and 0 is not specified within the software. However, it is likely a ratio of angle or sides within each element face.

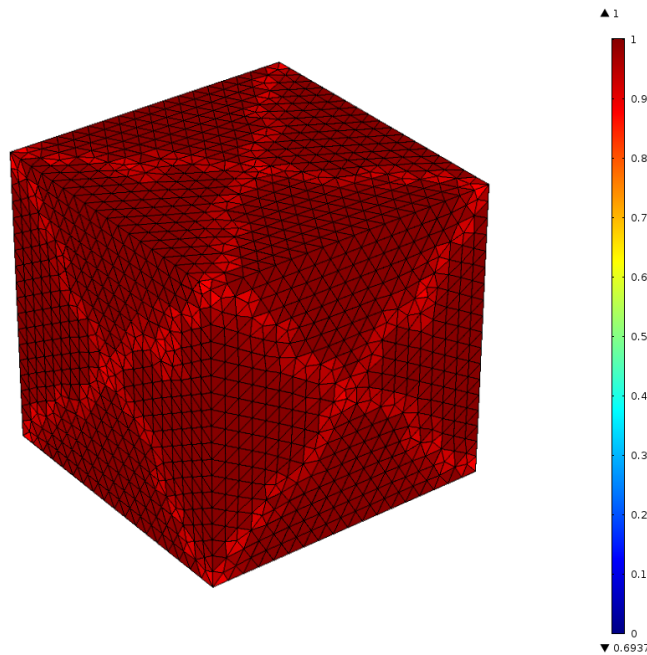


Fig. 3.3 Exterior domain boundary mesh element quality. 1 = equilateral triangular face 0 = worst case scalene triangular face.

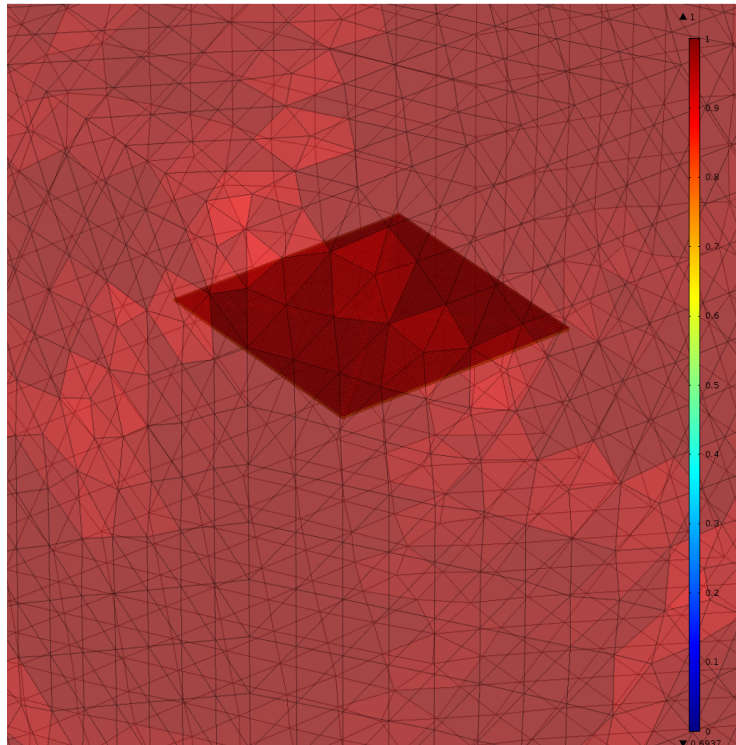


Fig. 3.4 Interior plates mesh element quality. 1 = equilateral triangular face 0 = worst case scalene triangular face.

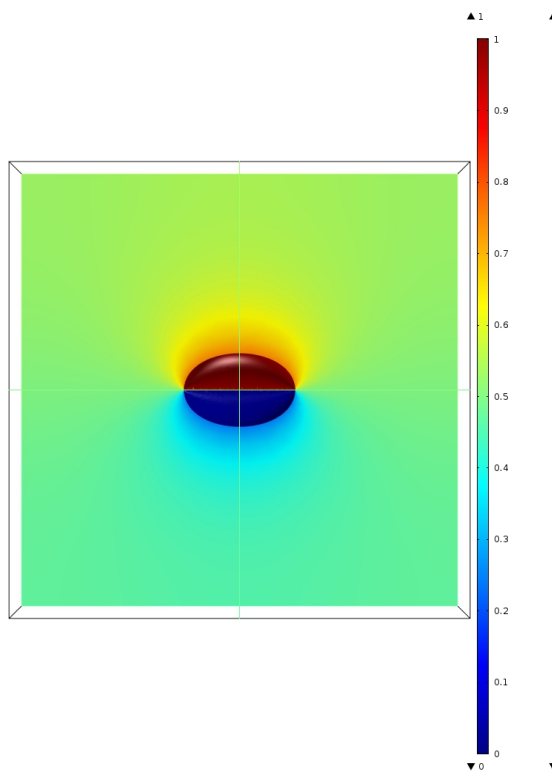


Fig. 3.5 Equipotential surfaces within the simulation domain. Scale in volts.

Figure 3.5 shows equipotential surfaces surrounding the parallel-plate capacitor calculated using FEM. The x-y plane is orientated into the page. The viewer is looking through the separation between the plates. This view was chosen because it allows the viewer to observe the difference in potential between the fields above and below the capacitor, which is not the ideal case consistent with equation (3.1) and exhibits fringe fields which can clearly be seen in fading yellow and blue. A view of the capacitor from above or below it would only show 1 extreme of the potential distribution in the problem domain.

Figure 3.6 shows the discrepancy between simulation and analytical data obtained from equation

(3.1) as a function of the dimensional factor.

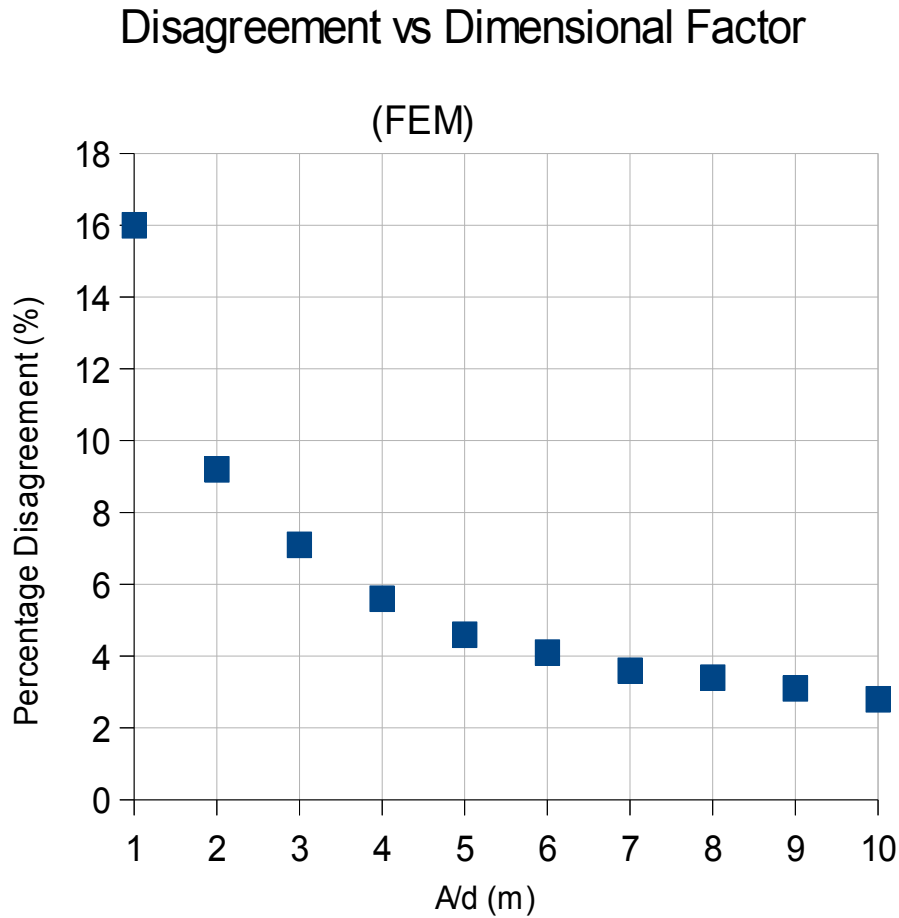


Fig. 3.6 Capacitance discrepancy between empirical equation and simulation results vs dimensional factor A/d .

Figure 3.6 shows that as the dimensional factor increases, the agreement between simulation and theory increases. This validates the FEM methodology as a means for calculating capacitance. The discrepancy is not a concern, rather it validates our view of capacitance as it is expected that fringe fields appear as the geometry and separation of the plate capacitor changes. Indeed, when it comes to TSP there are no empirical equations which can predict the mutual capacitance with any accuracy. That is what makes simulations necessary. Walker et al [40] created empirical expressions for capacitances of common microelectronic components using numerical methods. It will be shown in section 3.6 how the same can be accomplished for TSPs using “Design of Experiments” (DoE) methodology in conjunction with FEM simulation studies.

Figure 3.7 shows the 3D model used to verify the simulation integrity of the Ansys Q3D MOM solver. The table included in figure 3.7 shows the effect of increasing the dimensional on the agreement of simulation and theory, the data for which is included in the figure. This result echoes

the success of the COMSOL Multiphysics FEM model.

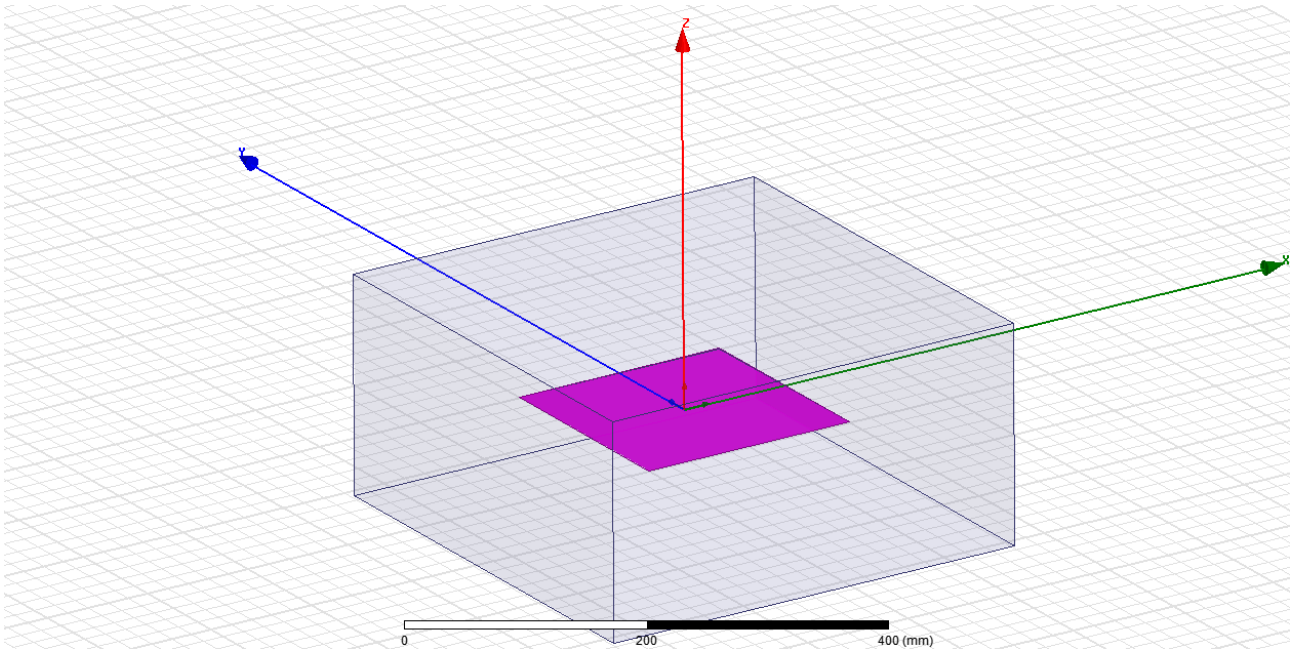


Fig. 3.7 3D view of parallel-plate capacitor model constructed using Ansys Q3D.

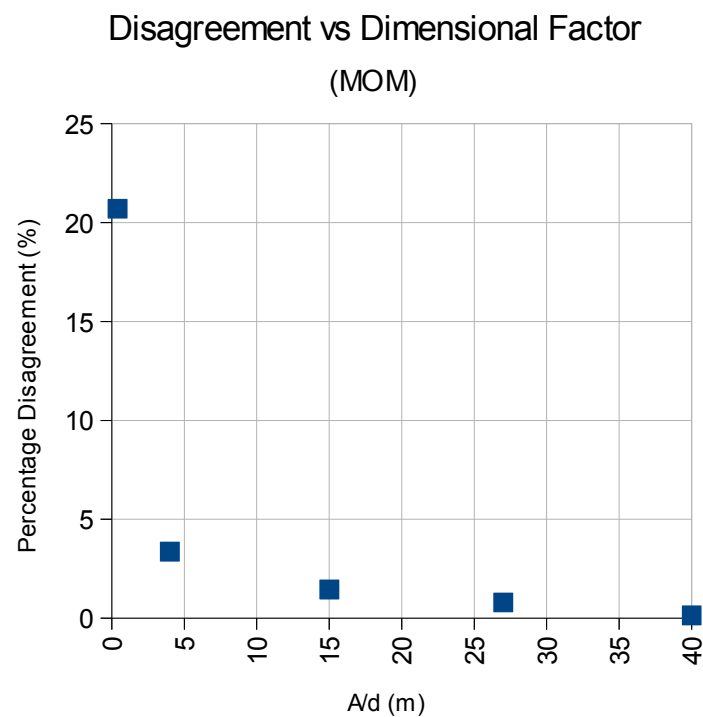


Fig. 3.8 Percentage disagreement vs dimensional factor for MOM validation study with data.

Based on the results seen in figures 3.6 and 3.8, neither simulator yields an advantage over the other when calculating the capacitance of parallel-plates as the calculation of of disagreement is almost identical.

3.2 STACK-UP SCREENING COMPARISON

It is important to investigate the effect of changing the stack-up for a fixed pattern in any TSP. Vendors often have a wide range of processing capabilities and so designers are sometimes forced to use different adhesive layer thicknesses and permittivities. Additionally, substrate materials vary in material composition and number. Double-layer ITO sensor patterns such as Manhattan designs often require two substrate layers (Glass-Film-Film) but it is also possible to process both electrode layers on a single substrate (Glass-Film). Single-layer ITO sensor patterns such as Diamond and snowflake are most commonly etched onto a substrate layer which is then covered by an adhesive and glass cover layer (Glass-Glass). However, it is possible to fabricate the ITO pattern onto the bottom interface of the glass cover itself (Sensor-On-Lens) thus eliminating the need for an extra glass substrate layer. Reducing the number of layers in the stack-up can dramatically change the behaviour of the sensor with respect to its design factor. Therefore, it is critical that we examine the effect of varying the stack-up. This chapter presents comparative studies for both Diamond and Manhattan designs. In each case, 2 distinct stack-ups are simulated and the results of identical parametric sweeps are evaluated. The first experiment compares a Diamond pattern for GG (Glass-Glass) and SOL (Sensor-On-Lens) stack-ups. The second study compares a Manhattan pattern for GFF (Glass-Film-Film) and GF (Glass-Film) stack-ups. From the resultant datasets it is shown how key metrics can be evaluated such as the change in mutual capacitance and the RC time constant.

Diamond Stack-Ups: GG vs SOL

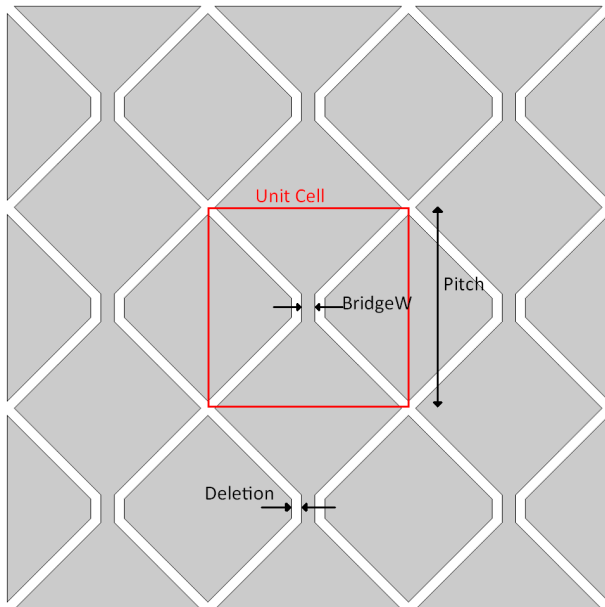


Fig. 3.9 Labeled Diamond pattern panel geometry.

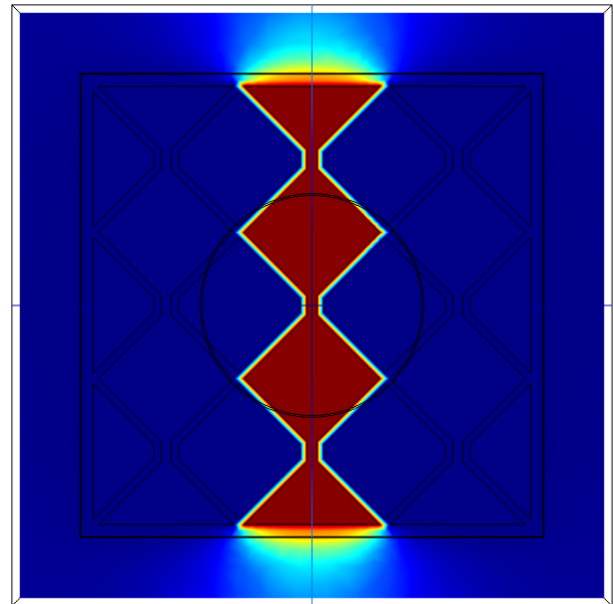


Fig. 3.11 Equipotential surfaces in diamond simulation domain.

Figure 3.9 shows the pattern layout used for the comparative Diamond study. The description of the “unit cell” marked by the red square is consistent with the Wigner-Seitz cell formation seen in the field of crystallography. The repetition of the pattern allows the designer to use a number of

locations as lattice points. However, the lattice point is chosen as the point of intersection of the central Rx and Tx electrodes. This is because these are the two electrodes which are set at 1 volt in alternating simulation while the other electrodes are held at ground. Therefore, most of the fringing in the problem domain occurs within the central unit cell. The finger is also modeled as a best case scenario – centered on the intersection of the central Rx and Tx electrodes. Moving the unit cell would therefore be equivalent to moving the finger. While investigating the effect of a moving is important (and can be seen in chapter 3.7) the rest of the the simulations in this thesis will feature a finger centered at the unit cell lattice point. Figure 3.11 shows an equipotential profile obtained from a resulting simulation. Figures 3.12 and 3.13 give the stack-ups for the GG and SOL simulations, respectively.

Parametric sweeps evaluated the following: the width of the Rx electrode ITO bridge (BridgeW), the width of the ITO deletion between the electrodes (Deletion) and the magnitude of the square unit-cell side (Pitch). The results of the sweep can be seen in tables 3.1 and 3.2.

Stack-Up: Glass-on-Glass	
Glass Cover	Thickness = 550 μm , Dielectric Constant = 7
Optical Clear Adhesive	Thickness = 100 μm , Dielectric Constant = 3.5
ITO Pattern	Diamond Pattern
Glass Substrate	Thickness = 550 μm , Dielectric Constant = 7
Copper Tape	Thickness = 508 μm , Dielectric Constant = 3.64

Fig. 3.12 GG stack-up for simulation.

Stack-Up: Sensor-on-Lens	
Glass Cover	Thickness = 550 μm , Dielectric Constant = 7
Optical Clear Adhesive	Thickness = 100 μm , Dielectric Constant = 3.5
ITO Pattern	Diamond Pattern
Copper Tape	Thickness = 508 μm , Dielectric Constant = 3.64

Fig. 3.13 SOL stack-up for simulation.

GG

BridgeW (μm)	Cm (pF)	Cm' (pF)	Cp-Tx (pF)	Cp-Rx (pF)	Cf-Tx (pF)	Cf-Rx (pF)	delCm (pF)
100	0.9145	0.6239	0.5858	0.5978	1.7340	1.7701	0.2906
150	0.9132	0.6227	0.5834	0.6004	1.7262	1.7780	0.2906
200	0.9070	0.6166	0.5808	0.6032	1.7175	1.7867	0.2905
250	0.9053	0.6152	0.5773	0.6065	1.7074	1.7971	0.2902
300	0.9035	0.6136	0.5734	0.6103	1.6957	1.8090	0.2899

Deletion (μm)	Cm (pF)	Cm' (pF)	Cp-Tx (pF)	Cp-Rx (pF)	Cf-Tx (pF)	Cf-Rx (pF)	delCm (pF)
50	1.3942	1.0950	0.5902	0.6012	1.7637	1.7973	0.2992
100	1.0828	0.7870	0.5865	0.6027	1.7455	1.7951	0.2957
150	0.9070	0.6166	0.5808	0.6032	1.7175	1.7867	0.2905
200	0.7571	0.4740	0.5730	0.6028	1.6795	1.7710	0.2832
250	0.6567	0.3825	0.5639	0.6022	1.6347	1.7508	0.2742

Pitch (μm)	Cm (pF)	Cm' (pF)	Cp-Tx (pF)	Cp-Rx (pF)	Cf-Tx (pF)	Cf-Rx (pF)	delCm (pF)
4	0.6641	0.4551	0.3748	0.3977	1.2352	1.3391	0.2089
4.5	0.7932	0.5437	0.4724	0.4950	1.4505	1.5403	0.2494
5	0.9070	0.6166	0.5808	0.6032	1.7175	1.7867	0.2905
5.5	1.0215	0.6895	0.6990	0.7216	1.9946	2.0487	0.3320
6	1.1353	0.7617	0.8282	0.8505	2.2450	2.2910	0.3736

Tab. 3.1 GG stack-up parametric simulation results.

SOL

BridgeW (μm)	Cm (pF)	Cm' (pF)	Cp-Tx (pF)	Cp-Rx (pF)	Cf-Tx (pF)	Cf-Rx (pF)	delCm (pF)
100	0.42879	0.14069	0.65272	0.68789	2.47259	2.59708	0.2881
150	0.42779	0.14019	0.6482	0.69276	2.45577	2.61605	0.2876
200	0.42665	0.13962	0.64349	0.69789	2.43762	2.63623	0.2870
250	0.42621	0.13902	0.63831	0.70369	2.41708	2.6573	0.2872
300	0.42359	0.13798	0.63214	0.70998	2.39213	2.68194	0.2856

Deletion (μm)	Cm (pF)	Cm' (pF)	Cp-Tx (pF)	Cp-Rx (pF)	Cf-Tx (pF)	Cf-Rx (pF)	delCm (pF)
50	0.87363	0.52323	0.68553	0.70453	2.76309	2.83255	0.3504
100	0.58958	0.26384	0.66886	0.70361	2.63562	2.7615	0.3257
150	0.42665	0.13962	0.64349	0.69789	2.43762	2.63623	0.2870
200	0.31523	0.07356	0.60847	0.68824	2.18555	2.47305	0.2417
250	0.23826	0.03942	0.56868	0.67455	1.92127	2.29802	0.1988

Pitch (μm)	Cm (pF)	Cm' (pF)	Cp-Tx (pF)	Cp-Rx (pF)	Cf-Tx (pF)	Cf-Rx (pF)	delCm (pF)
4	0.31002	0.10191	0.40539	0.46167	1.59167	1.91376	0.2081
4.5	0.37113	0.1227	0.51908	0.57365	1.97655	2.2435	0.2484
5	0.42665	0.13962	0.64349	0.69789	2.43762	2.63623	0.2870
5.5	0.48364	0.15748	0.78009	0.83498	2.90909	3.05745	0.3262
6	0.54128	0.17505	0.92865	0.9836	3.31173	3.44065	0.3662

Tab. 3.2 SOL stack-up parametric simulation results.

It is possible to express or graph SNR_t , SNR_d and RC time constant according the the formulas outlined in chapter 2.3 from the data is tables 1 and 2. For illustrative purposes, ΔC_m has been plotted as a function of each parametric sweep factor for both GG and SOL. These trends can be seen in figures 27, 28 and 29 below.

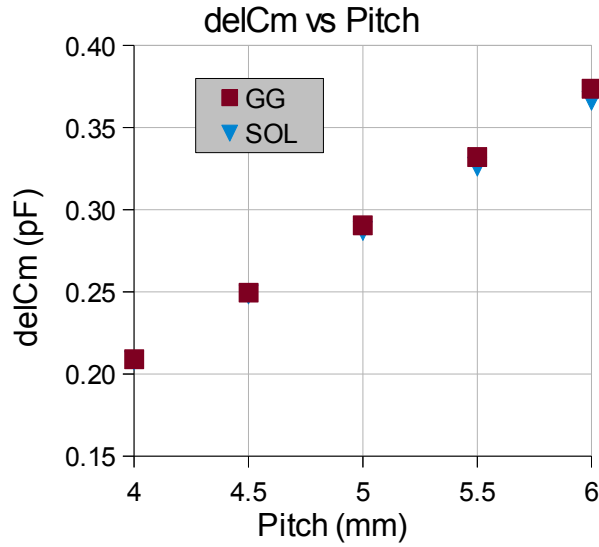


Fig. 3.14 ΔC_m vs pitch for GG vs SOL simulations.

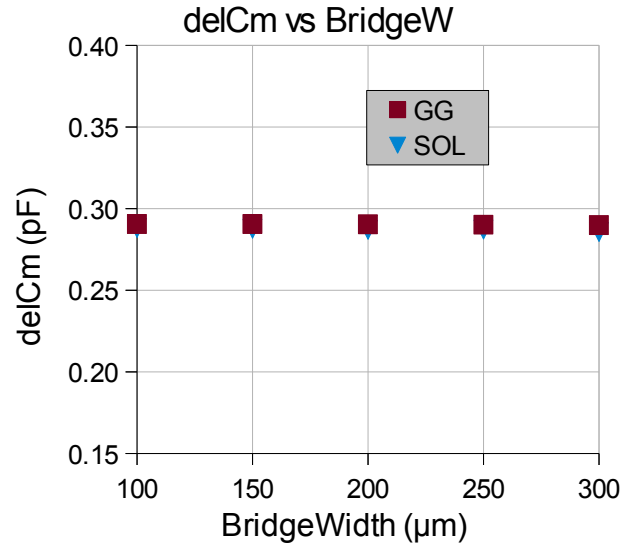


Fig. 3.15 ΔC_m vs bridge width for GG vs SOL simulations.

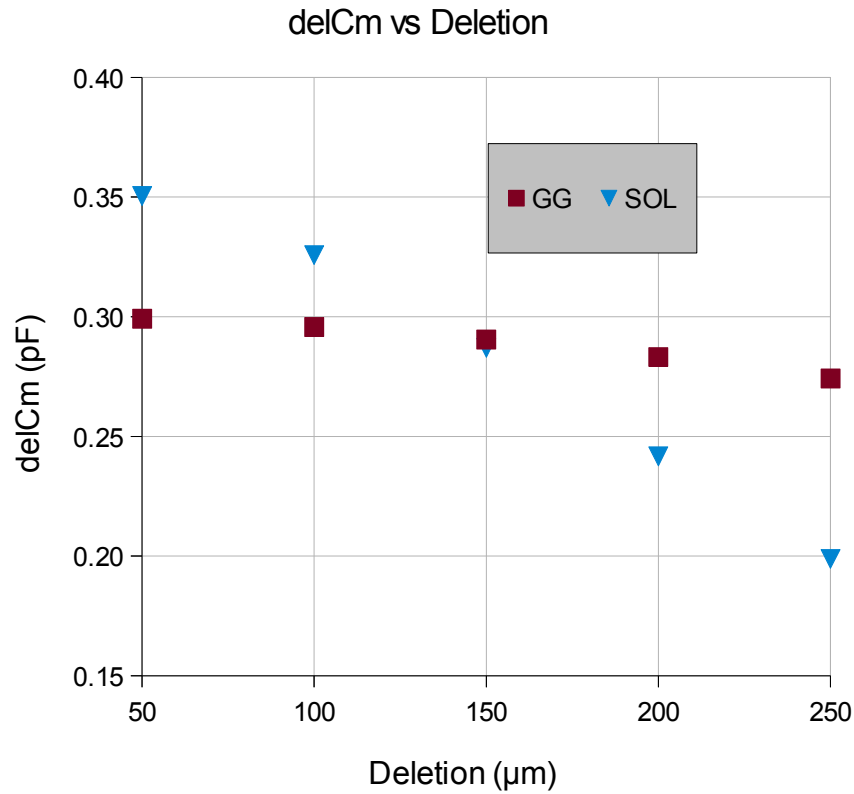


Fig. 3.16 ΔC_m vs deletion for GG vs SOL simulations.

It is clear from the above figures that changing the Rx width or bridge width causes an identical response for both GG and SOL. However, the behaviour of ΔC_m is very different between GG and SOL with respect to deletion. This is logical as the absence of a glass substrate layer pulls the sensor layer closer to the VCOM plane. This means that the effect of deletion has a greater impact on the sensor, as the deletion width is ultimately the limiting factor on how much charge is lost to the

common ground layer. This claim is confirmed by inspecting the increase in parasitic capacitances in SOL. As ΔC_m remains unchanged, SOL will yield a lower SNR for large deletions and a higher SNR for small deletions.

After reviewing these results, it is easy to make a recommendation to a potential customer or vendor. Deletion has been determined to be the highest impact factor in the when choosing between GG and SOL stack-ups for diamond. Rx Width and Bridge Width have been shown to produce the same repsonese for ΔC_m in both stack-ups. These designs are effectively interchangeable if and only if there is a low process variation in Deletion. Any design with a deletion region $<150 \mu\text{m}$ will produce an increase in ΔC_m and SNR for SOL over GG. Any design with a deletion region $>150\mu\text{m}$ will produce a decrease in ΔC_m and SNR for SOL over GG. As always, creating the best sensor will be determined by the processing limitations of the manufacturer.

Manhattan Stack-Ups: GFF vs GF

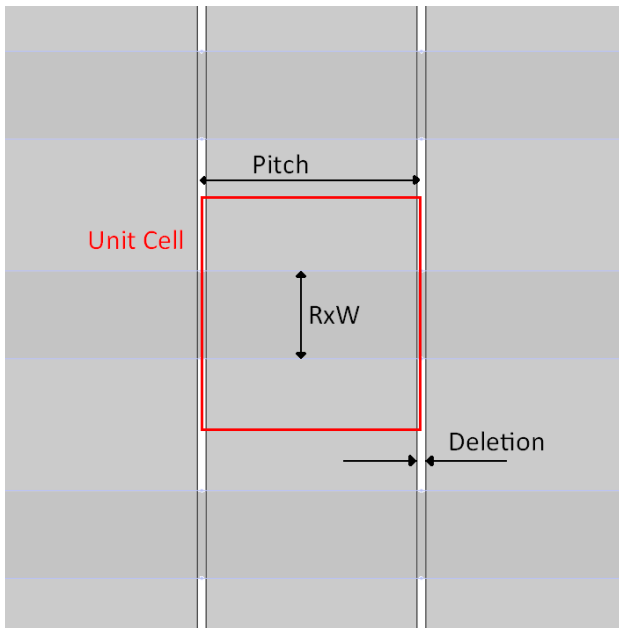


Fig. 3.17 Labelled Manhattan pattern panel geometry.

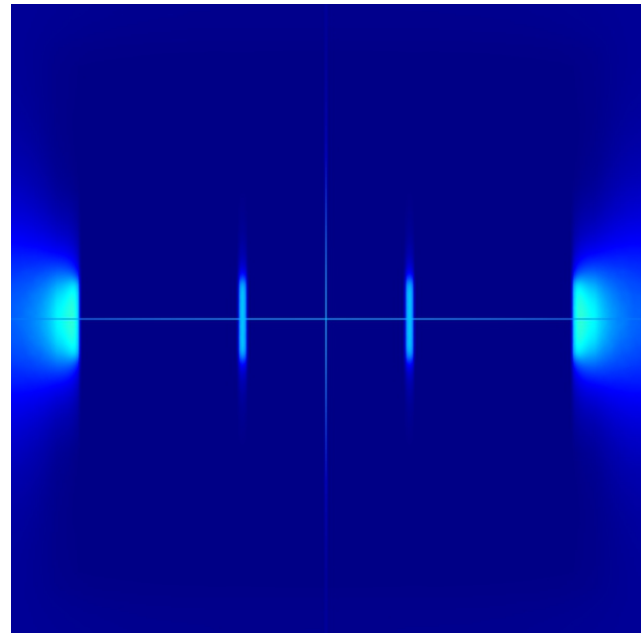


Fig. 3.18 Equipotential surfaces in Manhattan simulation domain.

Figure 3.17 shows the pattern layout used for the comparative Manhattan study. Figure 3.18 shows an equipotential profile obtained from a resulting simulation. Figures 3.19 and 3.20 give the stack-ups for the GFF and GF simulations, respectively.

Stack-Up: Glass-Film-Film

Glass Cover	Thickness = 550 μm , Dielectric Constant = 7
OCA1	Thickness = 100 μm , Dielectric Constant = 3.5
Rx ITO	Rx Manhattan Pattern
FILM1	Thickness = 100 μm , Dielectric Constant = 3.5
OCA2	Thickness = 100 μm , Dielectric Constant = 3.5
Tx ITO	Tx Manhattan Pattern
FILM2	Thickness = 100 μm , Dielectric Constant = 3.5
OCA3	Thickness = 100 μm , Dielectric Constant = 3.5
Copper Tape	Thickness = 508 μm , Dielectric Constant = 3.64

Fig. 3.19 GFF stack-up

Stack-Up: Glass-Film

Glass Cover	Thickness = 550 μm , Dielectric Constant = 7
OCA1	Thickness = 100 μm , Dielectric Constant = 3.5
Rx ITO	Rx Manhattan Pattern
FILM1	Thickness = 100 μm , Dielectric Constant = 3.5
Tx ITO	Tx Manhattan Pattern
OCA2	Thickness = 100 μm , Dielectric Constant = 3.5
Copper Tape	Thickness = 508 μm , Dielectric Constant = 3.64

Fig. 3.20 GF stack-up.

Parametric sweeps evaluated the effect of the following: the width of the Rx (RxW), the width of the ITO deletion between the Tx electrodes (Deletion) and the magnitude of the square unit-cell side (Pitch). The results of the sweep can be seen in tables 3.3 and 3.4.

GFF

RxWidth (mm)	Cm (pF)	Cm' (pF)	Cp-Tx (pF)	Cp-Rx (pF)	Cf-Tx (pF)	Cf-Rx (pF)	delCm (pF)
1.00	1.1169	0.9043	1.1277	0.0207	1.6607	1.0754	0.2126
1.50	1.4790	1.2549	1.1248	0.0275	1.3912	1.4829	0.2241
2.00	1.8277	1.6052	1.1216	0.0339	1.1285	1.8857	0.2224
2.50	2.1649	1.9552	1.1177	0.0401	0.8705	2.2831	0.2097
3.00	2.4868	2.3043	1.1132	0.0459	0.6162	2.6723	0.1825

Pitch (mm)	Cm (pF)	Cm' (pF)	Cp-Tx (pF)	Cp-Rx (pF)	Cf-Tx (pF)	Cf-Rx (pF)	delCm (pF)
4.00	1.6086	1.4247	0.8886	0.0334	0.8226	1.8750	0.1839
4.25	1.7183	1.5146	1.0015	0.0338	0.9668	1.8820	0.2037
4.50	1.8277	1.6052	1.1216	0.0339	1.1285	1.8857	0.2224
4.75	1.9349	1.6947	1.2474	0.0341	1.3044	1.8898	0.2401
5.00	2.0424	1.7853	1.3806	0.0341	1.4897	1.8914	0.2571

Deletion (μm)	Cm (pF)	Cm' (pF)	Cp-Tx (pF)	Cp-Rx (pF)	Cf-Tx (pF)	Cf-Rx (pF)	delCm (pF)
100	1.8398	1.6168	1.1274	0.0277	1.1334	1.8847	0.2230
150	1.8349	1.6121	1.1250	0.0305	1.1314	1.8852	0.2228
200	1.8277	1.6052	1.1216	0.0339	1.1285	1.8857	0.2224
250	1.8190	1.5970	1.1173	0.0376	1.1249	1.8868	0.2220
300	1.8082	1.5867	1.1122	0.0416	1.1203	1.8875	0.2215

Tab. 3.3 GFF parametric sweep simulation results.

GF

RxWidth (mm)	Cm (pF)	Cm' (pF)	Cp-Tx (pF)	Cp-Rx (pF)	Cf-Tx (pF)	Cf-Rx (pF)	delCm (pF)
1.00	1.86475	1.64922	1.13308	0.02231	2.04565	0.99518	0.2155
1.50	2.57034	2.3375	1.12971	0.03048	1.72398	1.40423	0.2328
2.00	3.2592	3.02334	1.12601	0.03845	1.40933	1.80753	0.2359
2.50	3.93918	3.71092	1.12162	0.04623	1.09936	2.20653	0.2283
3.00	4.60303	4.39596	1.11629	0.05376	0.79381	2.59826	0.2071

Pitch (mm)	Cm (pF)	Cm' (pF)	Cp-Tx (pF)	Cp-Rx (pF)	Cf-Tx (pF)	Cf-Rx (pF)	delCm (pF)
4.00	2.88328	2.68382	0.89182	0.03816	1.03496	1.79891	0.1995
4.25	3.06779	2.8496	1.00538	0.03835	1.21266	1.80273	0.2182
4.50	3.2592	3.02334	1.12601	0.03845	1.40933	1.80753	0.2359
4.75	3.44372	3.19099	1.25244	0.03863	1.625	1.80841	0.2527
5.00	3.63461	3.36559	1.38619	0.03858	1.84941	1.81345	0.2690

Deletion (μm)	Cm (pF)	Cm' (pF)	Cp-Tx (pF)	Cp-Rx (pF)	Cf-Tx (pF)	Cf-Rx (pF)	delCm (pF)
100	3.29505	3.05865	1.13392	0.02977	1.41603	1.80628	0.2364
150	3.27943	3.04325	1.13062	0.03375	1.413	1.80651	0.2362
200	3.2592	3.02334	1.12601	0.03845	1.40933	1.80753	0.2359
250	3.23763	3.00219	1.12063	0.0435	1.40363	1.80896	0.2354
300	3.21056	2.97566	1.11433	0.04884	1.398	1.80975	0.2349

Tab. 3.4 GF parametric sweep simulation results.

For illustrative purposes, ΔC_m has been plotted as a function of each parametric sweep factor for both GFF and GF. These trends can be seen in figures 34, 35 and 36 below.

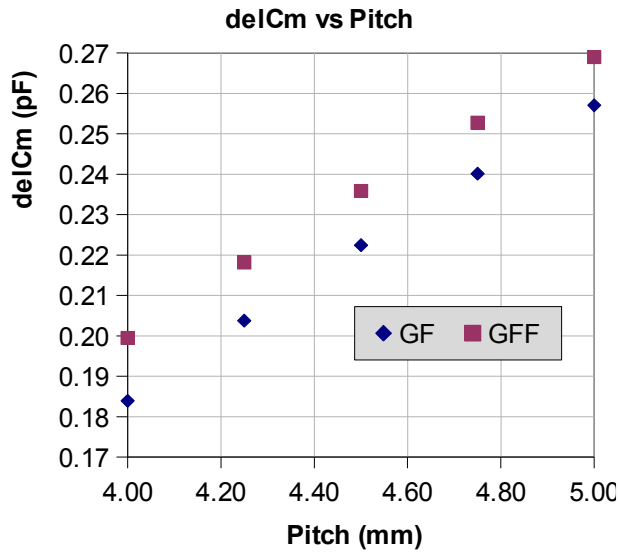


Fig. 3.21 ΔC_m vs pitch for GFF vs GF simulations.

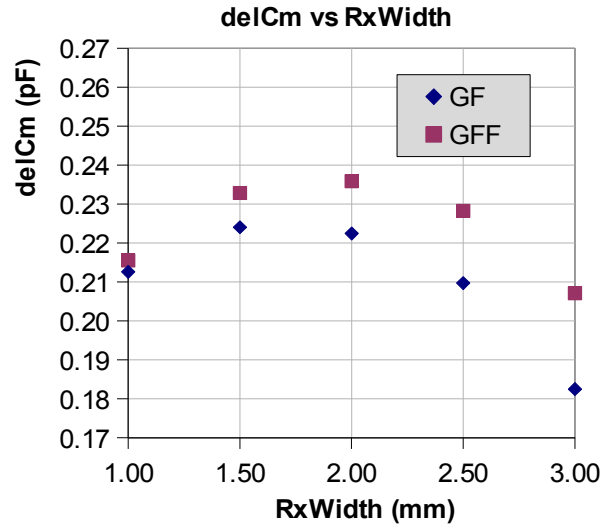


Fig. 3.22 ΔC_m vs Rx electrode width for GFF vs GF simulations.

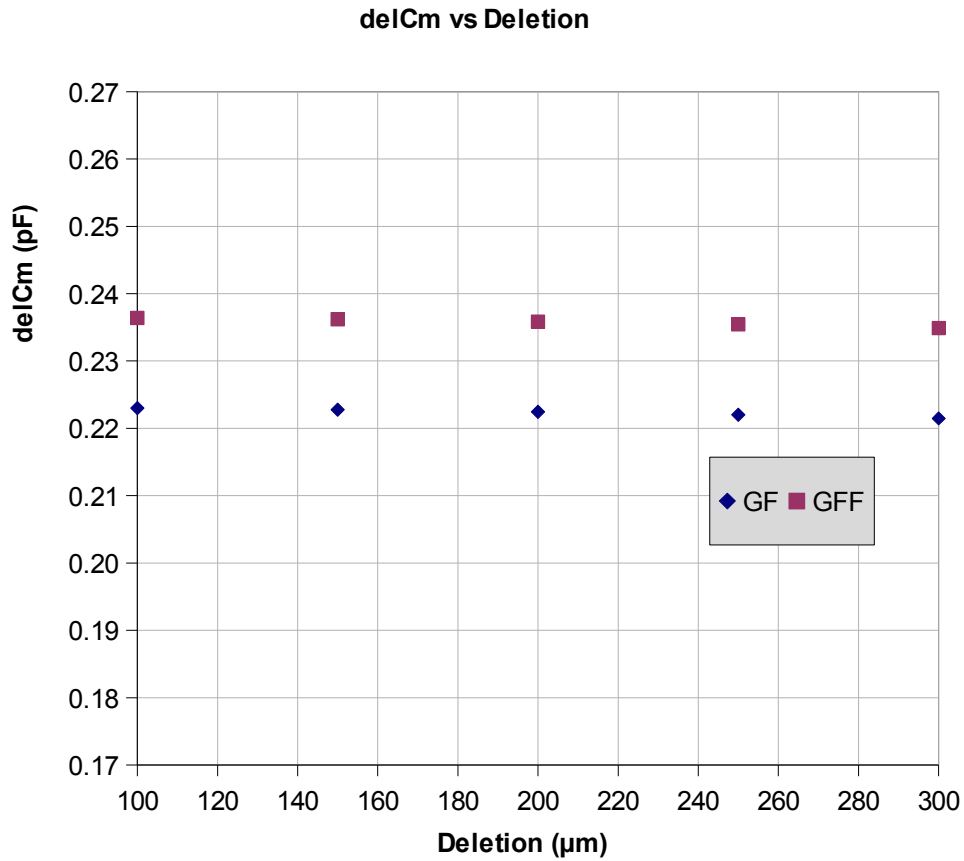


Fig. 3.23 ΔC_m vs deletion for GFF vs GF simulations.

It is clear from the above figures that changing the deletion, pitch or Rx width causes an similar response for both GFF and GF, the difference being that GFF exhibits a higher ΔC_m value in all sweeps. Pitch and deletion both exhibit linear behavior and a constant common slope in both GFF and GF. Rx width has a unique effect in that there is a maximum ΔC_m response point. The effect of

changing from GFF to GF stack-up is that it decreases the optimal Rx width value and lowers the magnitude of the maximum change in mutual capacitance. This is uncommon behaviour and close attention should be paid to Rx width in the roll-out of any Manhattan sensor.

A recommendation to a potential customer or vendor would be as follows. Upon inspection, GFF represents consistently higher values of ΔC_m and lower values of parasitic capacitance due to the extended distance from the VCOM plane. Therefore, GFF also produces a lower signal-to-noise ratio. However, GFF is thicker by at least 200 μm and would be unsuitable for ultra-thin applications. A compromise could be reached by choosing an optimal GF design of Rx Width = 1.7 mm. This would represent the smallest loss in the key sensing metric ΔC_m .

Further analysis is undertaken to evaluate an estimate for the RC time constant as a unit cell value. Tables 5 and 6 were derived from the previous results and additional resistance simulations. Resistance can be easily computed using an FEM solver by slightly modifying the conditions of the simulation, assigning sheet resistance and voltage terminals. These simulations are not required for Manhattan designs due to the simplicity of the block electrodes, allowing the user to calculate the resistances by hand. However, they are required for the more complex Diamond and Snowflake designs as there is a dynamic current spreading effect present in these panels. The RC time constant was then plotted in the untouched case for both GFF and GF. Figures 3.24, 3.25 and 3.26 show the behaviour of the RC time constant with respect to each simulation factor.

GFF								
RxWidth (mm)	SNR Display	SNR Touch	Tx-Res (Ω)	Rx-Res (Ω)	Tx-RC (pF. Ω)	Rx-RC (pF. Ω)	τ (pF. Ω)	
1.00	10.24927676	0.1976714991	156.97674419	675	175.32575581	753.90075	929.2265	
1.50	8.1621129326	0.1510931578	156.97674419	450	232.16232558	665.532	897.6943	
2.00	6.5635880791	0.1179589975	156.97674419	337.5	286.89854651	616.831875	903.7304	
2.50	5.236454432	0.0918591715	156.97674419	270	339.83895349	584.523	924.3620	
3.00	3.9795028347	0.0682945084	156.97674419	225	390.36505814	559.52325	949.8883	

Pitch (mm)	SNR Display	SNR Touch	Tx-Res (Ω)	Rx-Res (Ω)	Tx-RC (pF. Ω)	Rx-RC (pF. Ω)	τ (pF. Ω)	
4.00	5.5016452288	0.0980932825	157.89473684	300	253.98789474	482.577	736.5649	
4.25	6.0367407407	0.108256598	157.40740741	318.75	270.47314815	547.708125	818.1813	
4.50	6.5635880791	0.1179589975	156.97674419	337.5	286.89854651	616.831875	903.7304	
4.75	7.0440011734	0.1270690458	156.59340659	356.25	302.98475275	689.2903125	992.2751	
5.00	7.5323762086	0.1359176077	156.25	375	319.121875	765.8925	1085.0144	

Deletion (μm)	SNR Display	SNR Touch	Tx-Res (Ω)	Rx-Res (Ω)	Tx-RC (pF. Ω)	Rx-RC (pF. Ω)	τ (pF. Ω)	
100	8.0392934391	0.1183284076	153.40909091	337.5	282.23590909	620.919	903.1549	
150	7.2994757536	0.118173765	155.17241379	337.5	284.7212069	619.268625	903.9898	
200	6.5635880791	0.1179589975	156.97674419	337.5	286.89854651	616.831875	903.7304	
250	5.9060920458	0.1176679475	158.82352941	337.5	288.89364706	613.899	902.7926	
300	5.3214800577	0.1173397757	160.71428571	337.5	290.60517857	610.270875	900.8761	

Tab. 3.5 GFF parametric sweep resistance simulation results with calculated key metrics.

GF

RxWidth (mm)	SNR Display	SNR Touch	Tx-Res (Ω)	Rx-Res (Ω)	Tx-RC (pF. Ω)	Rx-RC (pF. Ω)	τ (pF. Ω)
1.00	9.6606902734	0.2165738861	156.97674419	675	292.72238372	1258.70625	1551.4286
1.50	7.6391076115	0.1658132927	156.97674419	450	403.48360465	1156.653	1560.1366
2.00	6.1342002601	0.1304874608	156.97674419	337.5	511.61860465	1099.98	1611.5986
2.50	4.9374864806	0.1034474945	156.97674419	270	618.35965116	1063.5786	1681.9383
3.00	3.8517485119	0.0796956425	156.97674419	225	722.56866279	1035.68175	1758.2504

Pitch (mm)	SNR Display	SNR Touch	Tx-Res (Ω)	Rx-Res (Ω)	Tx-RC (pF. Ω)	Rx-RC (pF. Ω)	τ (pF. Ω)
4.00	5.2269392034	0.1108782541	157.89473684	300	455.25473684	864.984	1320.2387
4.25	5.6894393742	0.1210330998	157.40740741	318.75	482.89287037	977.8580625	1460.7509
4.50	6.1342002601	0.1304874608	156.97674419	337.5	511.61860465	1099.98	1611.5986
4.75	6.5423246182	0.1397526004	156.59340659	356.25	539.26384615	1226.82525	1766.0891
5.00	6.9730430275	0.1483470733	156.25	375	567.9078125	1362.97875	1930.8866

Deletion (μ m)	SNR Display	SNR Touch	Tx-Res (Ω)	Rx-Res (Ω)	Tx-RC (pF. Ω)	Rx-RC (pF. Ω)	τ (pF. Ω)
100	7.9408800806	0.130876719	153.40909091	337.5	505.490625	1112.079375	1617.5700
150	6.9979259259	0.1307382744	155.17241379	337.5	508.87706897	1106.807625	1615.6847
200	6.1342002601	0.1304874608	156.97674419	337.5	511.61860465	1099.98	1611.5986
250	5.4124137931	0.1301521316	158.82352941	337.5	514.21182353	1092.700125	1606.9119
300	4.8095823096	0.1297969333	160.71428571	337.5	515.98285714	1083.564	1599.5469

Tab. 3.6 GF parametric sweep resistance simulation results with calculated key metrics.

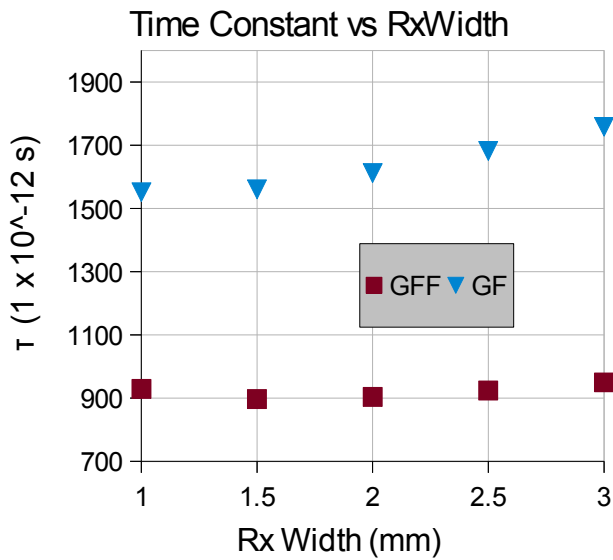


Fig. 3.24 RC time constant vs Rx electrode width for GFF vs GF simulations.

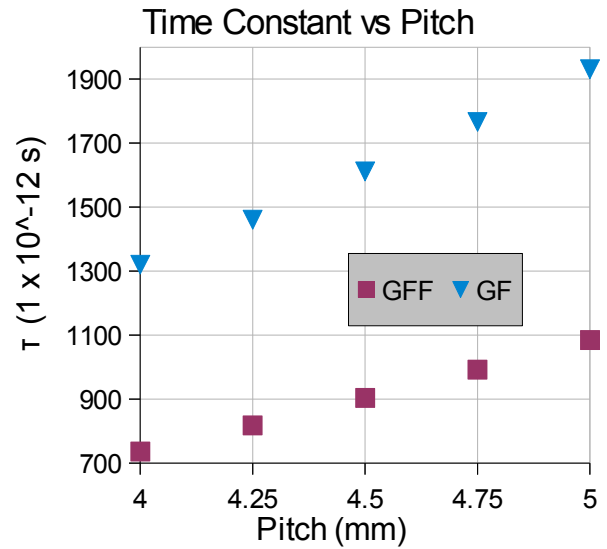


Fig. 3.25 RC time constant vs pitch for GFF vs GF simulations.

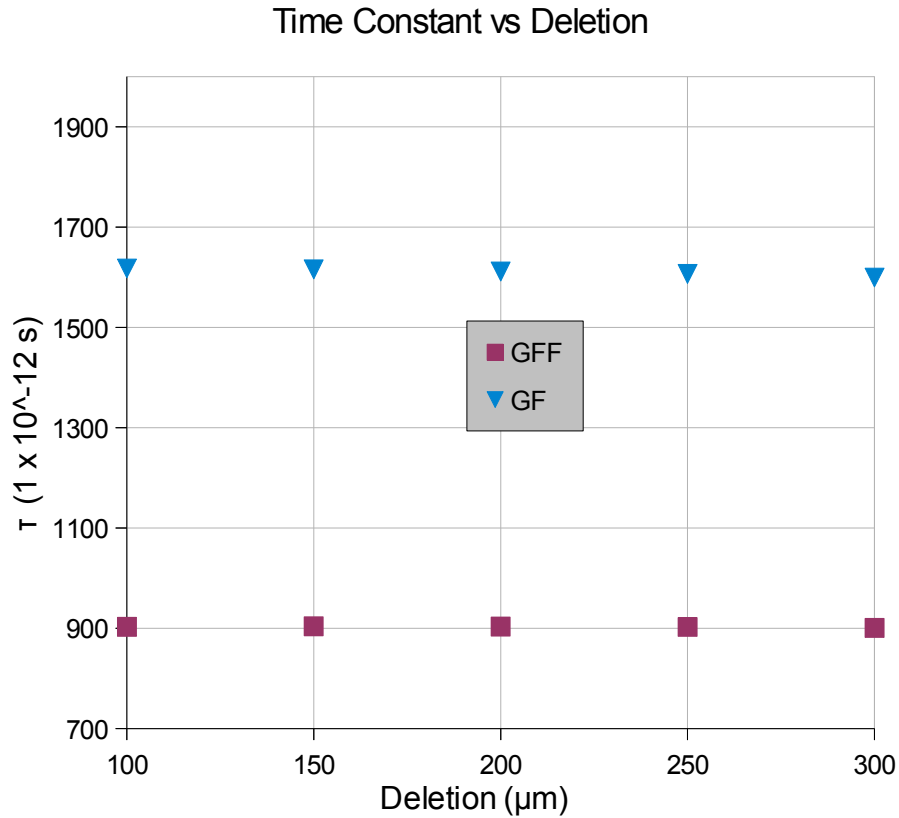


Fig. 3.26 RC time constant vs deletion for GFF vs GF simulations.

Upon inspection of the above figures it is clear that GFF produces the lowest RC time constant and therefore will yield the fastest settling panels. Any recommendation to a vendor or customer will include this information to enable them to make an informed choice. This choice is dependant on their requirements with regard to refresh rate for the specific application.

3.3 PATTERN SCREENING COMPARISON

The following experiments show the effect of using different ITO panel geometry on a fixed stack-up. In this way, it is possible to compare the merit of the sensor panel designs and determine the pros and cons of each. As engineers, we are always looking to improve existing designs. The snowflake design is in truth a special case of the Diamond design and operates under the exact same principles. They are both single-layer sensors and the only differences between them are slight differences in geometry. Screening Analysis was performed on identical GG stack-ups for diamond and snowflake patterns. ΔC_m was compared as a function of several pattern parameters of interest.

Glass-on-Glass Stack-Up: Diamond vs Snowflake

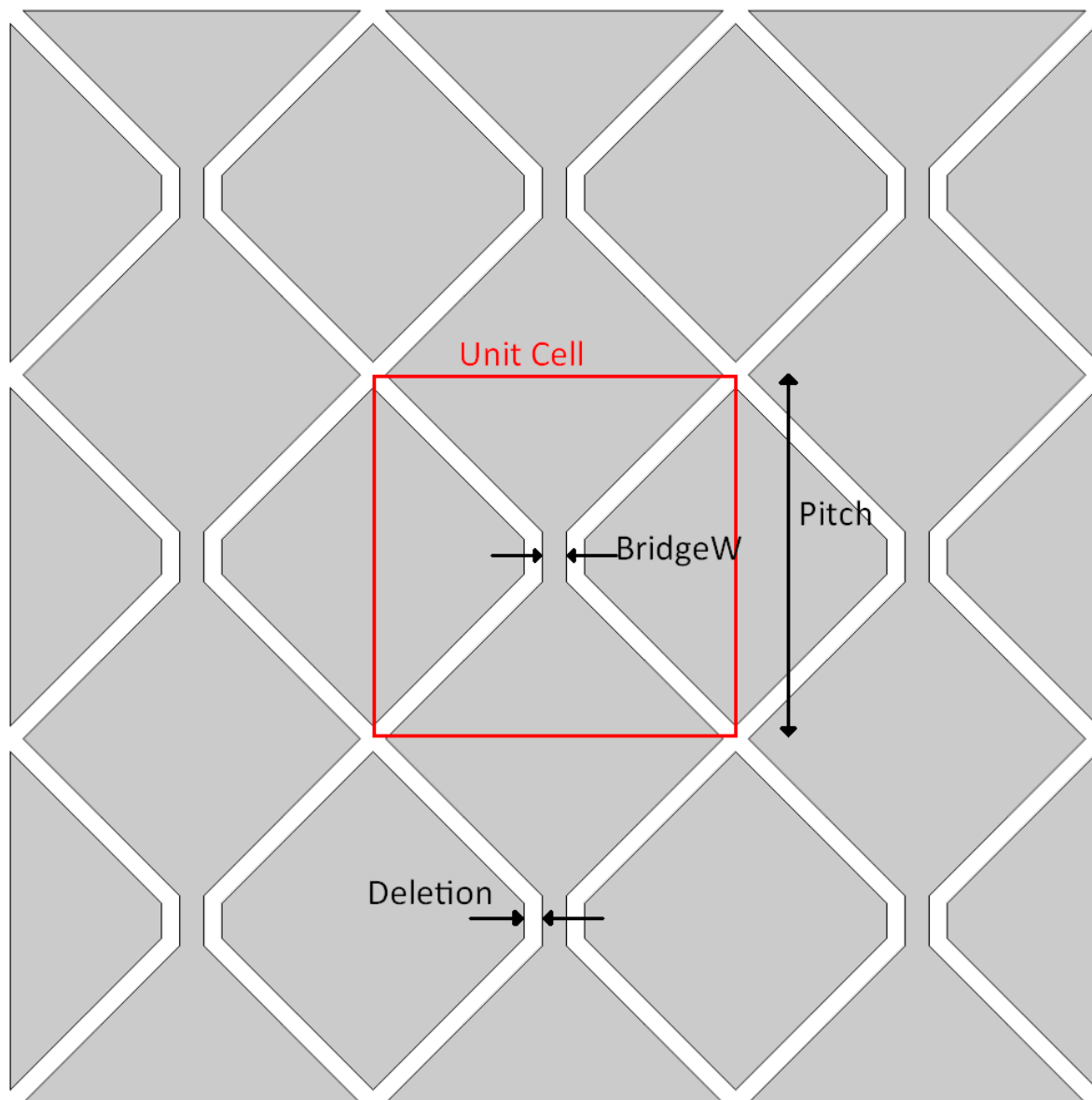


Fig. 3.27 Labelled diamond pattern layout.

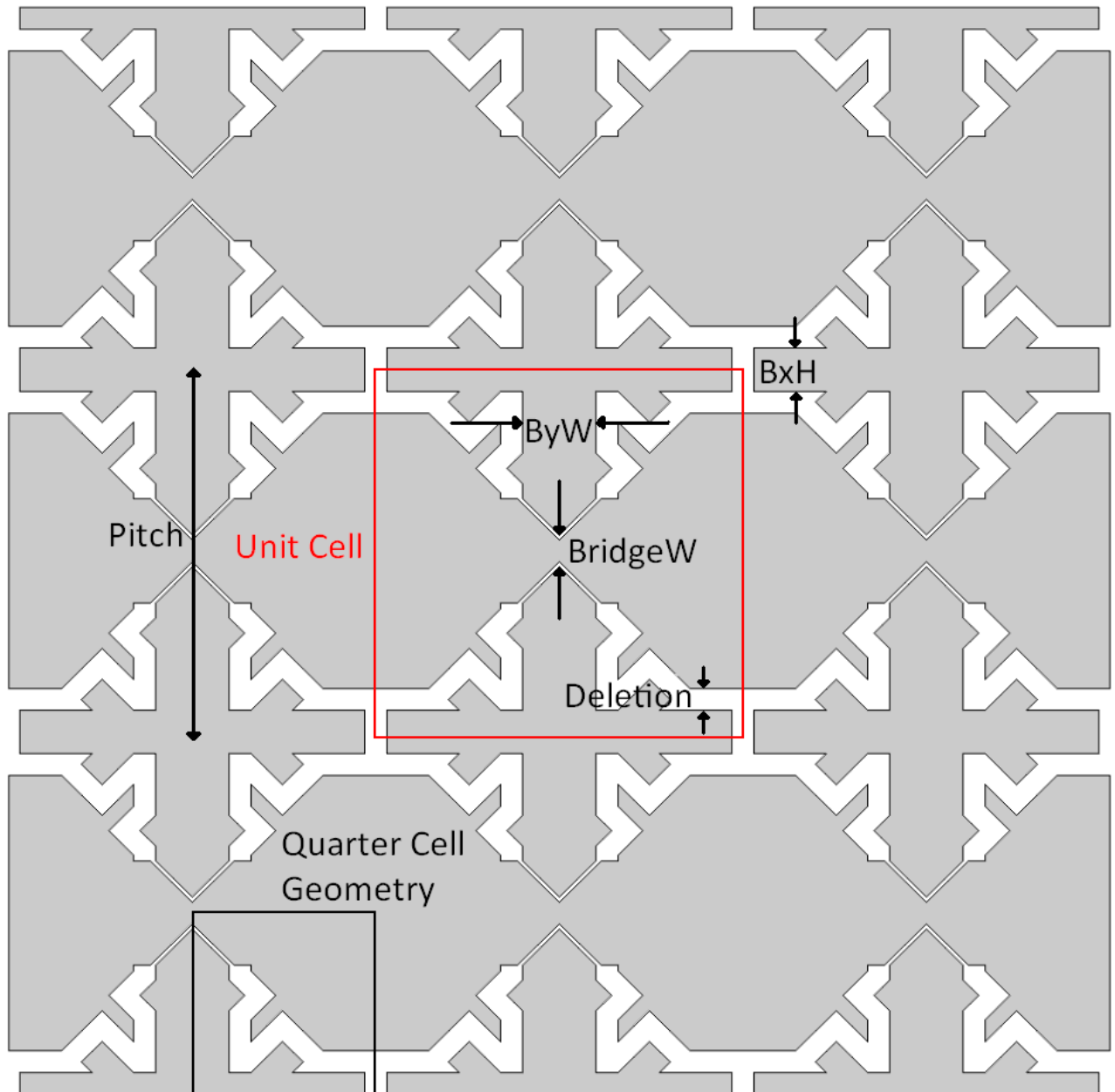


Fig. 3.28 Labelled snowflake pattern layout.

Figures 3.27 and 3.28 show the pattern layout used for the comparative diamond vs snowflake studies. Figure 3.29 shows an equipotential profile obtained from a resulting snowflake simulation. Figures 3.30 gives the stack-up for the GG simulations.

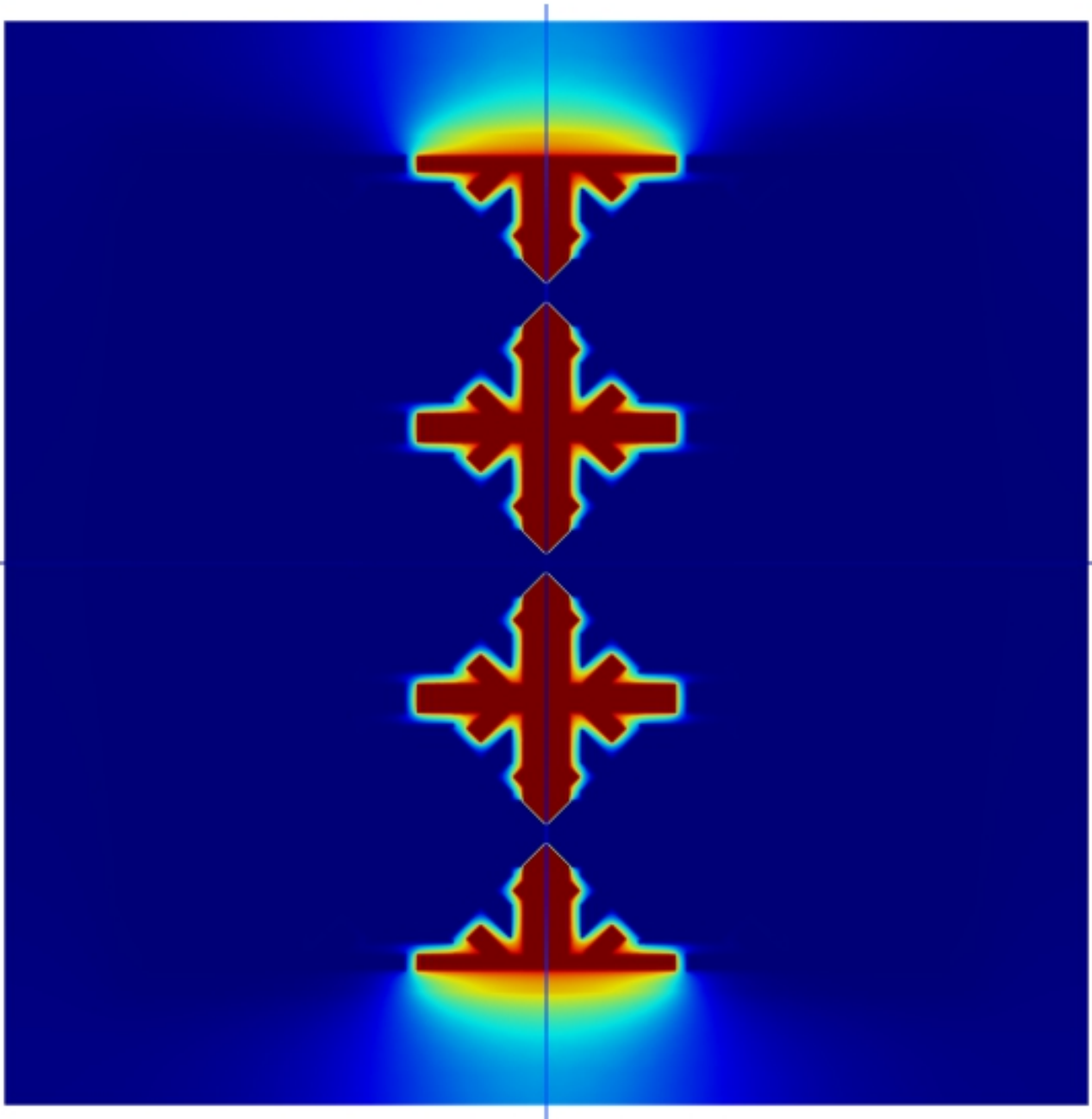


Fig. 3.29 Equipotential surfaces in snowflake simulation domain.

Glass Cover Optical Clear Adhesive ITO Pattern Glass Substrate Copper Tape	Stack-Up: Glass-on-Glass	
	Thickness = 550 μm ,	Dielectric Constant = 7
	Thickness = 100 μm ,	Dielectric Constant = 3.5
	Diamond Pattern	
	Thickness = 550 μm ,	Dielectric Constant = 7
	Thickness = 508 μm ,	Dielectric Constant = 3.64

Fig. 3.30 GG stack-up.

The stack-up used for this comparative study is glass lens on a glass substrate separated by an OCA layer and bonded to 20 mils (508 μm) of grounded copper tape (GG).

The parameters for screening analysis are labelled in the above diagrams. Each has a pitch, deletion and bridge width. The snowflake pattern is unique in that it has two extra parameters which describe the width of the central bars of the Rx electrodes – Y-bar width (ByW) and X-bar height (BxH). The resulting datasets obtained from the parametric sweeps are shown in tables 3.7 and 3.8.

Screening Data for Diamond:

BridgeW (μm)	Cm (pF)	Cm' (pF)	Cp-Tx (pF)	Cp-Rx (pF)	Cf-Tx (pF)	Cf-Rx (pF)	delCm (pF)	SNRd
100	0.54258	0.28009	0.53921	0.56781	1.72607	1.81955	0.26249	0.4622849
150	0.54224	0.27964	0.53537	0.57196	1.71333	1.8346	0.2626	0.459123
200	0.54145	0.27919	0.53125	0.57634	1.69943	1.85	0.26226	0.4550439
250	0.54043	0.27845	0.52684	0.5811	1.68436	1.86569	0.26198	0.4508346
300	0.53834	0.27701	0.52178	0.58635	1.66695	1.88322	0.26133	0.4456894
Deletion (μm)	Cm (pF)	Cm' (pF)	Cp-Tx (pF)	Cp-Rx (pF)	Cf-Tx (pF)	Cf-Rx (pF)	delCm (pF)	SNRd
100	1.02007	0.72157	0.56254	0.57814	1.88338	1.9354	0.2985	0.5163109
200	0.71297	0.42939	0.54955	0.57824	1.80807	1.90444	0.28358	0.4904192
300	0.54145	0.27919	0.53125	0.57634	1.69943	1.85	0.26226	0.4550439
400	0.41689	0.18118	0.50623	0.5725	1.55685	1.77297	0.23571	0.4117205
500	0.32795	0.12038	0.47723	0.56637	1.40141	1.68602	0.20757	0.3664919
Pitch (mm)	Cm (pF)	Cm' (pF)	Cp-Tx (pF)	Cp-Rx (pF)	Cf-Tx (pF)	Cf-Rx (pF)	delCm	SNRd
4	0.39131	0.2043	0.33588	0.38226	1.1582	1.38113	0.18701	0.489222
4.5	0.46884	0.24403	0.42874	0.4741	1.40234	1.59297	0.22481	0.4741827
5	0.54145	0.27919	0.53125	0.57634	1.69943	1.85	0.26226	0.4550439
5.5	0.61499	0.31467	0.64364	0.68883	2.00988	2.12502	0.30032	0.4359857
6	0.6887	0.35031	0.76597	0.81139	2.28682	2.38428	0.33839	0.4170498

Tab. 3.7 Diamond parametric sweep simulation results with calculated key metrics ΔC_m and $\text{SNR}_{\text{DISPLAY}}$.

From these tables, the experimentalist takes a first look at some key relationships. Namely, ΔC_m and SNR. This will give an initial indication as to which pattern is superior in performance. These key metrics are plotted against what are expected to be high-impact parameters – Deletion and Pitch. Deletion is expected to be a high impact parameter as the it directly affects the number of field lines which can penetrate through the ITO layer from the finger to VCOM. It is normally the first suspect in increasing the parasitic capacitance for that reason. As a rule of thumb, increasing Pitch will normally have the effect of increasing ΔC_m . The reason for this being that capacitance is

Screening Data for Snowflake:

BridgeW (μm)	Cm (pF)	Cm' (pF)	Cp-Tx (pF)	Cp-Rx (pF)	Cf-Tx (pF)	Cf-Rx (pF)	delCm (pF)	SNRd (pF)
100	1.1413	0.82229	0.65579	0.47234	2.40118	1.65363	0.31901	0.6753821
200	1.13212	0.8157	0.66499	0.46332	2.43669	1.62011	0.31642	0.6829405
300	1.12161	0.80805	0.67407	0.45445	2.47174	1.58689	0.31356	0.6899769
400	1.10981	0.79941	0.68295	0.4457	2.50672	1.55405	0.3104	0.6964326
500	1.09778	0.79064	0.69171	0.43706	2.53972	1.52122	0.30714	0.702741
ByW (μm)	Cm (pF)	Cm' (pF)	Cp-Tx (pF)	Cp-Rx (pF)	Cf-Tx (pF)	Cf-Rx (pF)	delCm (pF)	SNRd (pF)
500	1.0385	0.73124	0.72075	0.40564	2.63579	1.38767	0.30726	0.7574697
750	1.08255	0.7707	0.69597	0.43151	2.55014	1.4929	0.31185	0.7226947
1000	1.12161	0.80805	0.67407	0.45445	2.47174	1.58689	0.31356	0.6899769
1250	1.15893	0.84523	0.65472	0.47474	2.40193	1.67033	0.3137	0.6607827
1500	1.20002	0.88697	0.63824	0.49217	2.34105	1.74258	0.31305	0.6360607
BxH (μm)	Cm (pF)	Cm' (pF)	Cp-Tx (pF)	Cp-Rx (pF)	Cf-Tx (pF)	Cf-Rx (pF)	delCm (pF)	SNRd (pF)
200	1.11852	0.81605	0.73354	0.39175	2.67228	1.34811	0.30247	0.7720996
400	1.12357	0.81268	0.69983	0.42793	2.55848	1.48386	0.31089	0.7264973
600	1.12161	0.80805	0.67407	0.45445	2.47174	1.58689	0.31356	0.6899769
800	1.10525	0.79196	0.64961	0.47828	2.387	1.6792	0.31329	0.6550347
1000	1.08376	0.77218	0.62445	0.50226	2.29764	1.7725	0.31158	0.620356
Deletion (μm)	Cm (pF)	Cm' (pF)	Cp-Tx (pF)	Cp-Rx (pF)	Cf-Tx (pF)	Cf-Rx (pF)	delCm (pF)	SNRd (pF)
100	1.79288	1.4664	0.72769	0.41006	2.69963	1.44401	0.32648	0.7961762
200	1.32919	1.00748	0.69885	0.43563	2.58056	1.5312	0.32171	0.7384937
300	1.12161	0.80805	0.67407	0.45445	2.47174	1.58689	0.31356	0.6899769
400	0.93564	0.6392	0.63378	0.48358	2.28977	1.66484	0.29644	0.6130113
500	0.87899	0.58943	0.61384	0.49487	2.19196	1.68751	0.28956	0.5851234
Pitch (mm)	Cm (pF)	Cm' (pF)	Cp-Tx (pF)	Cp-Rx (pF)	Cf-Tx (pF)	Cf-Rx (pF)	delCm (pF)	SNRd (pF)
4	0.83555	0.61178	0.40767	0.32931	1.69698	1.26567	0.22377	0.6795117
4.5	0.98396	0.71574	0.53402	0.38888	2.05993	1.4019	0.26822	0.6897243
5	1.12161	0.80805	0.67407	0.45445	2.47174	1.58688	0.31356	0.6899769
5.5	1.25986	0.89925	0.83115	0.52277	2.86847	1.76337	0.36061	0.6898062
6	1.40461	0.99528	1.00696	0.59229	3.2133	1.90579	0.40933	0.6910973

Tab. 3.8 Snowflake parametric sweep simulation results with calculated key metrics ΔC_m and SNR_{DISPLAY} .

dependent on the area of the object holding charge. Increasing the Pitch of the sensor will always increase the area of the ITO electrodes as other factors are held constant. Conversely, bridge width usually has a very small effect as it is geometrically dwarfed by other parameters. Its evaluation is trivial comparatively. As for BxH and ByW, these are new parameters with complex effects yet to be understood. Therefore, it is logical that deletion and pitch are the first parameters to be considered.

Figures 44 and 45 show ΔC_m vs Deletion and Pitch for both sensors patterns. Figures 46 and 47 show SNR vs Deletion and Pitch for both sensors patterns.

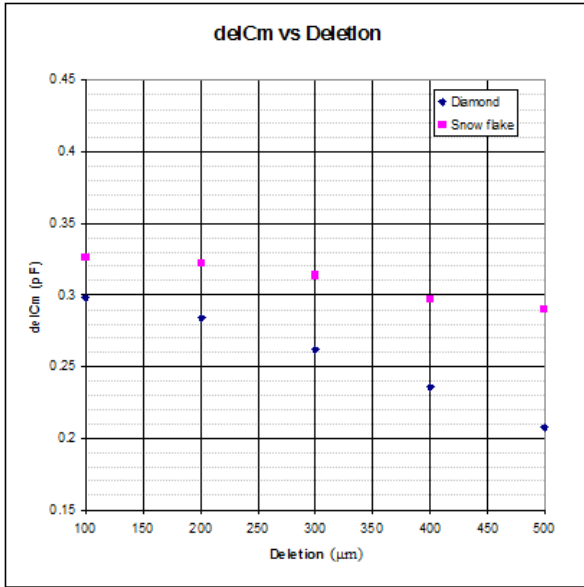


Fig. 3.31 ΔC_m vs deletion for diamond vs snowflake simulations.

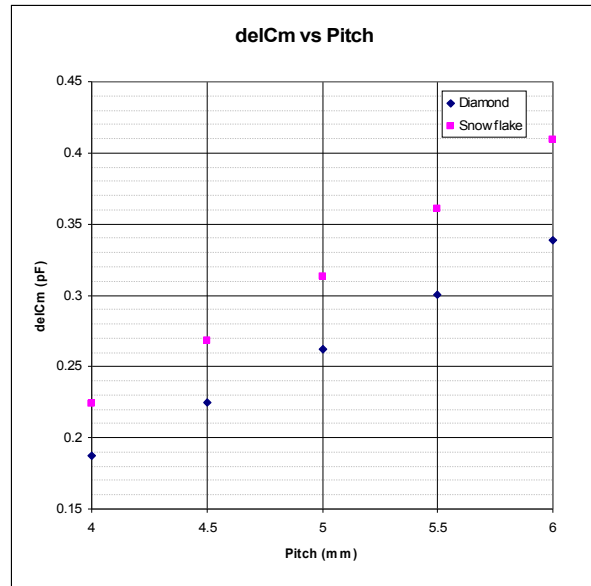


Fig. 3.32 ΔC_m vs pitch for diamond vs snowflake simulations.

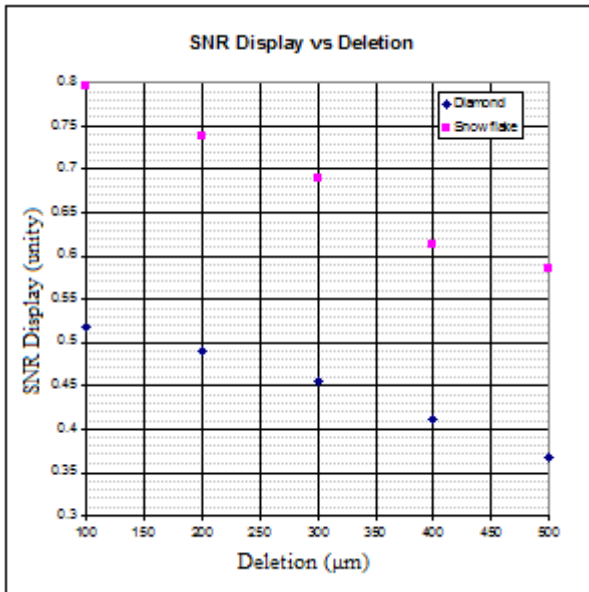


Fig. 3.33 $SNR_{DISPLAY}$ vs deletion for diamond vs snowflake simulations.

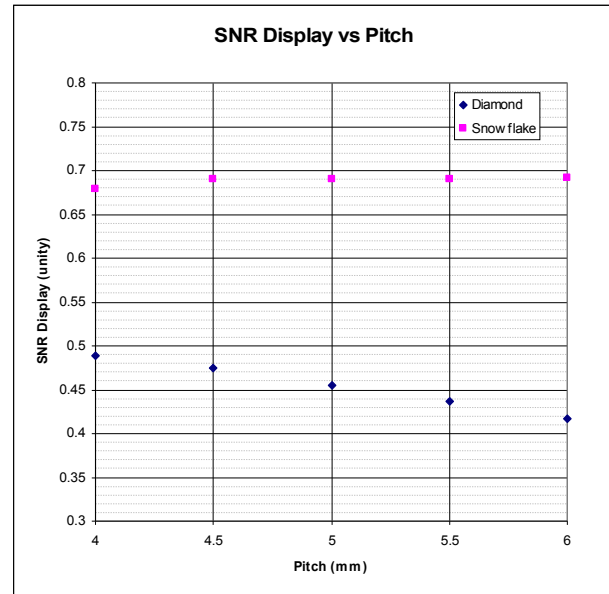


Fig. 3.34 $SNR_{DISPLAY}$ vs pitch for diamond vs snowflake simulations.

Upon inspection of these plots, it can be said that the snowflake design appears to be advantageous in both ΔC_m and SNR. However, the full capacitance matrix should not be ignored. Ideally, all capacitance trends would be observed against each factor. We can use an additional software package – JMP, to create a multivariate plot of each factor against every capacitance. JMP is a statistical software tool used to arrange data and form statistical models. This was the tool available during placement at Cypress Semiconductor. This is used to complete a quick assessment of all trends and can be used to determine the full set of high impact factors. Figures 3.35, 3.36 and 3.37 give the full set of diamond multivariate plots for each of the 3 panel parameters Bridge Width,

Deletion and Pitch, respectively. Figures 3.38, 3.39, 3.40, 3.41 and 3.42 give the full set of snowflake multivariate plots for each of the 5 panel parameters Bridge Width, Deletion, Pitch, BxH and ByW respectively. These plots convert tables 7 and 8 into graphs which correlate all possible combinations of columns in the table, two at a time, simultaneously. It is a useful method of quickly cross referencing one trend against another.

Diamond Multivariate Plots:

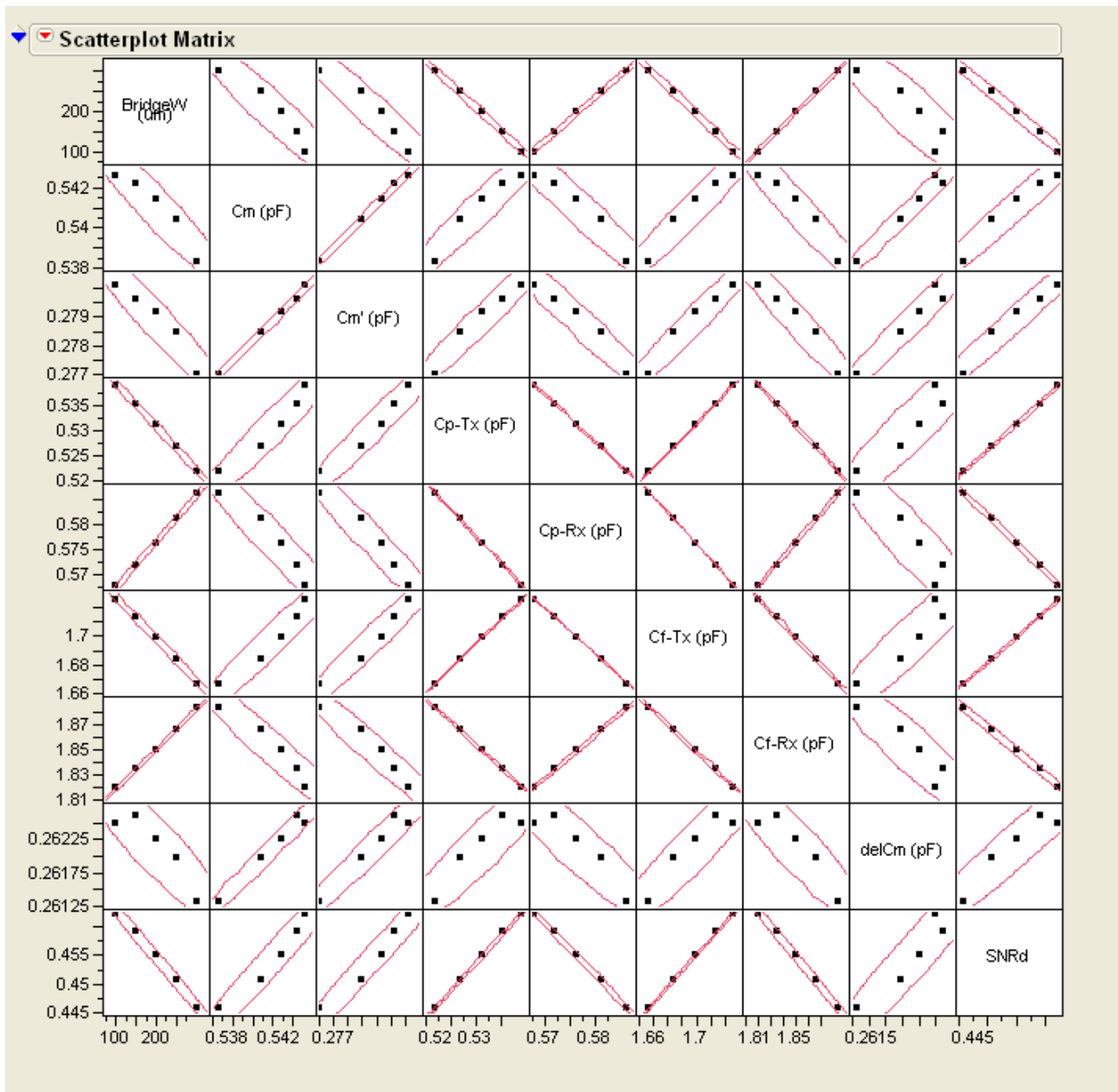


Fig. 3.35 Diamond multivariate plot for bridge width

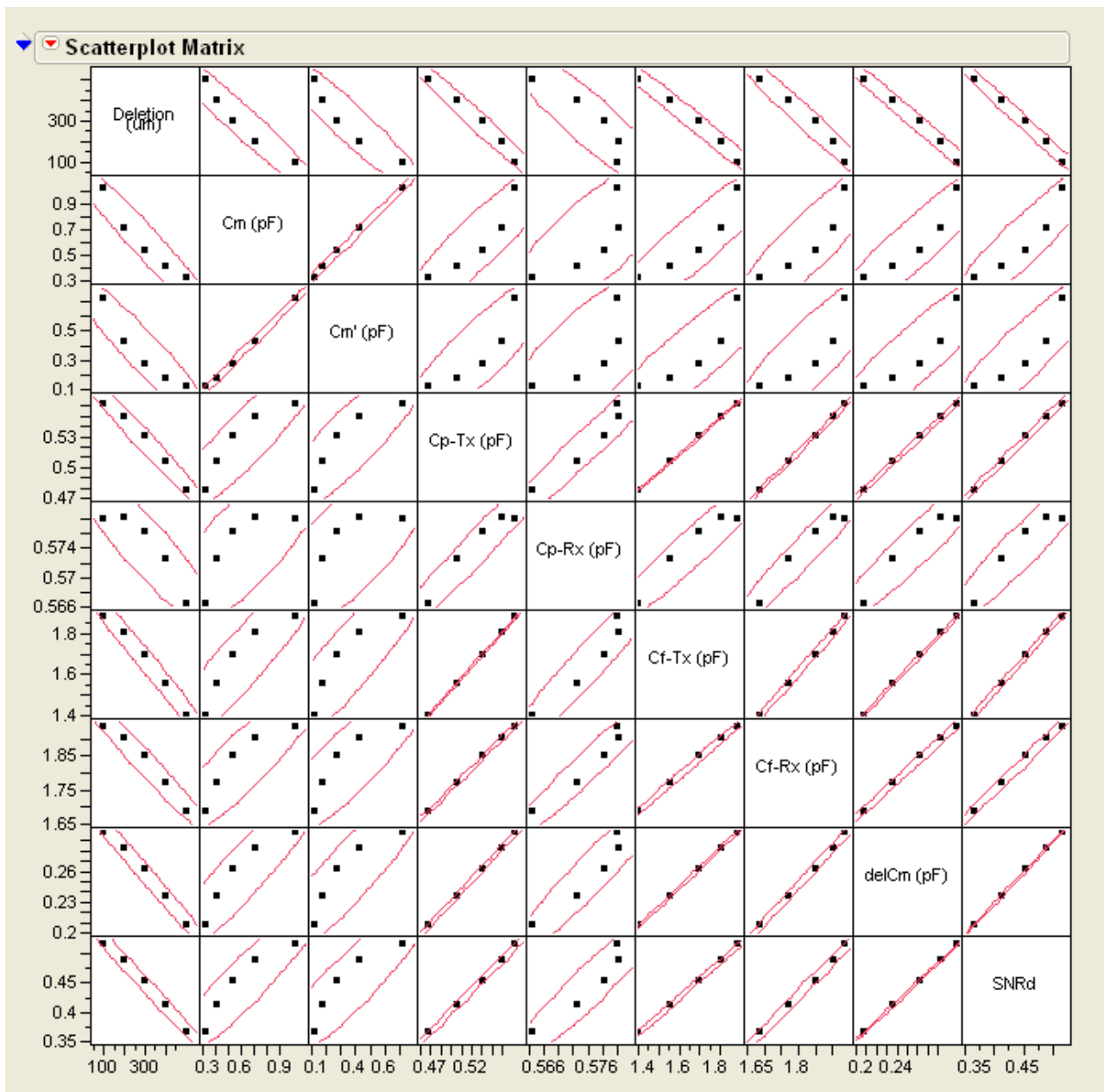


Fig. 3.36 Diamond multivariate plot for deletion.

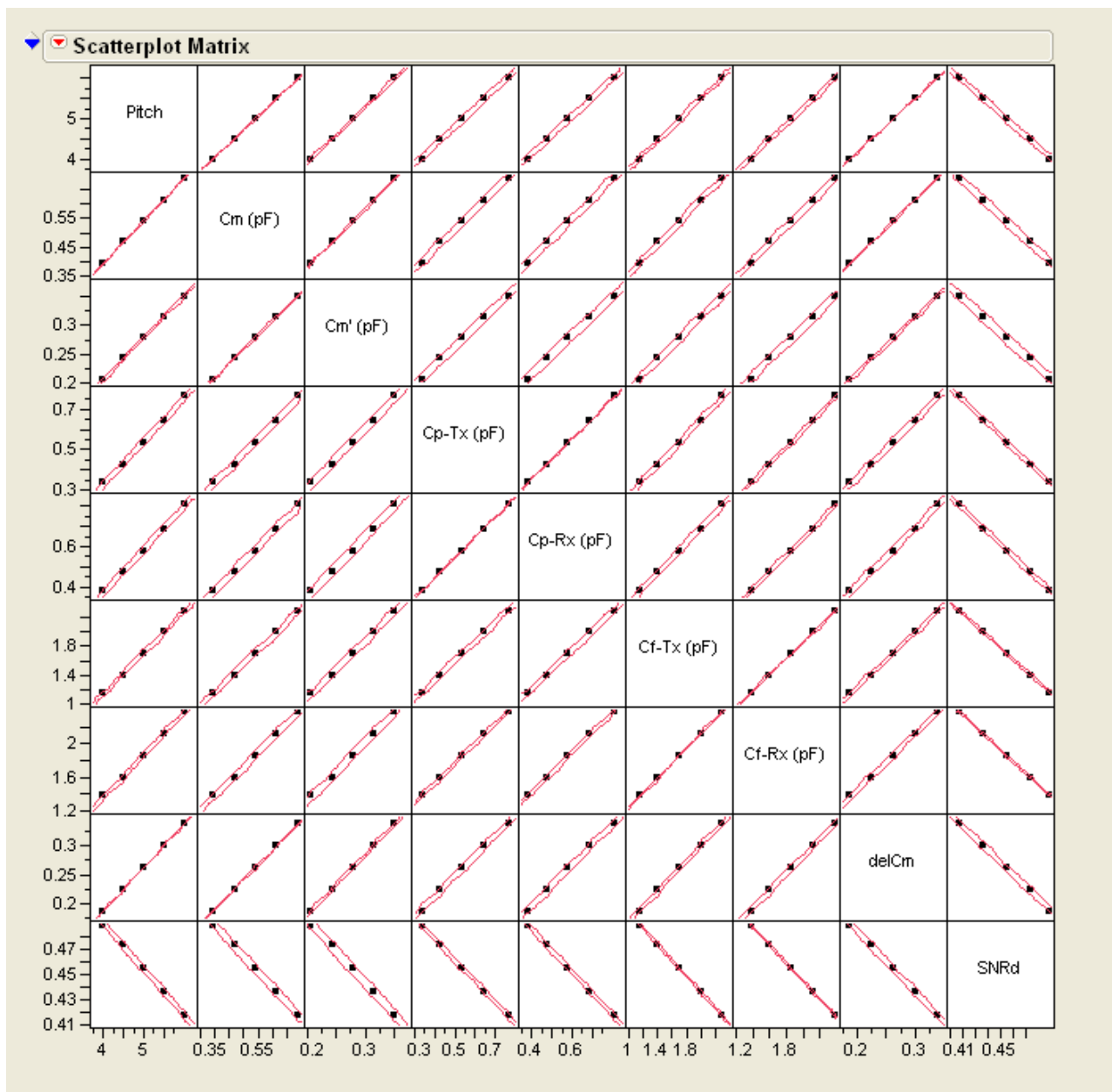


Fig. 3.37 Diamond multivariate plot for pitch.

Snowflake Multivariate Plots:

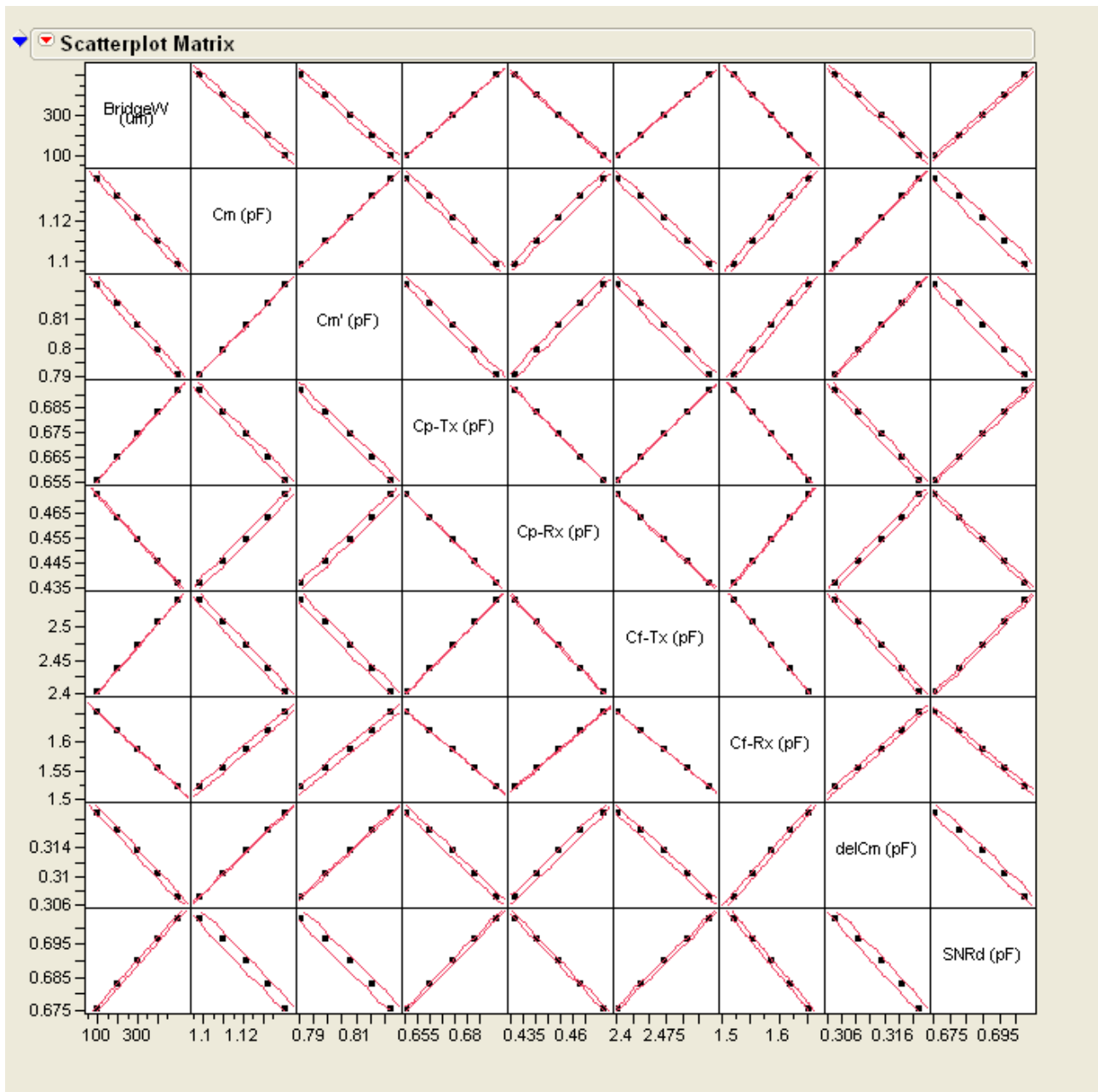


Fig. 3.38 Snowflake multivariate plot for bridge width.

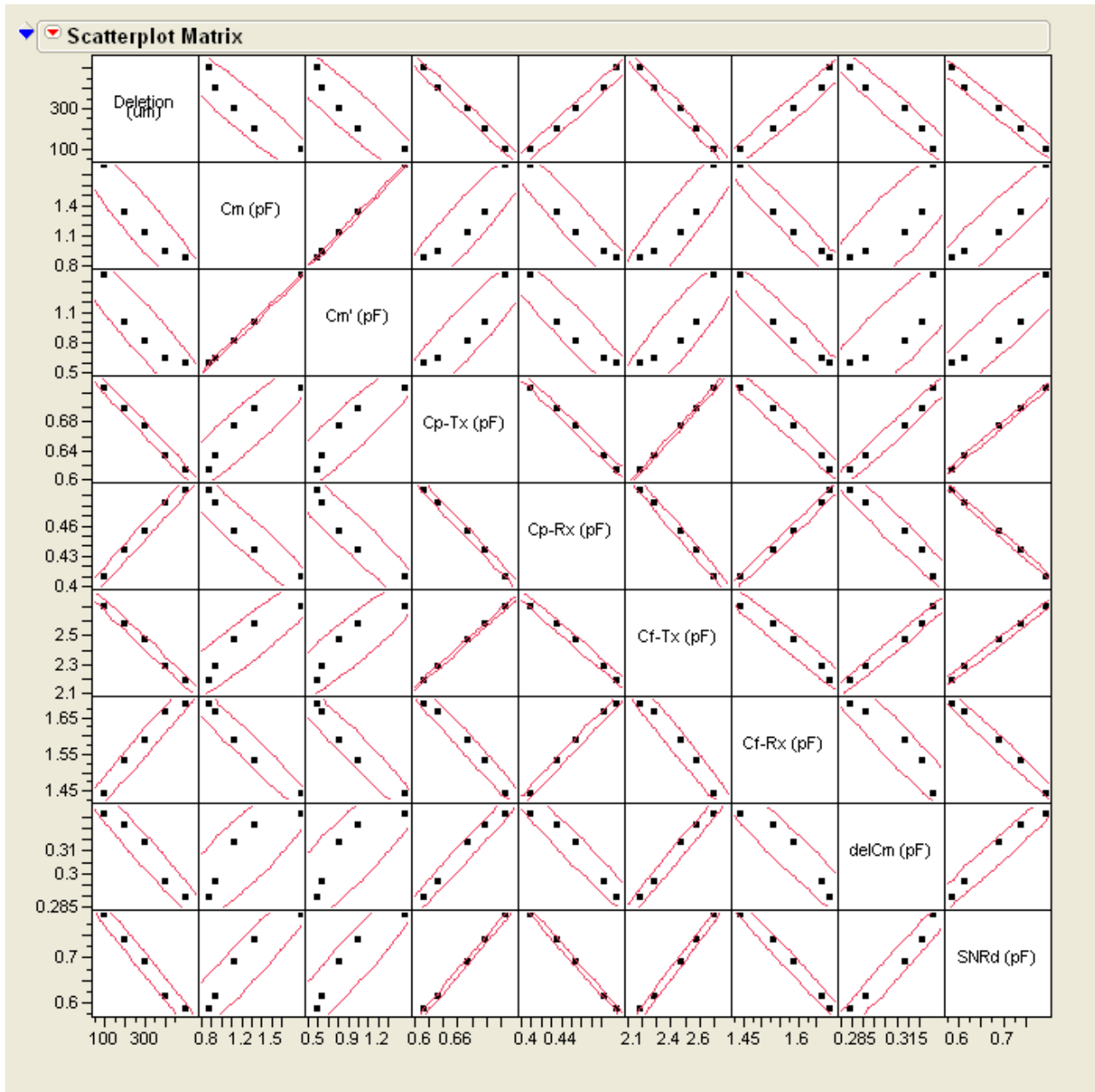


Fig. 3.39 Snowflake multivariate plot for deletion.

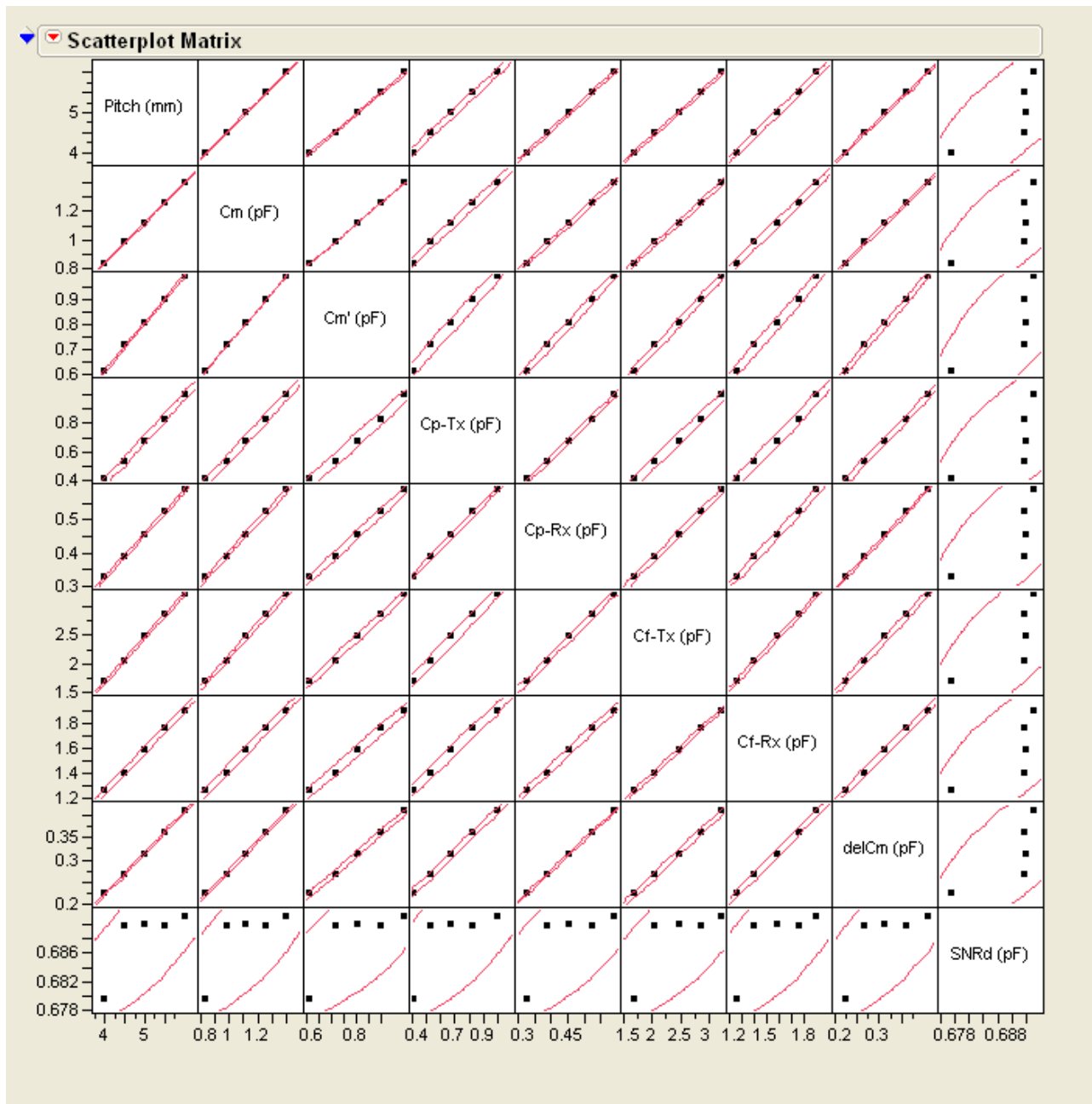


Fig. 3.40 Snowflake multivariate plot for pitch.

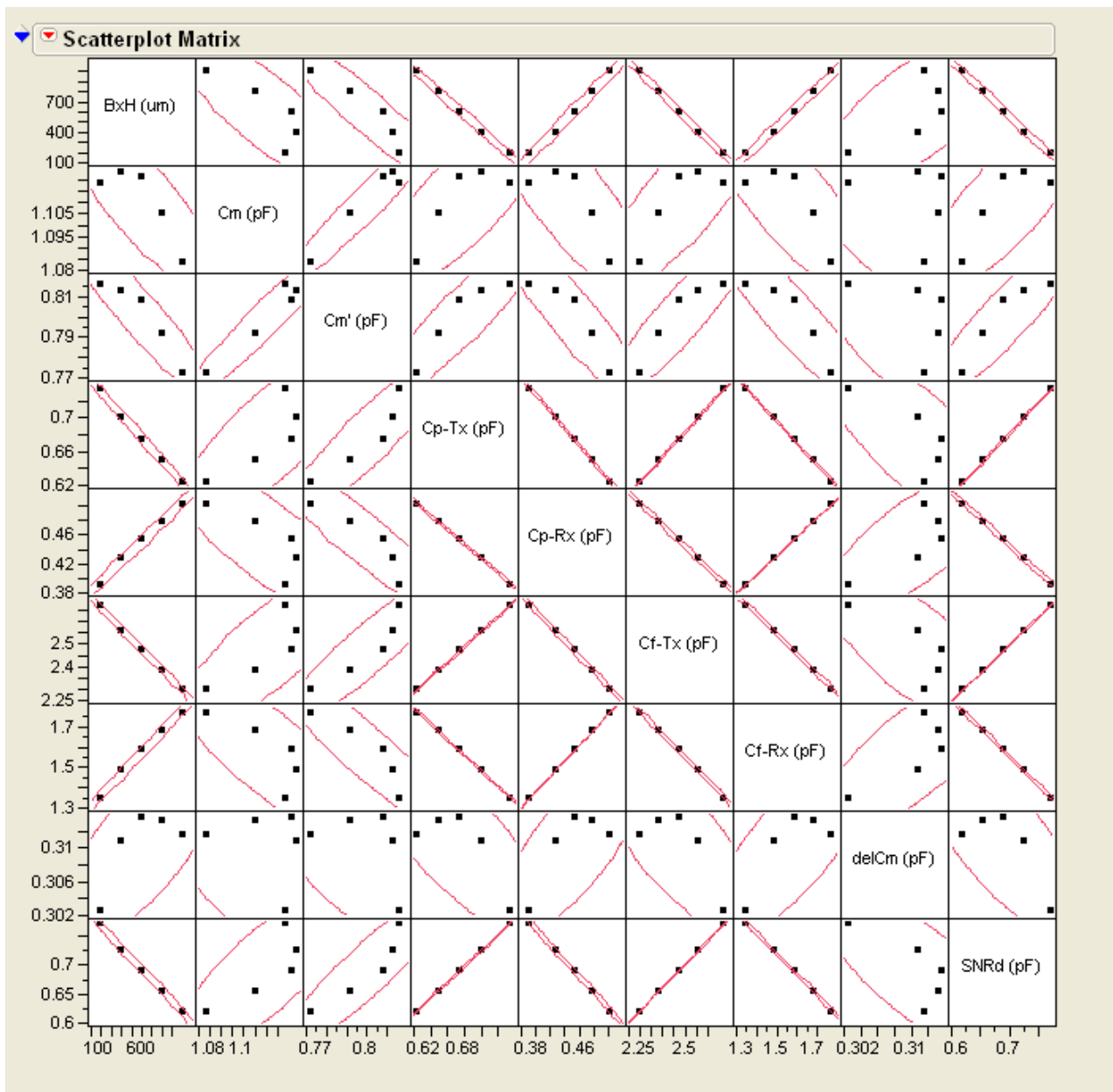


Fig. 3.41 Snowflake multivariate plot for x-bar height.

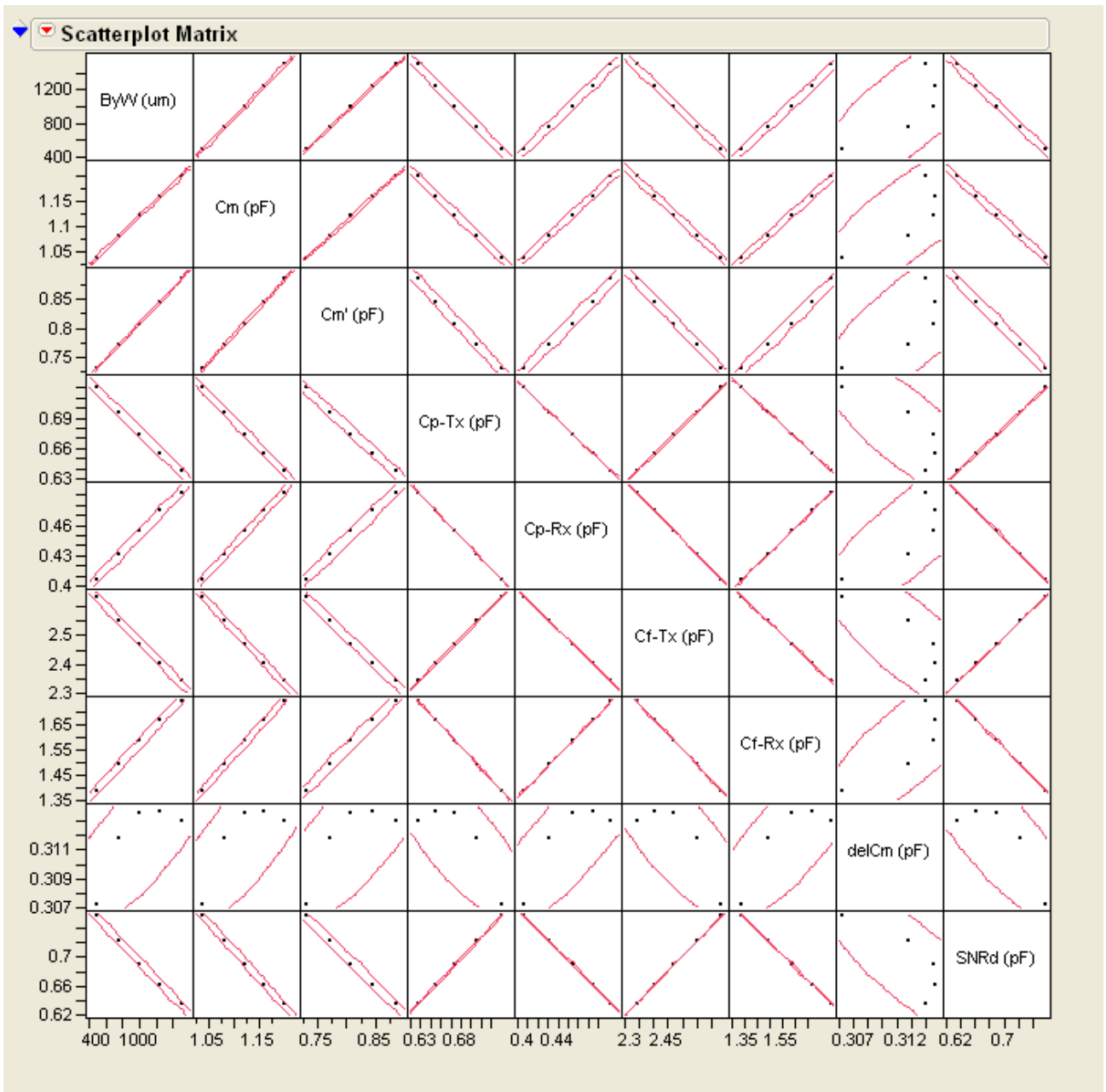


Fig. 3.42 Snowflake multivariate plot for \bar{y} -bar width.

Figures 3.41 and 3.42 are of particular interest. The multivariate plots for BxH and ByW are noteworthy as exhibiting non-linear behaviour is seen. For example, it can be seen that the response of ΔC_m to BxH and ByW is hyperbolic. This suggests that there is an optimal value for each of these parameters which maximizes ΔC_m . However, changing the baseline values of other parameters is sure to impact these values, as this screening analysis holds each factor at a baseline value while the factor of interest is varied. It is therefore inferred that other panel parameters will cause the location of this optimal BxH/ByW value to shift – dramatically changing the profile of the response. Therefore, it is clear that a more rigorous analysis is required in order to fully establish the best design practices for a Snowflake panel TSP.

The snowflake design offers superior ΔC_m and SNR. However, further studies need to be undertaken in order to determine a metric for panel speed (specifically resistance simulations). Also, the selection of ByW and BxH needs to be optimized as these have complex effects on the performance of the panel. A “Design of Experiments” (DOE) for these panels parameters is recommended in order to establish a “best design”. This would create empirical equations for each capacitance response over a predetermined experimental domain. However, a full factorial DOE would be extremely time-consuming. Therefore, this type of screening methodology would be used to identify the highest impact factors only. In the DOE, only these factors would be used. This approach in tandem with a fractional-factor DOE will provide the experimentalist with a dataset set large enough to create equations without the weeks of simulation time a full-factorial DOE would require.

3.4 FEM VS MOM COMPARISON

This work compares the simulation of a diamond-pattern on GG stack-up as simulated by both COMSOL FEM solver and Ansys Q3D MOM solver. Identical models were built in each software package and executed separately on different machines. The FEM simulations were run using a Dell Precision T5500 with 2 machines utilizing 12 Intel Xeon 3.47GHz processors and 48.0 GB of RAM, whereas the MOM simulations were run using on a personal machine with 8 Intel Core i7 2.4GHz processors and 12.0 GB of RAM. Therefore, it is difficult to draw conclusions regarding computational efficiency due to the difference in processing power. However, it is useful to observe the separate simulations and it is a worthwhile demonstration of the Ansys Q3D solver's capabilities.

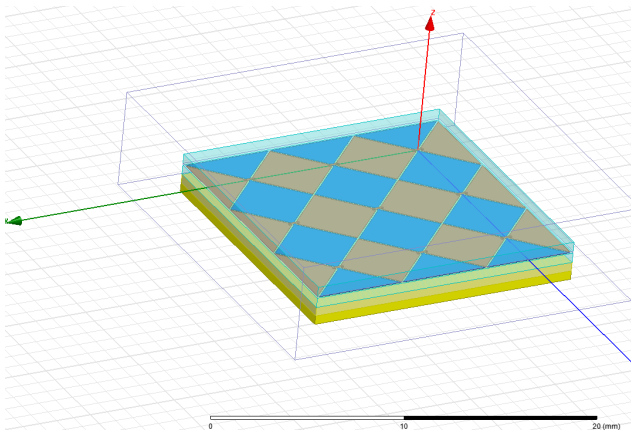


Fig. 3.43 Diamond 3D model in Ansys without finger.

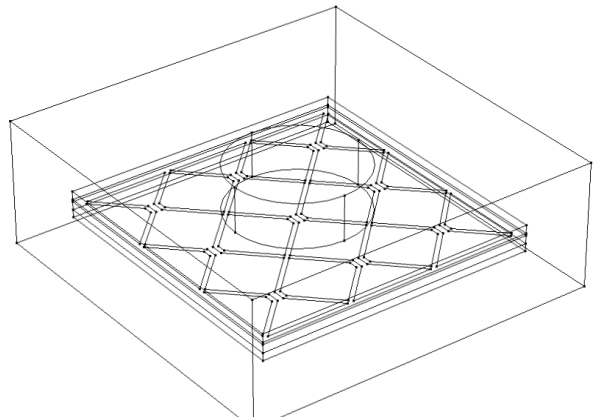


Fig. 3.44 Diamond 3D model in COMSOL with finger.

The parasitic capacitances, C_{pTX} and C_{pRX} were calculated for both the FEM and MOM simulations for a parametric sweep of the Rx bridge width. This should produce a predictable change in both

simulations, as increasing the area of the bridge should directly affect the area of both Rx and Tx electrodes. Figures 3.45 and 3.46 show the results of the experiment.

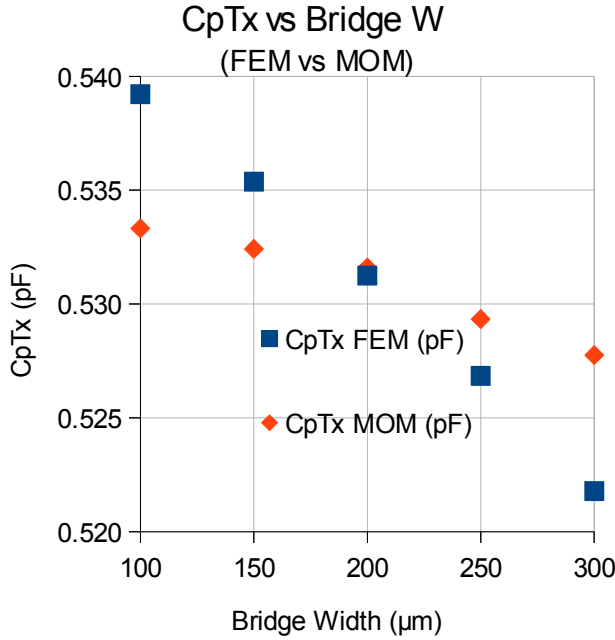


Fig. 3.45 C_{pTx} vs bridge width for FEM vs MOM study.

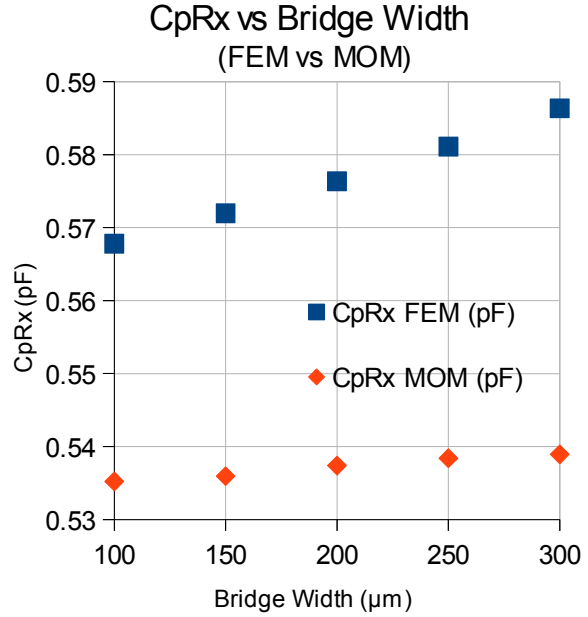


Fig. 3.46 C_{pRx} vs bridge width for FEM vs MOM study.

It can be seen from figures 3.45 and 3.46 that there is a good match for C_{pRx} as the simulations only disagree by about 35fF, and a good match for C_{pTx} as there is only a disagreement of about 5 fF at the extreme ends of the parametric sweep range. The FEM study took 42 mins 36 sec while the MOM study took 1 hour 33 mins 2 seconds. Whether this increase in solving time is due to the dense nature of the MOM matrix or simply due to the fact FEM studies were run on a much more powerful machine can not be said with confidence. However, this experiment shows that both simulation models are consistent and produce results with a high degree of an agreement for an identical sensor.

3.5 SIMULATION SIZE

This work reviews several issues affecting the numerical simulation of capacitive touch screen sensors. The main computational issue identified is the tension between the need for both accuracy and speed. As panels usually comprise a finite array of repeating unit cells a compromise is to only model a smaller array of such cells. A series of numerical experiments are described documenting the effect of changing the number of unit cells retained in the simulation.

In this work, we perform an experimental case study whereby a snowflake diamond-like pattern, inspired by [15], is simulated using the COMSOL FEM solver. The geometry (see figure 3.47) is

built and parametrised for parametric analysis.

There is an ongoing struggle in TSP simulation between the consumption of computational resources and convergence. This means that the larger the simulation space built the longer a simulation will need to generate a solution. In an industry where complex relationships can exist between designers, customers and vendors – deadlines have an unavoidable effect on the validity of any simulation. Therefore, it is important to understand the impact of increasingly larger simulations and the pros and cons. By convention, while a TSP physically consists of a large array of “unit cells” only a small section of the TSP is actually simulated. As more and more unit cells

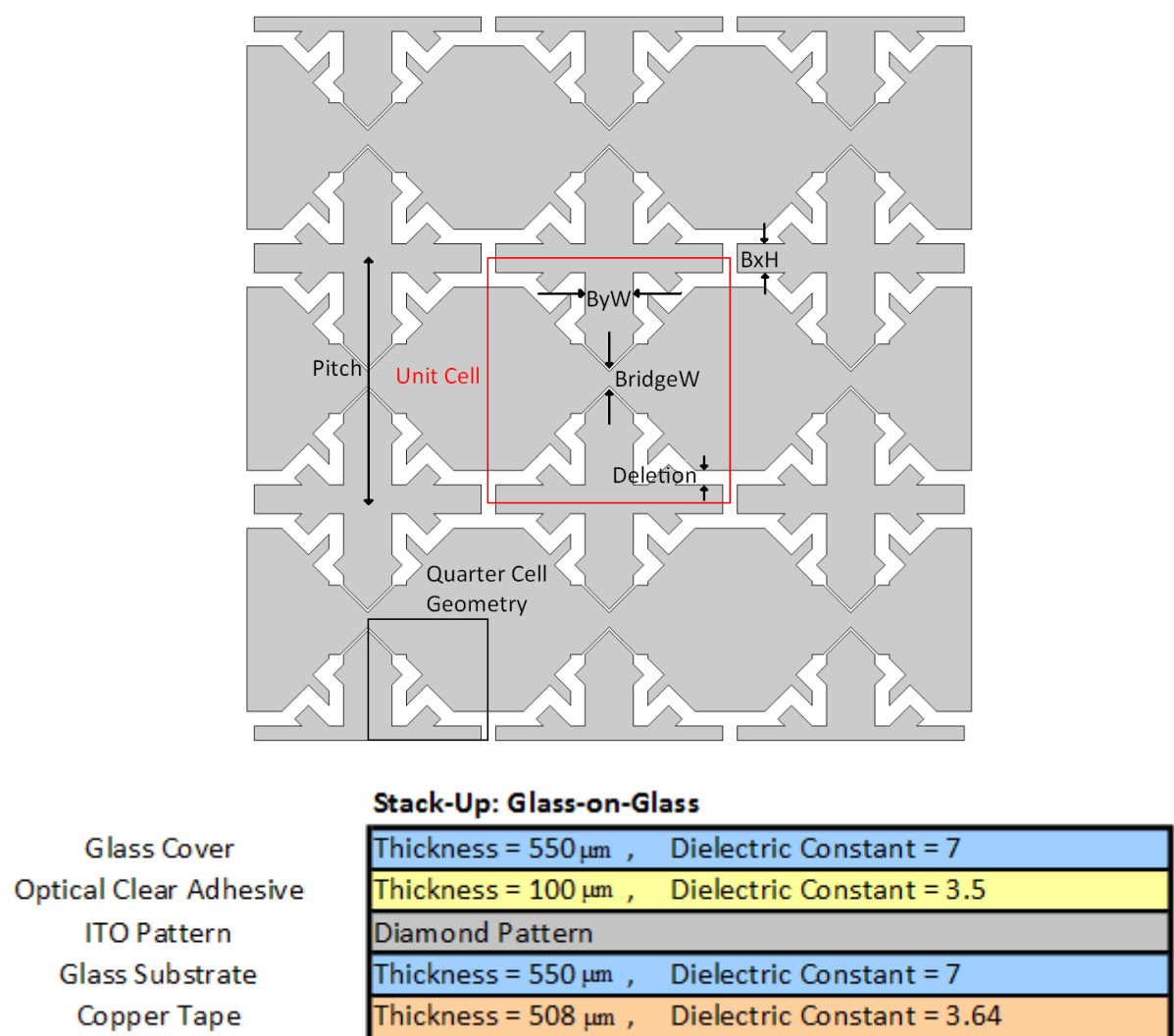


Fig. 3.47 Labeled pattern layout and stack-up for “snowflake” design simulated.

are added for a given element density, the solution time increases. In this work, three snowflake geometries were constructed – 1x1, 3x3 and 5x5. 3D geometries for each simulation are shown in figures 3.48, 3.49 and 3.50.

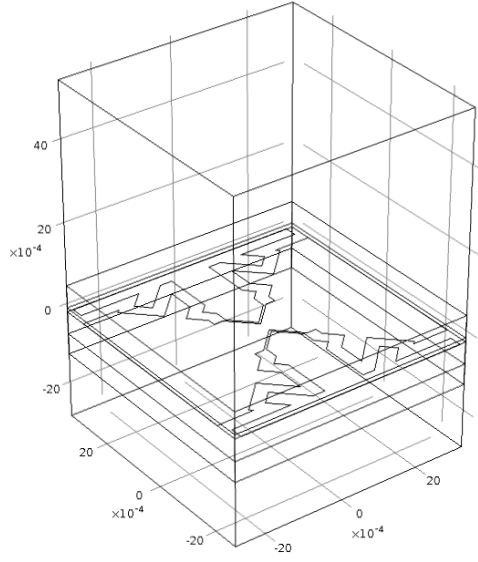


Fig. 3.48 1x1 snowflake geometry.

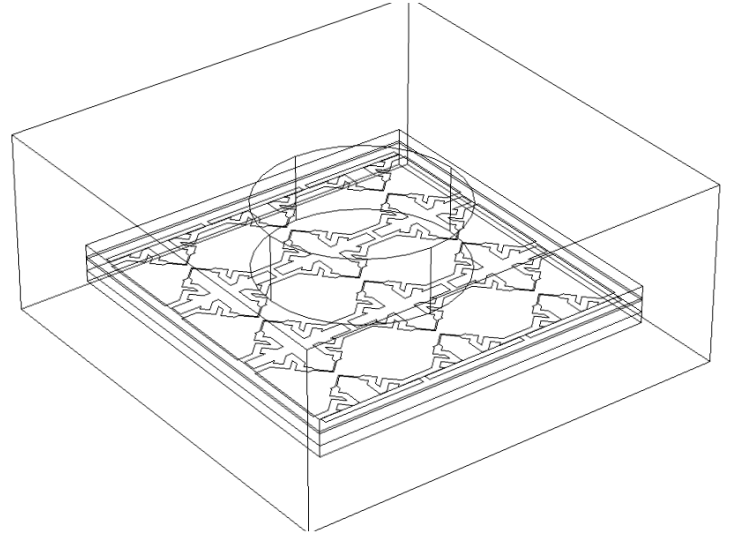


Fig. 3.49 3x3 snowflake geometry with finger.

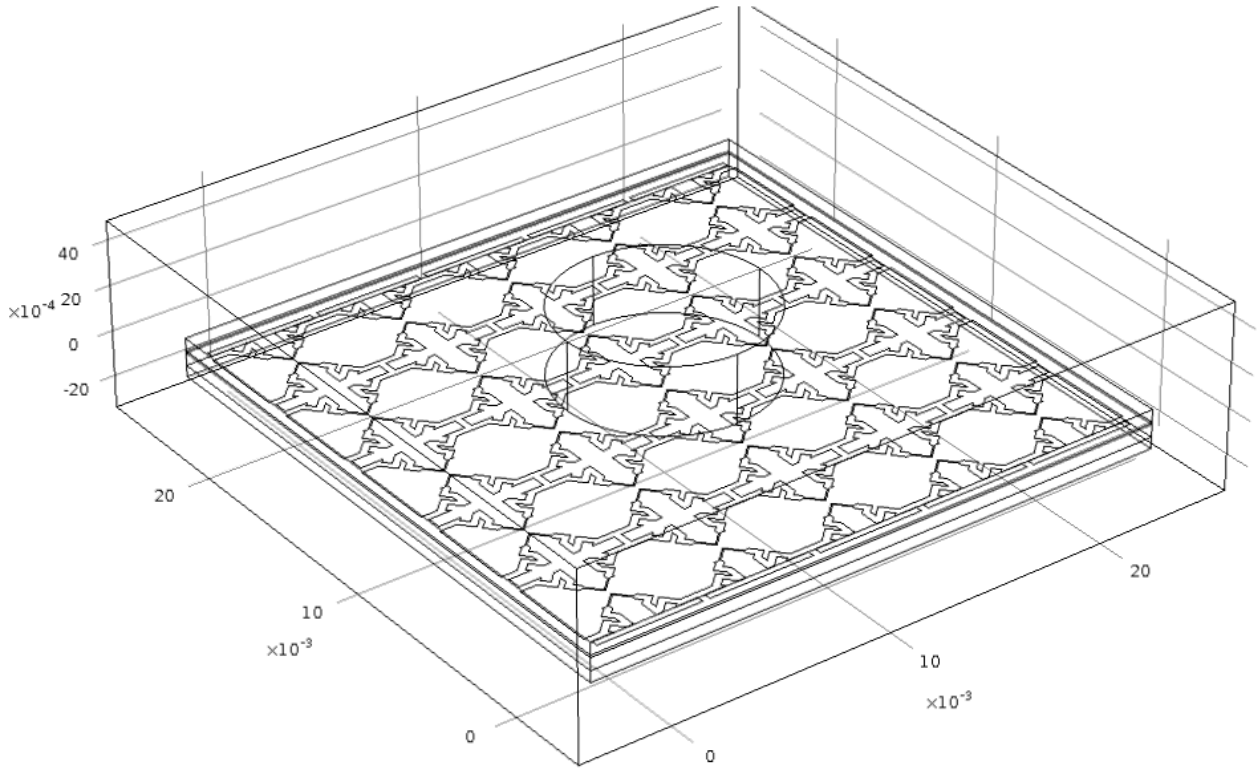


Fig. 3.50 5x5 snowflake geometry with finger.

Tables 3.9, 3.10, and 3.11 give the datasets for the 1x1, 3x3 and 5x5 simulations respectively. Parametric studies of 5 factors are carried and key metrics ΔC_m , $SNR_{display}$ and SNR_{touch} are calculated from the capacitance matrix and added to the tables. Tables 3.9, 3.10 and 3.11 show the full capacitance matrices and key metrics over the parametric sweep ranges for the 1x1, 3x3 and 5x5 simulations, respectively.

1x1 Snowflake (0:16:16)									
Parameters	No Finger Capacitances (pF)			Finger Capacitances (pF)			Metrics		
bridgeW (μm)	Cm	Cp-Tx	Cp-Rx	Cm'	Cf-Tx	Cf-Rx	Δ Cm (pF)	SNRd	SNRt
100	1.14049	0.59527	0.40943	0.82143	1.19255	0.81317	0.31906	0.7792785	0.3923657
200	1.12149	0.604	0.40042	0.80477	1.21122	0.79592	0.31672	0.7909695	0.3979294
300	1.12072	0.61328	0.39193	0.80719	1.22977	0.7787	0.31353	0.7999643	0.4026326
400	1.10886	0.62197	0.38339	0.79847	1.24776	0.76189	0.31039	0.8095934	0.4073948
500	1.09688	0.63062	0.37498	0.78979	1.26558	0.74521	0.30709	0.8189503	0.4120852
ByW (μm)	Cm	Cp-Tx	Cp-Rx	Cm'	Cf-Tx	Cf-Rx	Δ Cm (pF)	SNRd	SNRt
500	1.03747	0.65933	0.34439	0.73033	1.31928	0.68051	0.30714	0.8918377	0.451338
750	1.0816	0.63485	0.36963	0.76983	1.27178	0.73246	0.31177	0.8434651	0.4256478
1000	1.12072	0.61328	0.39193	0.80719	1.22977	0.7787	0.31353	0.7999643	0.4026326
1250	1.14852	0.5939	0.41138	0.84434	1.19261	0.8199	0.30418	0.7394137	0.3709965
1500	1.18939	0.57772	0.42829	0.88609	1.16123	0.85551	0.3033	0.708165	0.3545254
BxH (μm)	Cm	Cp-Tx	Cp-Rx	Cm'	Cf-Tx	Cf-Rx	Δ Cm (pF)	SNRd	SNRt
200	1.11762	0.66751	0.33517	0.81532	1.33273	0.66123	0.3023	0.9019304	0.4571783
400	1.11434	0.63606	0.3671	0.81016	1.27118	0.72124	0.30418	0.8286026	0.4217459
600	1.12072	0.61328	0.39193	0.80719	1.22977	0.7787	0.31353	0.7999643	0.4026326
800	1.10286	0.5913	0.41424	0.79121	1.18645	0.82429	0.31165	0.7523416	0.378083
1000	1.07931	0.5687	0.43696	0.77139	1.14137	0.87045	0.30792	0.7046869	0.3537481
d (μm)	Cm	Cp-Tx	Cp-Rx	Cm'	Cf-Tx	Cf-Rx	Δ Cm (pF)	SNRd	SNRt
100	1.77882	0.6647	0.34896	1.47337	1.35122	0.70869	0.30545	0.8753152	0.4310065
200	1.32061	0.63683	0.37334	1.00677	1.28779	0.75145	0.31384	0.8406278	0.4176459
300	1.12072	0.61328	0.39193	0.80719	1.22976	0.7787	0.31353	0.7999643	0.4026326
400	0.92941	0.57422	0.42064	0.63837	1.13496	0.81697	0.29104	0.6918981	0.3562432
500	0.87495	0.55571	0.43218	0.58874	1.08605	0.82811	0.28621	0.6622472	0.3456183
Pitch (mm)	Cm	Cp-Tx	Cp-Rx	Cm'	Cf-Tx	Cf-Rx	Δ Cm (pF)	SNRd	SNRt
4	0.82866	0.36216	0.2797	0.61143	0.72373	0.55468	0.21723	0.7766536	0.3916312
4.5	0.97858	0.48077	0.33286	0.71521	0.96316	0.66137	0.26337	0.7912336	0.3982188
5	1.12072	0.61328	0.39193	0.80719	1.22976	0.7787	0.31353	0.7999643	0.4026326
5.5	1.25887	0.76267	0.45384	0.89806	1.53027	0.90116	0.36081	0.7950159	0.4003839
6	1.39889	0.93071	0.51695	0.99349	1.86849	1.02586	0.4054	0.7842151	0.3951806

Tab. 3.9 Data for the 1x1 parametric study.

3x3 Snowflake (1:45:12)									
Parameters	No Finger Capacitances			Finger Capacitances			Metrics		
bridgeW (μm)	Cm	Cp-Tx	Cp-Rx	Cm'	Cf-Tx	Cf-Rx	delCm	SNRd	SNRt
100	1.1413	0.65579	0.47234	0.82229	2.40118	1.65363	0.31901	0.6753821	0.192915
200	1.13212	0.66499	0.46332	0.8157	2.43669	1.62011	0.31642	0.6829405	0.1953077
300	1.12161	0.67407	0.45445	0.80805	2.47174	1.58689	0.31356	0.6899769	0.197594
400	1.10981	0.68295	0.4457	0.79941	2.50672	1.55405	0.3104	0.6964326	0.1997362
500	1.09778	0.69171	0.43706	0.79064	2.53972	1.52122	0.30714	0.702741	0.2019037
ByW (μm)	Cm	Cp-Tx	Cp-Rx	Cm'	Cf-Tx	Cf-Rx	delCm	SNRd	SNRt
500	1.0385	0.72075	0.40564	0.73124	2.63579	1.38767	0.30726	0.7574697	0.2214215
750	1.08255	0.69597	0.43151	0.7707	2.55014	1.4929	0.31185	0.7226947	0.2088887
1000	1.12161	0.67407	0.45445	0.80805	2.47174	1.58689	0.31356	0.6899769	0.197594
1250	1.15893	0.65472	0.47474	0.84523	2.40193	1.67033	0.3137	0.6607827	0.1878072
1500	1.20002	0.63824	0.49217	0.88697	2.34105	1.74258	0.31305	0.6360607	0.1796474
BxH (μm)	Cm	Cp-Tx	Cp-Rx	Cm'	Cf-Tx	Cf-Rx	delCm	SNRd	SNRt
200	1.11852	0.73354	0.39175	0.81605	2.67228	1.34811	0.30247	0.7720996	0.224366
400	1.12357	0.69983	0.42793	0.81268	2.55848	1.48386	0.31089	0.7264973	0.2095144
600	1.12161	0.67407	0.45445	0.80805	2.47174	1.58689	0.31356	0.6899769	0.197594
800	1.10525	0.64961	0.47828	0.79196	2.387	1.6792	0.31329	0.6550347	0.186571
1000	1.08376	0.62445	0.50226	0.77218	2.29764	1.7725	0.31158	0.620356	0.1757856
d (μm)	Cm	Cp-Tx	Cp-Rx	Cm'	Cf-Tx	Cf-Rx	delCm	SNRd	SNRt
100	1.79288	0.72769	0.41006	1.4664	2.69963	1.44401	0.32648	0.7961762	0.2260926
200	1.32919	0.69885	0.43563	1.00748	2.58056	1.5312	0.32171	0.7384937	0.2101032
300	1.12161	0.67407	0.45445	0.80805	2.47174	1.58689	0.31356	0.6899769	0.197594
400	0.93564	0.63378	0.48358	0.6392	2.28977	1.66484	0.29644	0.6130113	0.1780592
500	0.87899	0.61384	0.49487	0.58943	2.19196	1.68751	0.28956	0.5851234	0.1715901
Pitch (mm)	Cm	Cp-Tx	Cp-Rx	Cm'	Cf-Tx	Cf-Rx	delCm	SNRd	SNRt
4	0.83555	0.40767	0.32931	0.61178	1.69698	1.26567	0.22377	0.6795117	0.1767996
4.5	0.98396	0.53402	0.38888	0.71574	2.05993	1.4019	0.26822	0.6897243	0.1913261
5	1.12161	0.67407	0.45445	0.80805	2.47174	1.58688	0.31356	0.6899769	0.1975953
5.5	1.25986	0.83115	0.52277	0.89925	2.86847	1.76337	0.36061	0.6898062	0.2045005
6	1.40461	1.00696	0.59229	0.99528	3.2133	1.90579	0.40933	0.6910973	0.2147823

Tab. 3.10 Data for the 3x3 parametric study.

5x5 Snowflake (2:07:57)									
Parameters	No Finger Capacitances			Finger Capacitances			Metrics		
bridgeW (um)	Cm	Cp-Tx	Cp-Rx	Cm'	Cf-Tx	Cf-Rx	delCm	SNRd	SNRt
100	1.14883	0.63105	0.447168	0.82979	2.40476	1.65439	0.31904	0.7134679	0.1928445
200	1.14304	0.640104	0.438432	0.8266	2.44044	1.62194	0.31644	0.7217539	0.1950997
300	1.13262	0.649272	0.429456	0.81909	2.476	1.58773	0.31353	0.7300631	0.1974706
400	1.12042	0.658224	0.420612	0.80999	2.51059	1.55435	0.31043	0.7380436	0.1997169
500	1.10983	0.666942	0.412248	0.80261	2.54445	1.5218	0.30722	0.745231	0.2018794
ByW (um)	Cm	Cp-Tx	Cp-Rx	Cm'	Cf-Tx	Cf-Rx	delCm	SNRd	SNRt
500	1.06491	0.695826	0.38136	0.7576	2.64217	1.38875	0.30731	0.8058265	0.2212853
750	1.09317	0.671046	0.40683	0.78131	2.55429	1.49369	0.31186	0.766561	0.208785
1000	1.13262	0.649272	0.429456	0.81909	2.476	1.58773	0.31353	0.7300631	0.1974706
1250	1.16762	0.63009	0.449514	0.85395	2.40534	1.67172	0.31367	0.6977981	0.1876331
1500	1.20586	0.613848	0.466554	0.89287	2.34464	1.74317	0.31299	0.6708548	0.1795522
BxH (um)	Cm	Cp-Tx	Cp-Rx	Cm'	Cf-Tx	Cf-Rx	delCm	SNRd	SNRt
200	1.12871	0.70692	0.368892	0.82635	2.67798	1.34745	0.30236	0.8196437	0.2243942
400	1.15227	0.674358	0.403686	0.84093	2.56422	1.48465	0.31134	0.771243	0.209706
600	1.13262	0.649272	0.429456	0.81909	2.476	1.58773	0.31353	0.7300631	0.1974706
800	1.12803	0.62595	0.452682	0.81483	2.39162	1.68094	0.3132	0.6918764	0.1863243
1000	1.09046	0.60162	0.476118	0.77921	2.30067	1.77386	0.31125	0.6537245	0.1754648
d (um)	Cm	Cp-Tx	Cp-Rx	Cm'	Cf-Tx	Cf-Rx	delCm	SNRd	SNRt
100	1.81158	0.701922	0.385368	1.48574	2.70246	1.44199	0.32584	0.8455295	0.2259655
200	1.34905	0.67359	0.410562	1.02764	2.58409	1.5303	0.32141	0.7828537	0.2100307
300	1.13262	0.649272	0.429456	0.81909	2.476	1.58773	0.31353	0.7300631	0.1974706
400	0.93996	0.609312	0.459036	0.64339	2.29286	1.66956	0.29657	0.6460713	0.1776336
500	0.88517	0.589932	0.470868	0.59505	2.19559	1.69497	0.29012	0.6161387	0.1711653
Pitch (mm)	Cm	Cp-Tx	Cp-Rx	Cm'	Cf-Tx	Cf-Rx	delCm	SNRd	SNRt
4	0.83902	0.388872	0.309768	0.61561	1.70573	1.2714	0.22341	0.7212172	0.1757197
4.5	0.98621	0.512262	0.366456	0.71839	2.06531	1.40284	0.26782	0.7308381	0.1909127
5	1.13262	0.649272	0.429456	0.81909	2.476	1.58773	0.31353	0.7300631	0.1974706

Tab. 3.11 Data for the 5x5 parametric study.

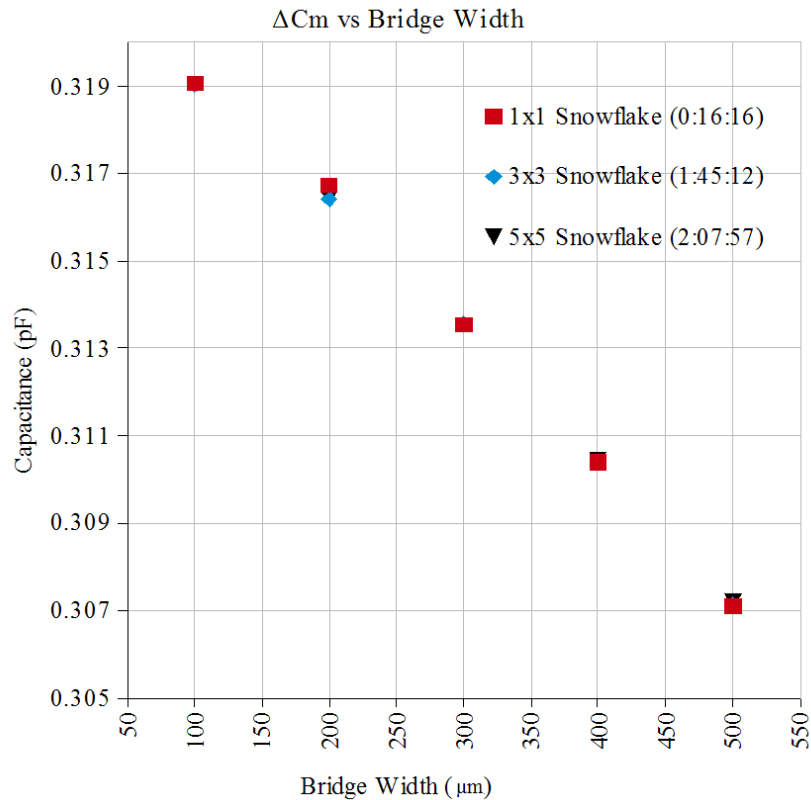


Fig. 3.51 ΔC_m vs bridge width for 1x1, 3x3 and 5x5 simulation. There is no change in the calculation of ΔC_m as the size of the simulation increased with respect to increasing bridge width – the study has converged.

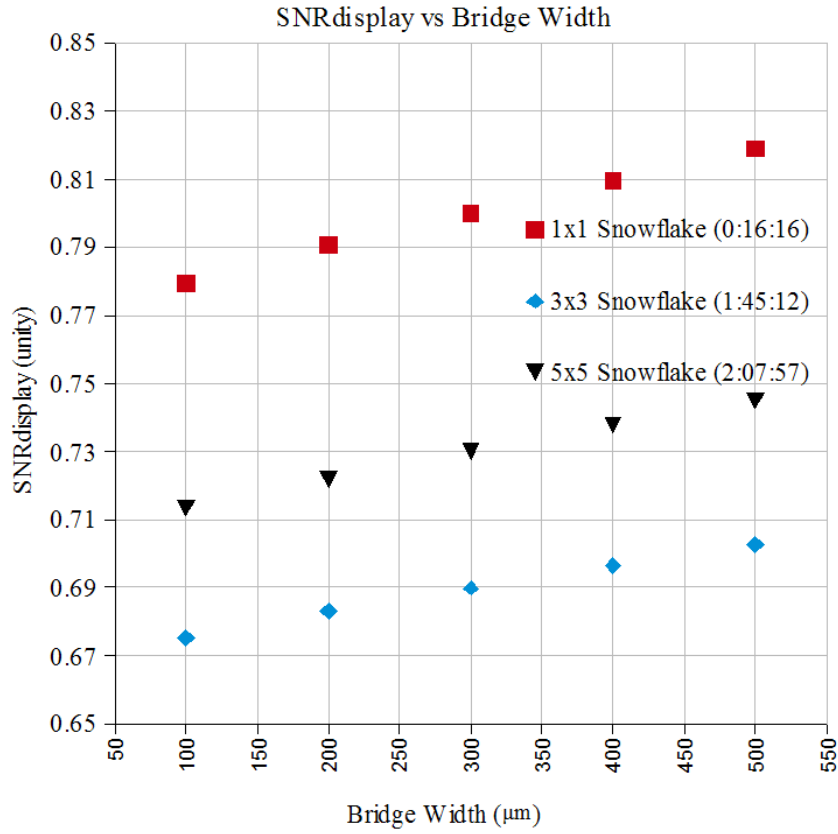


Fig. 3.52 $SNR_{display}$ vs bridge width for 1x1, 3x3 and 5x5 simulation. There is a significant increase in the convergence of the calculation of $SNR_{display}$ as the size of the simulation increased with respect to increasing bridge width..

Figures 3.51 and 3.52 show the effect of an increasing large computational domain on both convergence and solution time, with respect to increasing bridge width size in the TSP. Computation run times are given in parentheses in the legend. In this case, it can be seen that the calculation of ΔC_m is virtually unchanged by expending additional computational resources. However, this is not necessarily true for all parameters (ByW, BxH, Pitch, d). It can also be seen that the calculation of $SNR_{display}$ appears to converge with a larger computational domain. Note the decrease in the change in $SNR_{display}$ between simulations of increasing computational size. This *points towards* good convergence in a hypothetical 7x7 simulation. However, there is no proof the simulations will converge for 7x7, 9x9, 11x11 etc. This is because the means to simulate these huge domains are not at the disposal of this project. This is due to the vast computational resources which would be required in order to run these simulations. The resources required would involve extremely fast processors using hundreds of GBs of RAM.

The full set of simulations reveal that the highest impact parameters of the snowflake panel design with regard to ΔC_m , are the pitch of the sensor and the deletion between the electrodes. Bridge width and bar thicknesses (BxH, ByW) have a very small impact. It is also shown that increasing

bridge width and pitch both have a positive effect on $SNR_{display}$ and SNR_{touch} , while increasing deletion and bar thicknesses has a negative effect and creates a noisier circuit. It is also possible to determine a rough estimate for panel speed using the RC constant described by equation (40). However, a far more accurate calculation of panel speed can be provided by using a full circuit simulation via LTSPICE or similar software. This can take into account screen size and number of columns and rows of electrodes for a bespoke TSP. Output data from electrostatic FEM simulations (parasitic, finger and mutual capacitances) becomes input data for advanced circuit simulations. This can yield a high accuracy measurement of panel speed - a critical parameter in TSP chip design.

The 1x1, 3x3 and 5x5 arrays all exhibit advantages and disadvantages. A 1x1 simulation is extremely quick and yields a converged prediction of ΔC_m resulting in a high level of confidence. Designers are constantly partnering with new vendors of varying processing capabilities. In such an environment, the need to accurately and quickly predict the response of ΔC_m - the primary sensing metric, is paramount. A 1x1 simulation for a complex geometry would be highly favorable in the case of process variation and uniformity testing. A 5x5 is computationally exhaustive but offers a high degree of accuracy for SNR calculations. It is also the simulation of choice for finger position studies, as a large domain is required to accommodate the movement of a finger. 3x3 provides the most reasonable model for testing new designs. It is highly accurate and relatively fast – representing the best compromise in terms of computational efficiency. The 1x1 snowflake simulation is 6.7 times faster than the 3x3 and would have been 16.7 times faster than a 5x5 simulation of equal mesh density. However, these time savings must also be balanced against the convergence and the purpose of the simulation. It is also worthwhile to note that to attain a fully converged study for $SNR_{display}$ larger arrays would have to be constructed 7x7 and 9x9 simulations would be extremely memory consuming and would most likely require advanced networking techniques such as cloud resources or a linked local network.

3.6 DESIGN OF EXPERIMENTS

As mentioned previously in chapter 3.1, the experimentalist would like to analyze the effect of varying all panel parameters within a design space. Rather than screen each factor individually against many different levels (values) for each remaining factor, a DOE scheme can be utilised to run only the experiments we need in order to generate analytical expressions for each capacitance.

Stack-Up:

Glass Cover Optical Clear Adhesive ITO Pattern Glass Substrate Copper Tape	Stack-Up: Glass-on-Glass	
	Thickness = 550 μm ,	Dielectric Constant = 7
	Thickness = 100 μm ,	Dielectric Constant = 3.5
	Diamond Pattern	
	Thickness = 550 μm ,	Dielectric Constant = 7
	Thickness = 508 μm ,	Dielectric Constant = 3.64

Fig. 3.53 Stack-up for snowflake design simulated.

The stack-up used is glass lens on a glass substrate separated by and OCA layer and bonded to 20 mils of grounded copper tape.

Pattern:

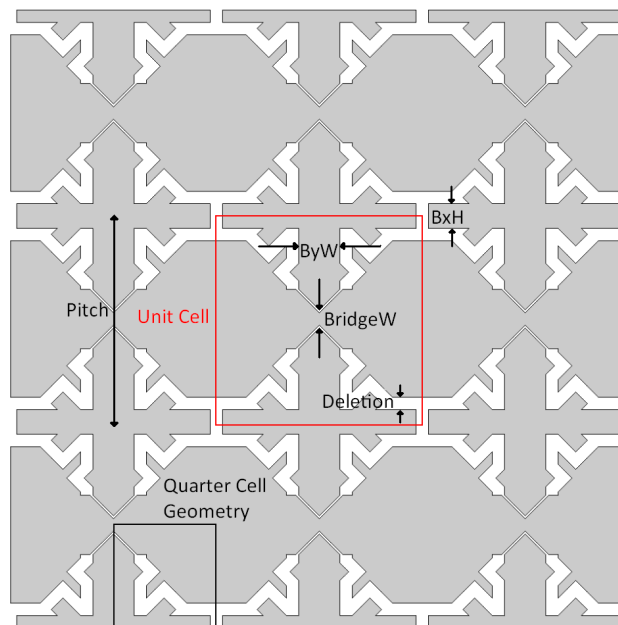


Fig. 3.54 Labeled pattern layout for snowflake.

The existence of non-linear behavior in the response of BxH and ByW with respect to Δcm has been noted in previous simulations. As a consequence, it is desirable to vary all parameters at once and observe the effect – as opposed to a single factor vs baseline value screening methodology. As the primary interest is in the panel design, the stack-up is frozen for these experiments with the exception of OCA thickness. This was identified as a high-impact parameter of the sensor type in advance of DOE simulations using the same screening analysis seen in previous chapters. The remaining factors in the DoE are the 5 panel parameters seen in figure 3.54, the snowflake pattern in question.

run	Factors							Responses									
	bridgeW	ByW	BxH	d	pitchX	T_Adhesive	Cm	Cm'	Cp-Tx	Cp-Rx	C-Tx-Tx	C-Rx-Rx	Cf-Tx	Cf-Rx	Cf-Tx-Tx	Cf-Rx-Rx	delCm
1	1.00E-04	0.001	3.50E-04	1.00E-04	0.005	1.50E-04	1.93928	1.64321	0.7665	0.36952	0.07331	0.03526	2.52075	1.14838	0.04313	0.03047	0.29607
2	1.00E-04	0.001	3.50E-04	2.00E-04	0.005	1.50E-04	1.38937	1.09113	0.72682	0.40635	0.05448	0.03184	2.37882	1.26372	0.03026	0.02553	0.29824
3	1.00E-04	0.0014	3.50E-04	1.00E-04	0.005	1.50E-04	1.91747	1.6139	0.71919	0.41815	0.06295	0.03755	2.36751	1.31979	0.03719	0.0316	0.30357
4	1.00E-04	0.0014	3.50E-04	2.00E-04	0.005	1.50E-04	1.41666	1.11398	0.68372	0.45085	0.04659	0.03468	2.23724	1.42123	0.026	0.02703	0.30268
5	3.00E-04	0.001	3.50E-04	1.00E-04	0.005	1.50E-04	1.8715	1.58297	0.77903	0.35698	0.07459	0.03485	2.56289	1.10574	0.04369	0.0303	0.28853
6	3.00E-04	0.001	3.50E-04	2.00E-04	0.005	1.50E-04	1.34689	1.05549	0.74134	0.39198	0.05607	0.03121	2.42797	1.21507	0.03098	0.02525	0.2914
7	3.00E-04	0.0014	3.50E-04	1.00E-04	0.005	1.50E-04	1.8532	1.55696	0.73507	0.40228	0.06447	0.03689	2.42115	1.26542	0.03784	0.03131	0.29624
8	3.00E-04	0.0014	3.50E-04	2.00E-04	0.005	1.50E-04	1.37687	1.08095	0.70173	0.43302	0.0484	0.03373	2.29976	1.36054	0.02683	0.02659	0.29592
9	2.00E-04	0.001	1.00E-04	1.50E-04	0.004	1.50E-04	1.15705	0.95842	0.50002	0.24136	0.08454	0.01486	1.87609	0.84498	0.05236	0.0109	0.19863
10	2.00E-04	0.001	1.00E-04	1.50E-04	0.006	1.50E-04	1.97386	1.63688	1.20971	0.39025	0.16442	0.01156	3.37947	1.07959	0.1185	0.00981	0.33698
11	2.00E-04	0.001	6.00E-04	1.50E-04	0.004	1.50E-04	1.1121	0.89372	0.43091	0.31254	0.03001	0.0558	1.62841	1.09119	0.01381	0.04528	0.21749
12	2.00E-04	0.001	6.00E-04	1.50E-04	0.006	1.50E-04	2.01245	1.61563	1.06113	0.54796	0.05173	0.05227	3.01579	1.57911	0.02969	0.04518	0.39682
13	2.00E-04	0.0014	1.00E-04	1.50E-04	0.004	1.50E-04	1.21654	1.00996	0.46642	0.27677	0.06916	0.01781	1.73403	0.98057	0.043	0.01242	0.20758
14	2.00E-04	0.0014	1.00E-04	1.50E-04	0.006	1.50E-04	2.00405	1.6495	1.14381	0.45859	0.14636	0.01277	3.23626	1.29186	0.10517	0.01044	0.35455
15	2.00E-04	0.0014	6.00E-04	1.50E-04	0.004	1.50E-04	1.15569	0.93761	0.40947	0.33453	0.02641	0.05869	1.53621	1.18016	0.0124	0.04679	0.21808
16	2.00E-04	0.0014	6.00E-04	1.50E-04	0.006	1.50E-04	2.00237	1.60174	1.00722	0.60292	0.04583	0.05421	2.89426	1.74773	0.02624	0.04616	0.40063
17	2.00E-04	0.0012	1.00E-04	1.00E-04	0.005	1.00E-04	1.89098	1.59995	0.81079	0.32135	0.14283	0.01292	3.00236	1.12794	0.09882	0.0106	0.29103
18	2.00E-04	0.0012	1.00E-04	1.00E-04	0.005	2.00E-04	1.84175	1.59406	0.81002	0.32134	0.138	0.01324	2.99669	0.90197	0.0951	0.01072	0.24769
19	2.00E-04	0.0012	1.00E-04	2.00E-04	0.005	1.00E-04	1.40262	1.10128	0.76759	0.36323	0.0957	0.01419	2.82444	1.27018	0.06102	0.01081	0.30134
20	2.00E-04	0.0012	1.00E-04	2.00E-04	0.005	2.00E-04	1.35478	1.0959	0.76657	0.36317	0.09416	0.01453	2.25937	1.01827	0.05966	0.01089	0.25888
21	2.00E-04	0.0012	6.00E-04	1.00E-04	0.005	1.00E-04	1.83597	1.50405	0.69999	0.43857	0.03941	0.06205	2.59957	1.55721	0.02092	0.05321	0.33192
22	2.00E-04	0.0012	6.00E-04	1.00E-04	0.005	2.00E-04	1.77608	1.4906	0.6994	0.43772	0.04183	0.061	2.07575	1.24255	0.02161	0.05243	0.28548
23	2.00E-04	0.0012	6.00E-04	2.00E-04	0.005	1.00E-04	1.36938	1.04422	0.67224	0.46317	0.03206	0.05273	2.48414	1.64065	0.01647	0.0423	0.32516
24	2.00E-04	0.0012	6.00E-04	2.00E-04	0.005	2.00E-04	1.3167	1.03433	0.67167	0.4622	0.03446	0.05157	1.9848	1.31107	0.01718	0.04151	0.28237
25	1.00E-04	0.0012	3.50E-04	1.00E-04	0.004	1.50E-04	1.39105	1.1729	0.44896	0.29616	0.04606	0.0399	1.68211	1.04743	0.02504	0.03228	0.21815
26	3.00E-04	0.0012	3.50E-04	1.00E-04	0.004	1.50E-04	1.33153	1.11909	0.46335	0.28176	0.04823	0.03877	1.74917	0.98171	0.02592	0.0318	0.21244
27	1.00E-04	0.0012	3.50E-04	1.00E-04	0.006	1.50E-04	2.4489	2.10162	1.11607	0.49252	0.09276	0.0343	3.16489	1.39663	0.06057	0.03038	0.38728
28	3.00E-04	0.0012	3.50E-04	1.00E-04	0.006	1.50E-04	2.41802	2.03996	1.1302	0.47841	0.09375	0.03403	3.19797	1.36158	0.06108	0.03026	0.37806
29	1.00E-04	0.0012	3.50E-04	2.00E-04	0.004	1.50E-04	1.04094	0.82415	0.4257	0.31706	0.03759	0.03173	1.58108	1.11819	0.01791	0.0277	0.21679
30	3.00E-04	0.0012	3.50E-04	2.00E-04	0.004	1.50E-04	1.01715	0.80517	0.44278	0.30009	0.03803	0.03525	1.6594	1.0436	0.01927	0.0268	0.21198
31	1.00E-04	0.0012	3.50E-04	2.00E-04	0.006	1.50E-04	1.80992	1.41928	1.0649	0.54043	0.06933	0.03047	3.03016	1.53487	0.04284	0.02532	0.39064
32	3.00E-04	0.0012	3.50E-04	2.00E-04	0.006	1.50E-04	1.76318	1.38086	1.08107	0.52449	0.07051	0.03008	3.06955	1.49594	0.04346	0.02514	0.38232
33	2.00E-04	0.001	3.50E-04	1.50E-04	0.004	1.00E-04	1.17719	0.94524	0.45923	0.28526	0.04389	0.03639	1.80435	1.10893	0.02332	0.02914	0.23195
34	2.00E-04	0.0014	3.50E-04	1.50E-04	0.004	1.00E-04	1.21721	0.9829	0.4319	0.31359	0.03664	0.04013	1.80435	1.23383	0.01964	0.03128	0.23431
35	2.00E-04	0.001	3.50E-04	1.50E-04	0.004	2.00E-04	1.13455	0.93702	0.45869	0.28474	0.04513	0.03611	1.56316	0.90031	0.023	0.02862	0.19753
36	2.00E-04	0.0014	3.50E-04	1.50E-04	0.004	2.00E-04	1.17686	0.97575	0.43134	0.31302	0.03783	0.03988	1.45874	1.00099	0.01938	0.0307	0.20111
37	2.00E-04	0.001	3.50E-04	1.50E-04	0.006	1.00E-04	2.12326	1.70825	1.12901	0.47874	0.08431	0.03181	3.58177	1.52737	0.05392	0.02769	0.41501
38	2.00E-04	0.0014	3.50E-04	1.50E-04	0.006	1.00E-04	2.13119	1.71047	1.06935	0.54004	0.07473	0.03339	3.43349	1.74131	0.0476	0.02851	0.42072
39	2.00E-04	0.001	3.50E-04	1.50E-04	0.006	2.00E-04	2.04132	1.68948	1.12829	0.47809	0.08605	0.03133	2.86977	1.21699	0.0543	0.0273	0.35184
40	2.00E-04	0.0014	3.50E-04	1.50E-04	0.006	2.00E-04	2.05393	1.69197	1.06859	0.53937	0.07615	0.03304	2.74748	1.38766	0.0479	0.0282	0.36196
41	1.00E-04	0.0012	1.00E-04	1.50E-04	0.005	1.00E-04	1.63555	1.33412	0.7826	0.34954	0.11539	0.01353	2.89054	1.22748	0.07664	0.01061	0.30143
42	1.00E-04	0.0012	6.00E-04	1.50E-04	0.005	1.00E-04	1.5834	1.25082	0.67714	0.46016	0.03445	0.05693	2.50808	1.63545	0.01803	0.047	0.33258
43	3.00E-04	0.0012	1.00E-04	1.50E-04	0.005	1.00E-04	1.58215	1.28878	0.79588	0.33634	0.1167	0.01323	2.9408	1.17729	0.07723	0.0105	0.29337
44	3.00E-04	0.0012	6.00E-04	1.50E-04	0.005	1.00E-04	1.53959	1.21409	0.69422	0.44317	0.03599	0.05587	2.57342	1.5704	0.01869	0.04645	0.3255
45	1.00E-04	0.0012	1.00E-04	1.50E-04	0.005	2.00E-04	1.58462	1.32674	0.78168	0.34954	0.1124	0.01388	2.30735	0.98329	0.07428	0.01071	0.25788
46	1.00E-04	0.0012	6.00E-04	1.50E-04	0.005	2.00E-04	1.52505	1.23803	0.67655	0.45926	0.03684	0.05586	2.00333	1.30628	0.01872	0.04622	0.28702
47	3.00E-04	0.0012	1.00E-04	1.50E-04	0.005	2.00E-04	1.53314	1.28219	0.79499	0.33631	0.11382	0.01354	2.34819	0.94243	0.0749	0.01059	0.25095
48	3.00E-04	0.0012	6.00E-04	1.50E-04	0.005	2.00E-04	1.48274	1.20116	0.69365	0.44226	0.03851	0.05473	2.05571	1.25356	0.01944	0.04564	0.28158
49	2.00E-04	0.0012	3.50E-04														

Tab. 3.12 DoE table for snowflake pattern.

A suitable DoE was chosen to capture the behavior observed in screening analysis – a 3-level 6-

factor design known as “Box-Behnken”[41]. There are advantages associated with choosing this over alternative fractional factorial designs. For one, it does not rely on the use of “star points”, points in the table corresponding to factor levels lying outside the experimental space of the DOE. It also minimizes the number of runs required compared to “Central Composite” designs in general.

To elaborate further, the central composite design is the most used response surface designed experiment. It is a fractional-factorial design with center points (like Box-Behnken) and a group of star points (unlike Box-Behnken). The purpose of these star points is to give a better estimation of response surface curvature. They are especially useful in sequential experiments as they allow the user to build on previous factorial experiments by adding star points at the user's discretion. They also have the added advantage of being rotatable (provide constant prediction variance at all points that are equidistant from the design center) and are often orthogonal, meaning that terms can be estimated independently. However, this design is not suitable for the TSP simulations in this work. This is due to the effect of start points as applied to TSP parameters such as Deletion and OCA thickness. Choosing to evaluate capacitance outside of the experimental domain of the DOE would have a negative impact on these simulations, as capacitive responses become increasingly non-linear as various stack-up layers and electrode separations decrease. Not only that, but the added simulation time due to meshing these thin layers would add a huge amount of time to an already lengthy DOE. Therefore, the Box-Behnken DOE scheme is much more desirable as it allows for faster simulations and preserves linearity within the experimental domain.

The data can now be fitted to a “least squares” model. This will fit the data points in the table to a polynomial equation which will consist of factors and/or combinations of factors and coefficients. The model will seek to minimize the residual between the predicted and actual data and will add more and more factors in order to do this if possible. Therefore, it is important to carefully scrutinize which factors are chosen to be included or excluded, as this approach can result in over-fitting of the data.

Modeling:

The models for each response are generated relatively quickly, however these can be further refined to create more efficient analytic equations. These models show the effect of each factor and gives the experimentalist an analytical equation for each response. In general, this approach can be used to predict all unit cell parameters (capacitances and resistances) and predict SNR Display and SNR Touch behaviour. We can also, in conjunction with further SPICE simulations estimate the settling

time for a given panel of a particular pitch and orientation and build a model for RC time constant, τ (hence the appearance of Rx-to-Rx and Tx-to-Tx capacitances appearing in the DoE table – these can be used in SPICE circuit model simulations).

ΔC_m Model

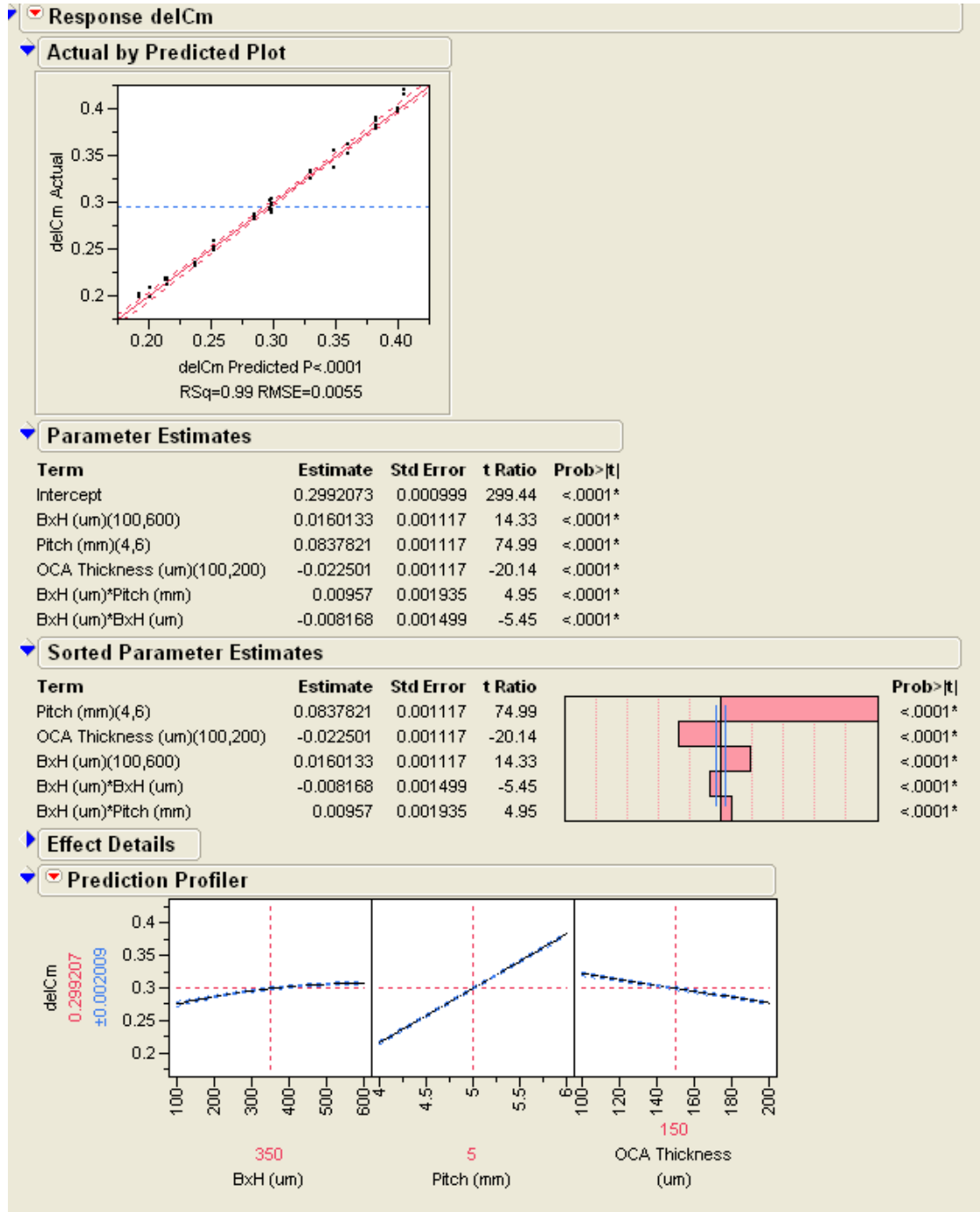


Fig. 3.55 JMP window view of the ΔC_m model created using the 6-factor 3-level Box-Behnken DoE.

Analytical Equation:

$$\begin{aligned} \Delta C_m = & 0.299 + 0.016 \frac{BxH - 350}{250} + 0.084 (P - 5) - 0.023 \frac{OCA_T - 150}{50} \\ & + \frac{BxH - 350}{250} 0.01 (P - 5) - 0.008 \left(\frac{BxH - 350}{250} \right)^2 \end{aligned} \quad (3.3)$$

where BxH is the x-bar height, P is the sensor pitch and OCA_T is the optically clear adhesive thickness.

C_m Model

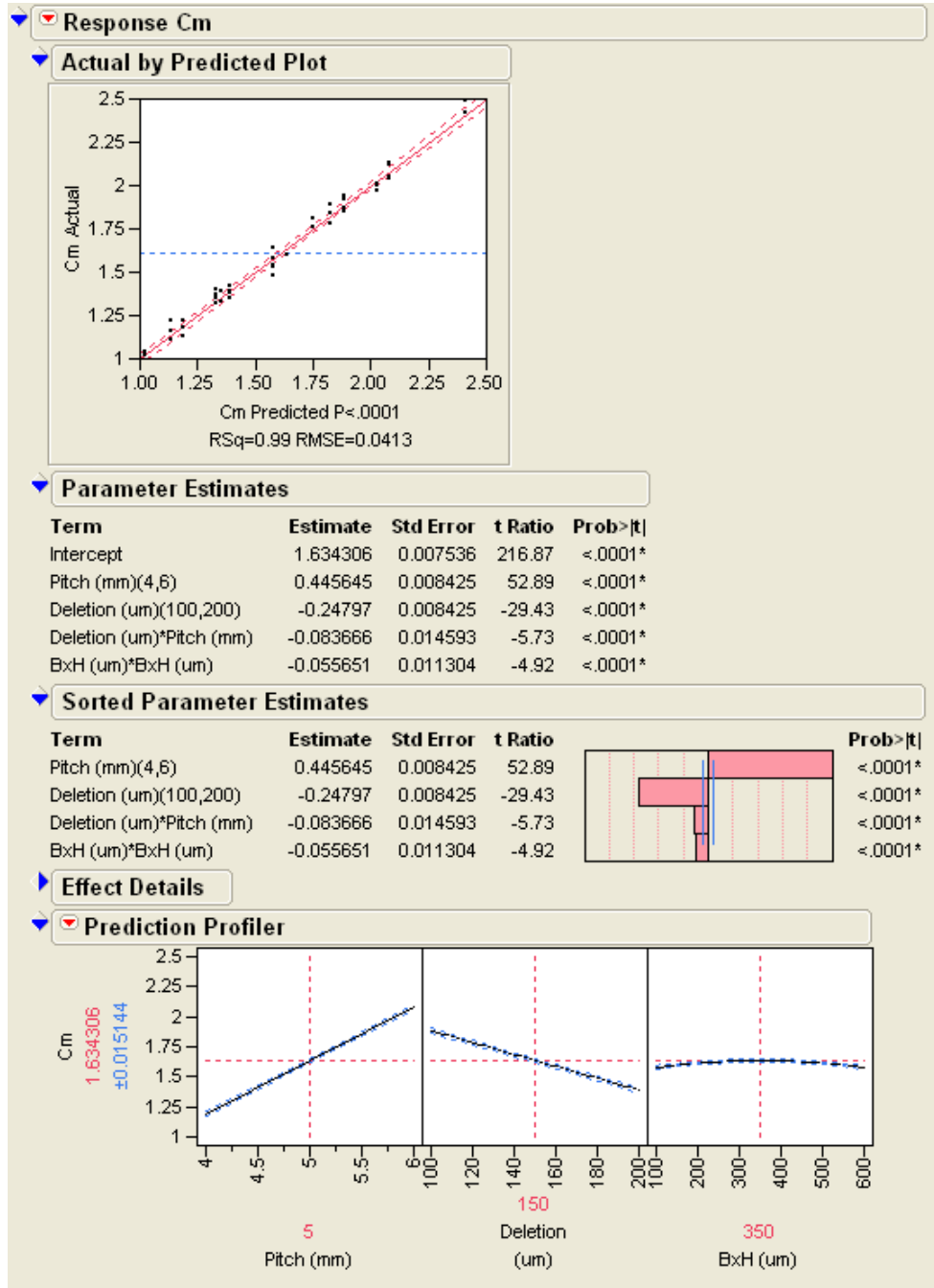


Fig. 3.56 JMP window view of the C_m model created using the 6-factor 3-level Box-Behnken DoE.

Analytical Equation:

$$C_m = 1.634 + 0.446(P - 5) - 0.248\left(\frac{D - 150}{50}\right) - 0.084\left(\frac{D - 150}{50}\right)(P - 5) - 0.056\left(\frac{BxH - 350}{250}\right)^2 \quad (3.4)$$

where P is the sensor pitch, BxH is the x-bar height and D is the thickness of the ITO deletion region between the electrodes.

C_m' Model

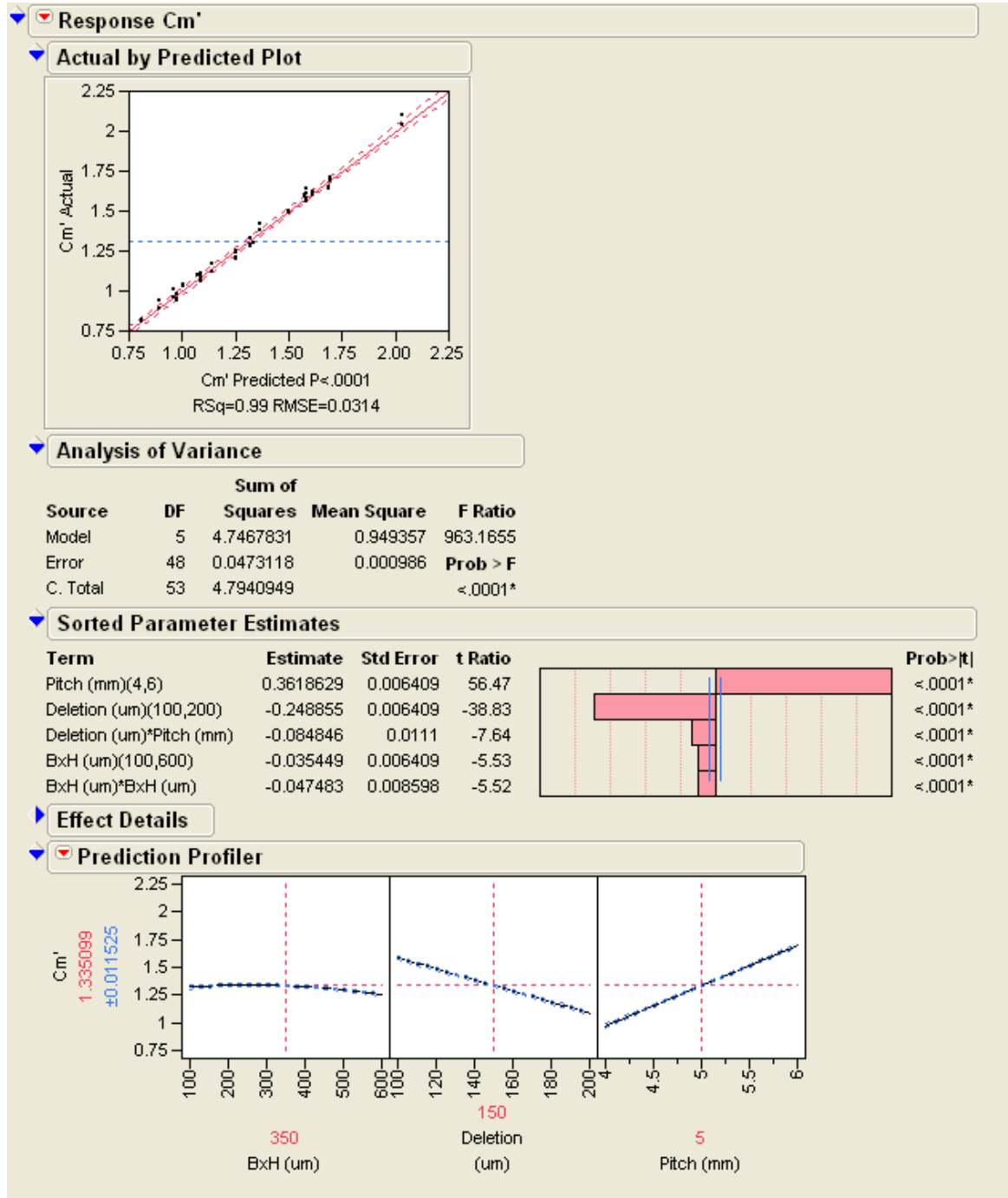


Fig. 3.57 JMP window view of the C_m' model created using the 6-factor 3-level Box-Behnken DoE.

Analytical Equation:

$$\begin{aligned}
 C_m' = & 1.335 - 0.035 \left(\frac{BxH - 350}{250} \right) - 0.249 \left(\frac{D - 150}{50} \right) + 0.362 (P - 5) \\
 & - 0.085 \left(\frac{D - 150}{50} \right) (P - 5) - 0.047 \left(\frac{BxH - 350}{250} \right)^2
 \end{aligned} \quad (3.5)$$

where BxH is the x-bar height, D is the thickness of the ITO deletion region between the electrodes and P is the sensor pitch.

C_{pTX} Model

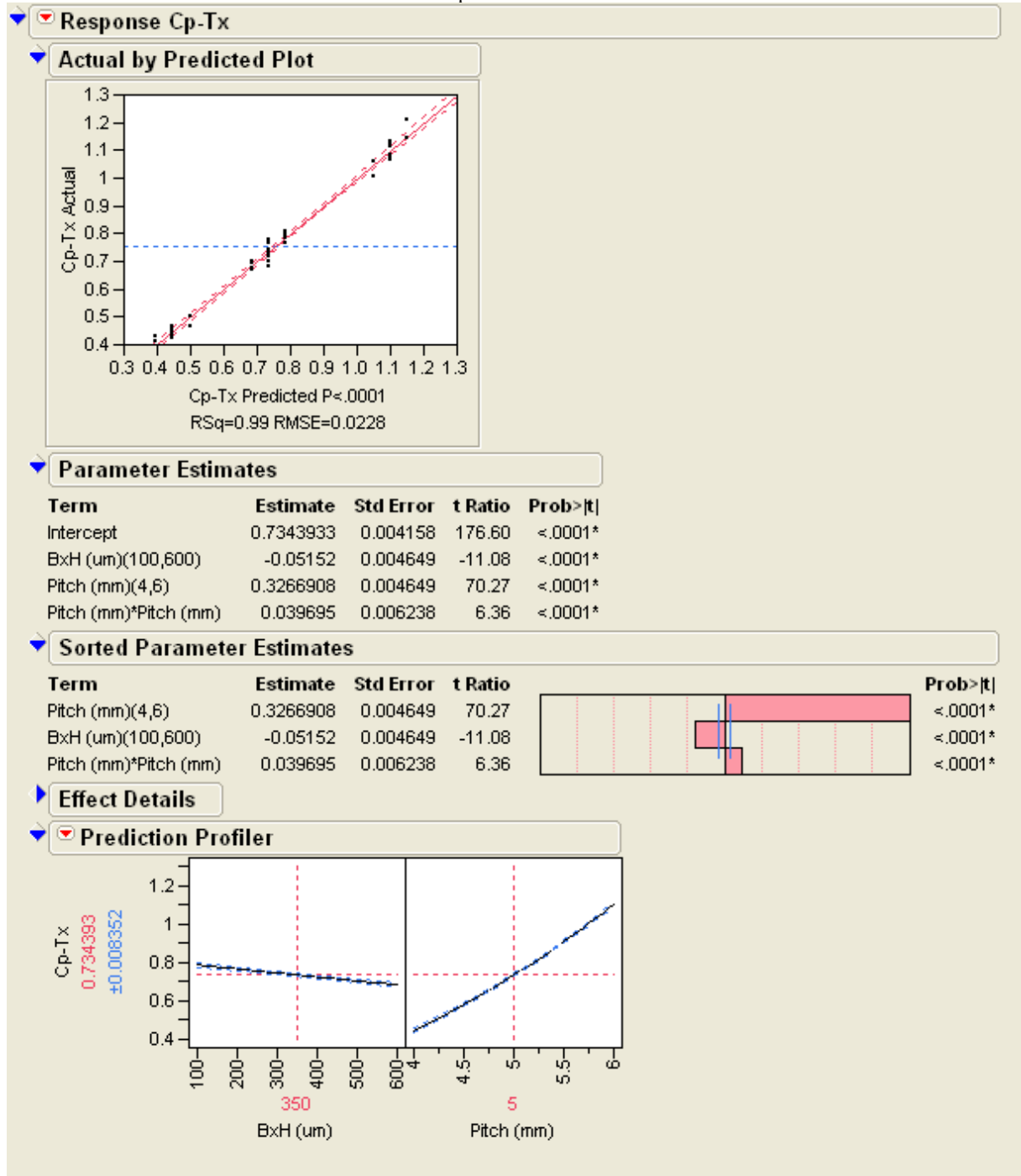


Fig. 3.58 JMP window view of the C_{pTX} model created using the 6-factor 3-level Box-Behnken DoE.

Analytical Equation:

$$C_{pTX} = 0.734 - 0.0515 \left(\frac{BxH - 350}{250} \right) + 0.327(Pitch - 5) + 0.04(Pitch - 5)^2 \quad (3.6)$$

where *BxH* is the x-bar height and *P* is the sensor pitch.

C_{pRX} Model

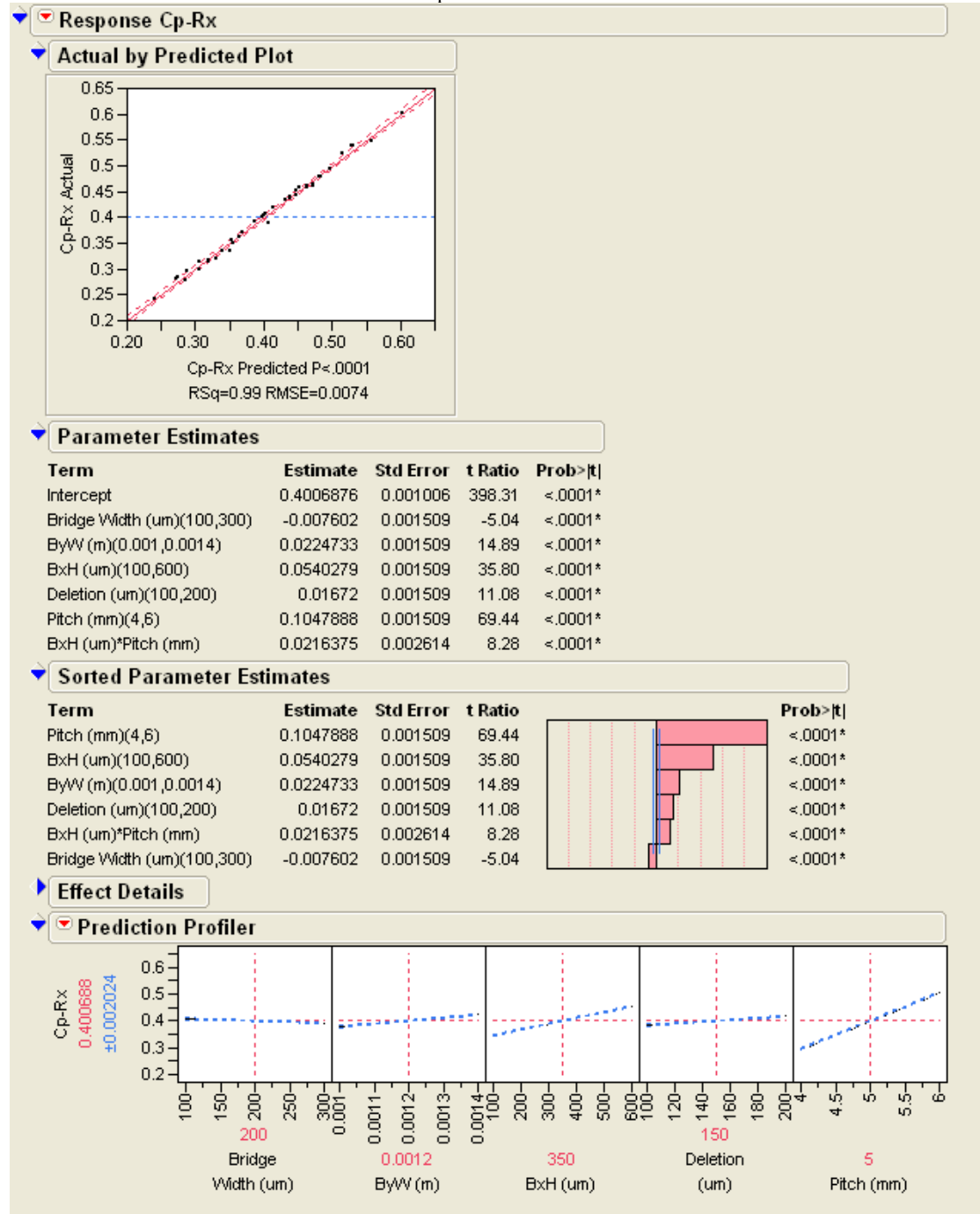


Fig. 3.59 JMP window view of the C_{pRX} model created using the 6-factor 3-level Box-Behnken DoE.

Analytical Equation:

$$\begin{aligned}
 C_{pRX} = & 0.401 + -0.008 \left(\frac{B_w - 200}{100} \right) + 0.0225 \left(\frac{ByW - 0.001}{0.0002} \right) + 0.054 \left(\frac{BxH - 350}{250} \right) \\
 & + 0.017 \left(\frac{D - 150}{50} \right) + 0.105 (Pitch - 5) + 0.0216375 \left(\frac{BxH - 350}{250} \right) (P - 5)
 \end{aligned} \quad (3.7)$$

where B_w is the ITO bridge width, ByW is the y-bar width, BxH is the x-bar height, D is the thickness of the ITO deletion region between the electrodes and P is the sensor pitch.

C_{ITX} Model

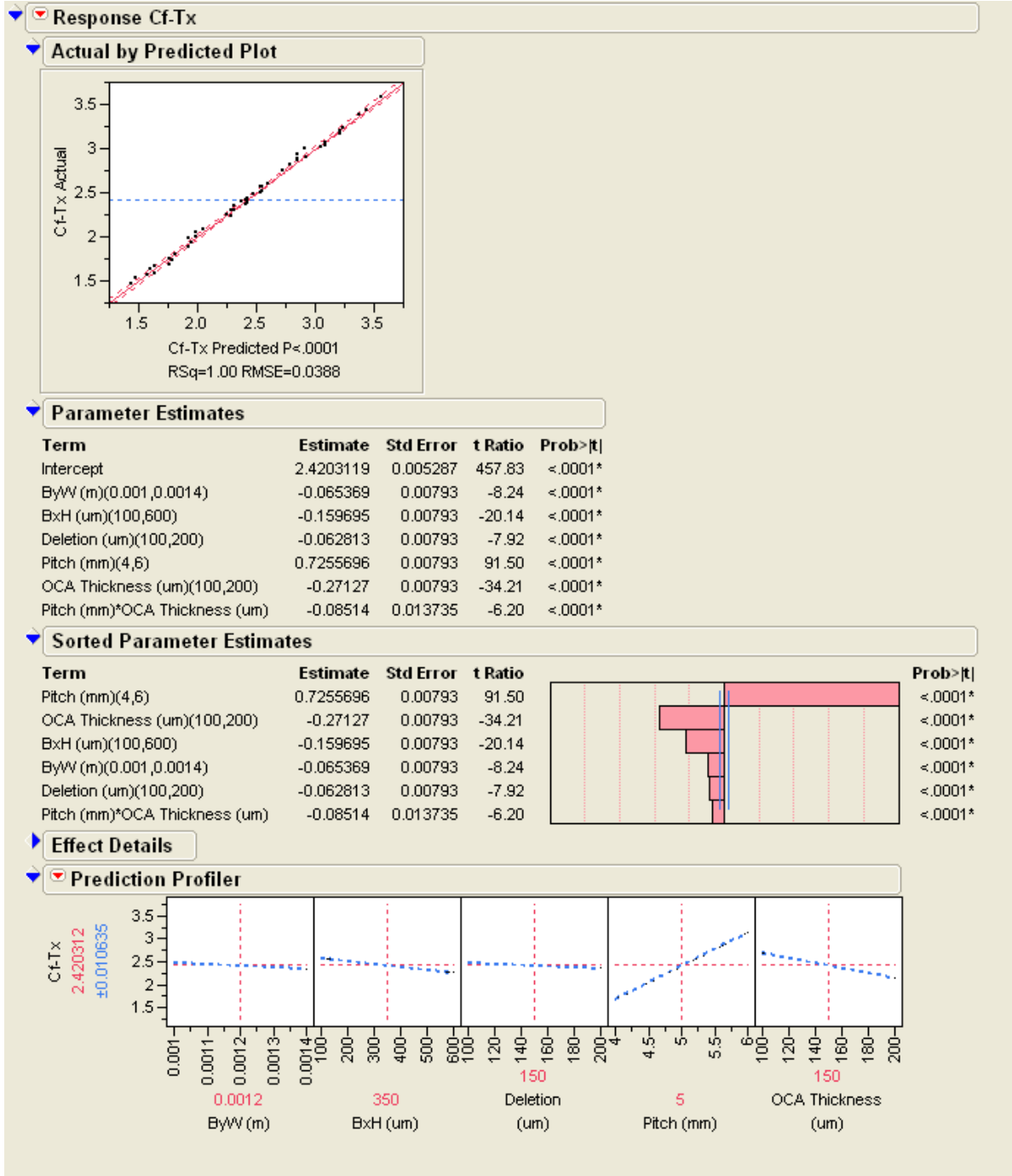


Fig. 3.60 JMP window view of the C_{ITX} model created using the 6-factor 3-level Box-Behnken DoE.

Analytical Equation:

$$\begin{aligned}
 C_{ITX} = & 2.420 - 0.065 \left(\frac{ByW - 0.001}{0.0002} \right) - 0.16 \left(\frac{BxH - 350}{250} \right) - 0.063 \left(\frac{D - 150}{50} \right) \\
 & + 0.726(P - 5) - 0.271 \left(\frac{OCA_T - 150}{50} \right) - 0.08514(P - 5) \left(\frac{OCA_T - 150}{50} \right)
 \end{aligned} \quad (3.8)$$

where ByW is the y-bar width, BxH is the x-bar height, D is the thickness of the ITO deletion region between the electrodes, OCA_T is the optically clear adhesive thickness and P is the sensor pitch.

C_{RX} Model

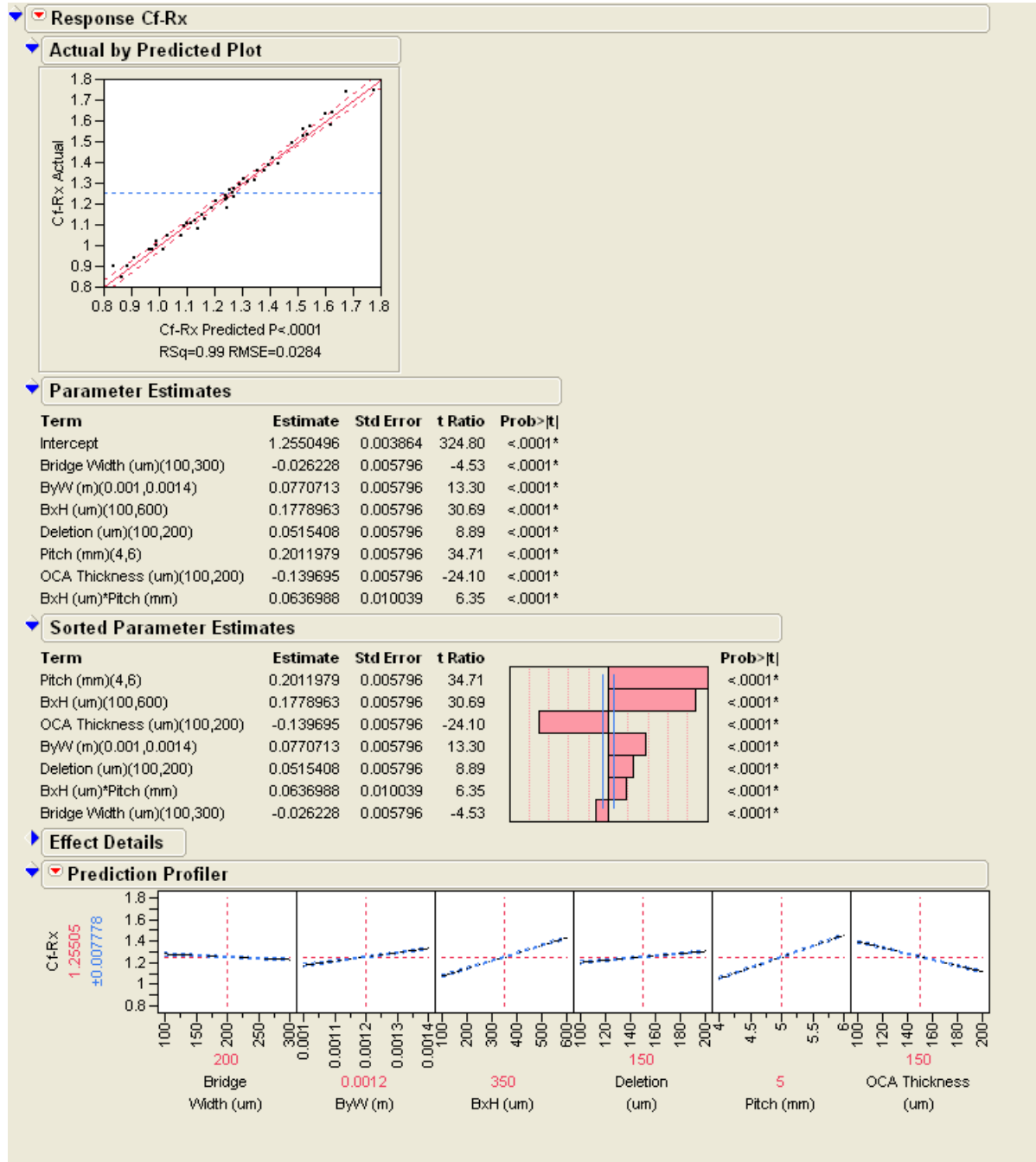


Fig. 3.61 JMP window view of the C_{RX} model created using the 6-factor 3-level Box-Behnken DoE.

Analytical Equation:

$$\begin{aligned}
 C_{RX} = & 1.255 - 0.026 * \left(\frac{B_w - 200}{100} \right) + 0.077 \left(\frac{ByW - 0.0012}{0.0002} \right) + 0.178 \left(\frac{BxH - 350}{250} \right) \\
 & + 0.0515 \left(\frac{D - 150}{50} \right) + 0.202 (P - 5) - 0.14 \left(\frac{OCA_T - 150}{50} \right) + 0.0637 \left(\frac{BxH - 350}{250} \right) (P - 5)
 \end{aligned} \quad (3.9)$$

where B_w is the ITO bridge width, ByW is the y-bar width, BxH is the x-bar height, D is the thickness of the ITO deletion region between the electrodes, P is the sensor pitch and OCA_T is the optically clear adhesive thickness.

Figures 3.55, 3.56, 3.57, 3.58, 3.59, 3.60, and 3.61, give the statistical models generated by the JMP software. The standard error and t-ratios for each parameter are given and it is noteworthy that in each case the uncertainty of each parameter is less than the impact it has on the response being modeled. An experimentalist is able to simultaneously adjust the sliders seen in each factor vs response plot and view the resultant response according to the analytical equation instantly. The analytical equations themselves have been extracted manually and accompany each model figure below. These can be seen as equations 3.3, 3.4, 3.5, 3.6, 3.7, 3.8, and 3.9.

Now that this analysis is complete, the need for additional simulations for this particular stack-up and pattern type has been effectively eliminated. Instead of running time consuming simulations, the experimentalist need only apply the empirical equation for each response according to the design specifications (pitch, deletion, BxH, etc). However, it is worth mentioning that the DOE itself is time consuming in its nature. Using only a 54-run scheme, at a solve time of 10 minutes per run of a 3x3 snowflake geometry, 9 hours of simulation time was required. Added to planning time, screening analysis, final model building and sweep programming the total time investment for the experimentalist comes in at 12 hours at least – more than a full working day. A full factorial design for a 6-factor 3-level design would've constituted 729 runs. Completing this DOE would've taken almost 14 working days. It is obvious why a fractional-factor design was chosen. The solving times involved serve to illustrate the need for prudent decision making when it comes to determining if a DOE study should be run. A recommendation to pursue empirical equations for a sensor through DOE methodology should only be under the condition that the benefits of the study outweigh the consumption of the manpower and computational resources required.

3.7 MOVING FINGER

This work demonstrates the effect of a moving finger in TSP simulations. In general, the finger is modeled as a grounded cylinder resting at the glass interface above the intersection of the Rx and Tx electrodes. However, in reality the location of the finger is variable within the unit cell. The location of the finger also changes the ΔC_m response. With this in mind, simulations can be designed which give a continuous profile of the critical parameters according to finger position. This means that not only can simulations predict which unit cell (intersection of electrodes) a touch occurs in, they can determine where in the unit cell the touch takes place. Figure 3.62 gives the 3D geometry of the 5x5 snowflake design used.

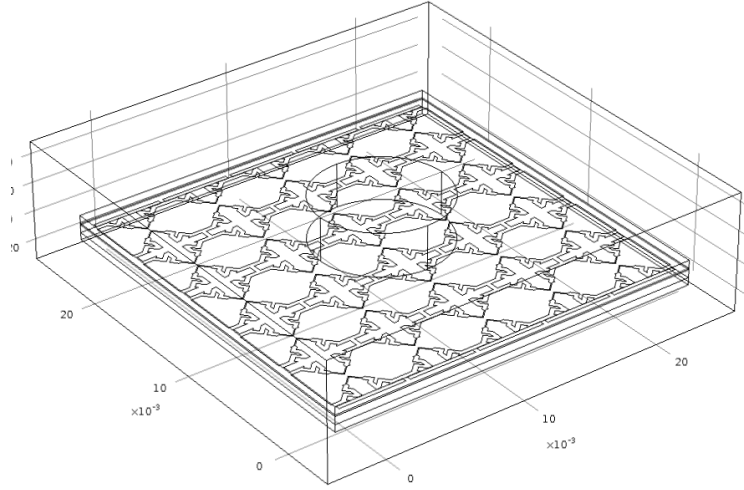
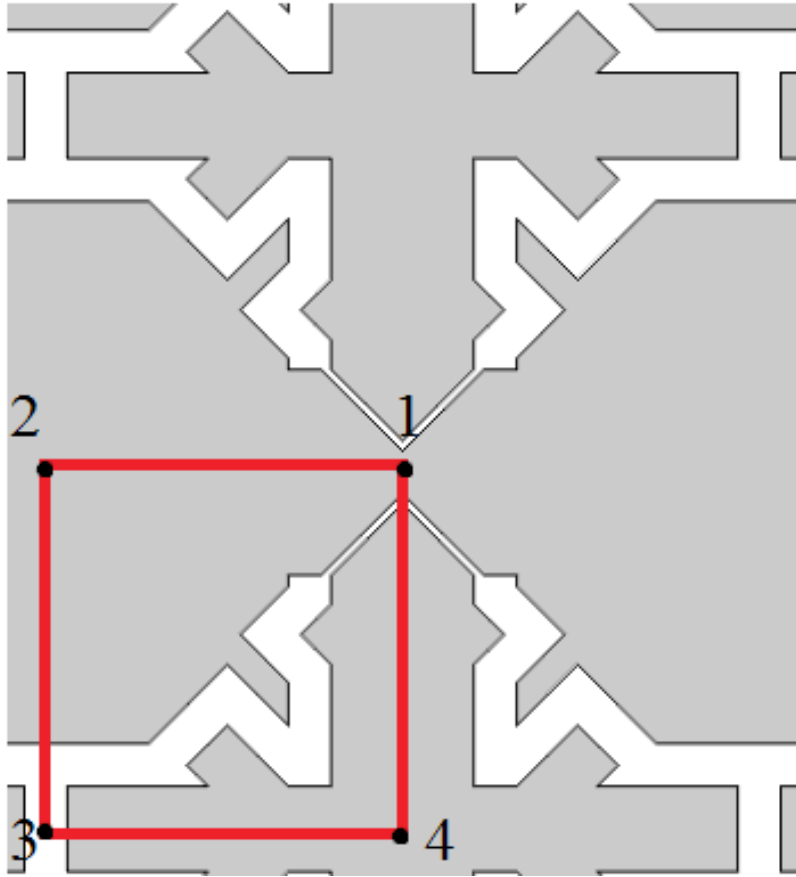


Fig. 3.62 5x5 3D geometry for the snowflake panel on GG stack-up.

The methodology for this experiment involves the use of axisymmetry. Firstly, the unit cell (snowflake pattern) was divided into quarters. A sweep was designed whereby the x-y coordinates of the 7mm finger were manipulated so as to trace a path covering the perimeter of the quarter-cell geometry. Figure 3.63 shows the path of the finger layed out by the parametric sweep. This sweep resulted in the dataset seen in table 3.13. Using the symmetry of the geometry and electrode activations, this data was rearranged into 4 distinct paths which give a full-pitch profile of responses for the TSP unit cell. Tables 3.14, 3.15, 3.16 and 3.17 show this data. Figures 3.65, 3.66, 3.67 and 3.68 give the response profiles. The four cross-sensor full-pitch paths are shown in figure 3.64.



FingX	FingY	Original Dataset		
		Cm	Cf-Tx	Cf-Rx
0.00938	0.01	0.85401	2.37254	1.66508
0.00875	0.01	0.85497	2.3165	1.63568
0.00813	0.01	0.86142	2.28144	1.55566
0.0075	0.01	0.87772	2.26933	1.41285
0.0075	0.00938	0.8798	2.24506	1.39117
0.0075	0.00875	0.88599	2.17238	1.33944
0.0075	0.00813	0.89649	2.05518	1.28326
0.0075	0.0075	0.9162	1.89038	1.25442
0.00813	0.0075	0.89856	1.90407	1.37437
0.00875	0.0075	0.88886	1.9422	1.44986
0.00938	0.0075	0.88317	1.98789	1.49337
0.01	0.0075	0.88124	2.00844	1.5076
0.01	0.00813	0.8604	2.21147	1.54857
0.01	0.00875	0.85457	2.33232	1.61414
0.01	0.00938	0.85398	2.38905	1.6541
0.01	0.01	0.85395	2.40534	1.67172

Fig. 3.63 Path of the finger swept out in moving finger simulations. Finger begins and ends at 1.

Tab. 3.13 Resulting dataset from moving finger.

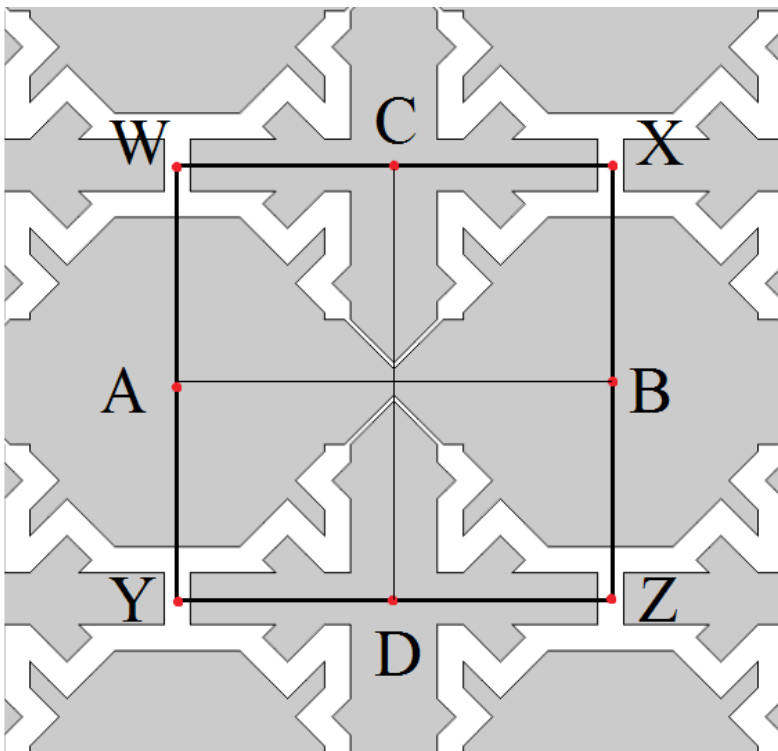


Fig. 3.64 The 4 distinct finger paths are completed by moving the finger (1) AB, (2) CD, (3) WX/YZ, (4) WY/XZ. In the datasets these paths are referred to as (1) Horizontal Centre, (2) Vertical Centre, (3) Horizontal Edge and (4) Vertical Edge.F.

Horizontal Centre (AB)		
FingX (pitch)	delCm (pF)	SNRt (unity)
0	0.25228	0.1785610645
1/8	0.26858	0.1726469794
1/4	0.27503	0.1681441358
3/8	0.27599	0.1657517957
1/2	0.27605	0.1651293279
5/8	0.27599	0.1657517957
3/4	0.27503	0.1681441358
7/8	0.26858	0.1726469794
1	0.25228	0.1785610645

Tab. 3.14 Rearranged data forms the horizontal centre path.

Horizontal Edge (WXYZ)		
FingX (pitch)	delCm (pF)	SNRt (unity)
0	0.2138	0.1704373336
1/8	0.23144	0.1683971565
1/4	0.24114	0.1663195067
3/8	0.24683	0.1652838881
1/2	0.24876	0.1650039798
5/8	0.24683	0.1652838881
3/4	0.24114	0.1663195067
7/8	0.23144	0.1683971565
1	0.2138	0.1704373336

Tab. 3.15 Rearranged data forms the horizontal edge path.

Vertical Centre (CD)		
FingY (pitch)	delCm (pF)	SNRt (unity)
0	0.24876	0.1650039798
1/8	0.2696	0.1740961016
1/4	0.27543	0.1706357565
3/8	0.27602	0.1668702013
1/2	0.27605	0.1651293279
5/8	0.27602	0.1668702013
3/4	0.27543	0.1706357565
7/8	0.2696	0.1740961016
1	0.24876	0.1650039798

Tab. 3.16 Rearranged data forms the vertical centre path.

Vertical Edge (WY/XZ)		
FingY (pitch)	delCm (pF)	SNRt (unity)
0	0.2138	0.1704373336
1/8	0.23351	0.1819662422
1/4	0.24401	0.182173147
3/8	0.2502	0.1798486166
1/2	0.25228	0.1785610645
5/8	0.2502	0.1798486166
3/4	0.24401	0.182173147
7/8	0.23351	0.1819662422
1	0.2138	0.1704373336

Tab. 3.17 Rearranged data forms the vertical edge path.

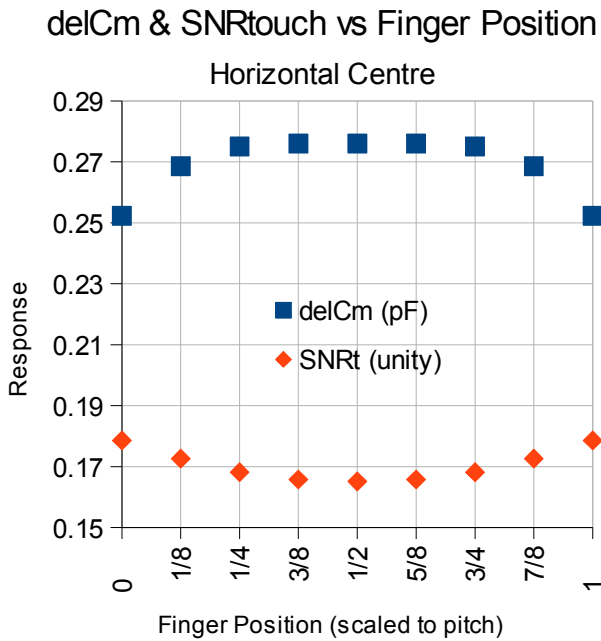


Fig. 3.65 ΔC_m and SNR_{TOUCH} responses as a function of finger position for the horizontal centre path.

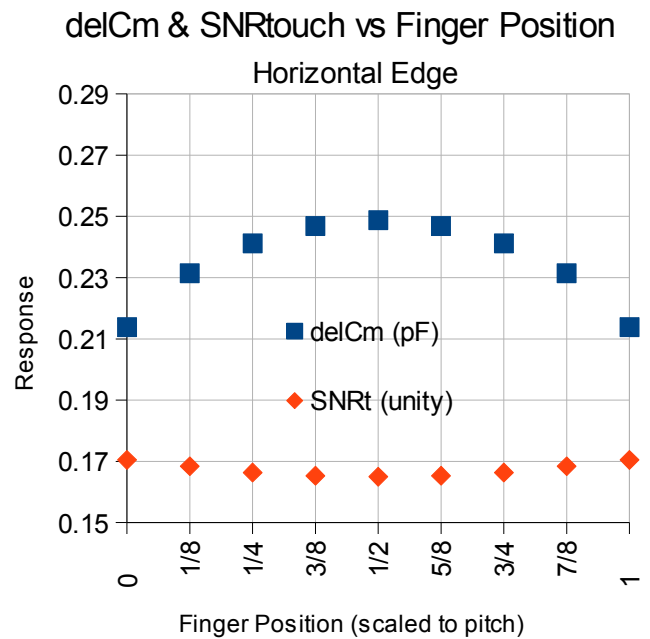


Fig. 3.66 ΔC_m and SNR_{TOUCH} responses as a function of finger position for the horizontal edge path.

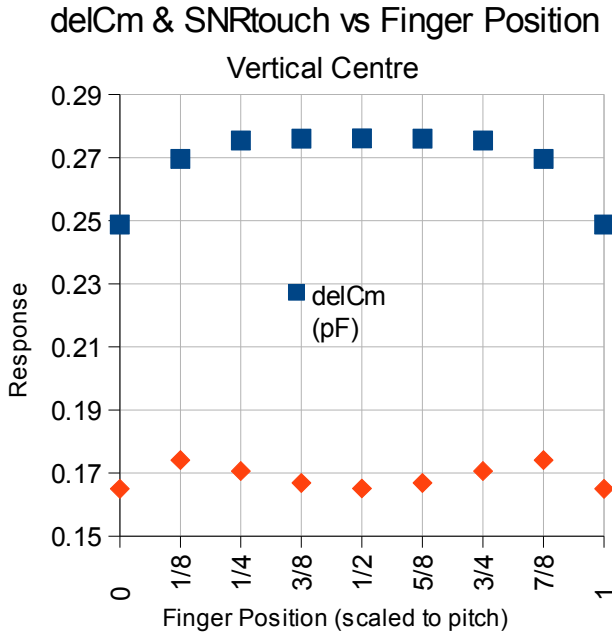


Fig. 3.67 ΔC_m and SNR_{TOUCH} responses as a function of finger position for the vertical centre path.

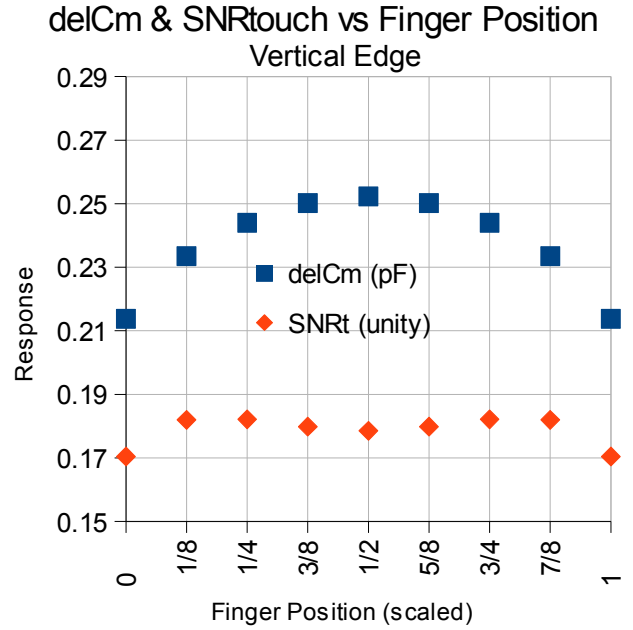


Fig. 3.68 ΔC_m and SNR_{TOUCH} responses as a function of finger position for the vertical edge path.

Upon inspection of the 4 finger path profiles obtained, it can be concluded that a response “map” of the unit cell can be constructed. However, the resolution of any map constructed would be poor and only describe the points on the paths taken. However, there is no limit to the number of paths that could be programmed into the parametric sweep – apart from time. In this way, a complete response map of the entire unit cell could be obtained. This information could be supplied to the the chip as tuning parameters for touch detection algorithms. While the quarter-cell symmetry creates 3 ghost points for each touch, the touch location can always be detected by analysing the capacitances of adjacent electrodes, thus eliminating the ghost points.

Obtaining the same data without the use of quarter-cell symmetry would have take 2.8 times longer to complete (16 finger locations to 45 finger locations). Verifying these results would've been possible by carrying out the full set of 45 finger locations. However, a more time efficient way to check for good symmetry is to compare a few mirrored pair locations in preliminary simulations. Eight runs would be enough to confirm good symmetry before proceeding with the remaining 15, thus saving roughly half the time in the long run with symmetry validation testing.

In conclusion, this work has served to illustrate how finger position studies could provide tuning data for touch sensing controllers. However and more importantly, they tell the designer about the

degradation in signal and signal-to-noise ratio at the limits of the unit cell. This is a core component of good TSP sensor design and any sensor which reaches critically low values for either is not worth building.

CHAPTER 4

CONCLUSIONS

The purpose of this thesis is to answer the research questions: “What key metrics characterize a good TSP?” and “How can TSP designs be optimized using computer simulations?”

Upon review of the most recent simulation techniques it is the view of this thesis that FEM and MOM will remain the dominant methods of TSP simulation for many years to come, as alternative hybrid techniques typically provide a small increase in accuracy at the cost of a large increase in simulation time. In an industry of hundreds if not thousands of designs, applications, vendors, customers and emerging technologies a simulation is no good, no matter how accurate, if it can't be done in a reasonable time frame within which a designer has the space to modify, redesign and optimize the application.

The key metrics of ΔC_m , SNR and τ have all been defined. Evidence of their importance can be found throughout this document. ΔC_m is the physical quantity responsible for the operation of all capacitive TSPs. SNR is crucial to touch detection circuitry and its measurement can provide engineers with insights into the difficulties of detecting a touch. The RC time constant characterizes the settling time of the panel and hence the maximum scan rate of the TSP. This information is paramount when configuring the timing block scheme for the full panel circuit. This is all information that can be calculated via simulation methodology without building a single real-life sensor. Powerful simulation techniques allow engineers to quickly evaluate designs and determine these key metrics.

The optimization of these simulations has been the subject of huge experimental endeavor in this work. FEM and MOM models have been validated against an empirical equation. Stack-ups for identical ITO patterns have been compared via screening analysis and the advantages and disadvantages have been determined. The same can be said for ITO patterns of identical stack-ups. It has been demonstrated that a snowflake variation on the classic diamond design offers distinct advantages in both sensitivity and SNR, despite its complex geometry. Empirical equations for the full capacitive matrix of the snowflake design were formulated using a DOE methodology and the importance of using a computationally non-exhaustive approach has been highlighted. It was demonstrated that MOM and FEM exhibit high agreement in the calculation of capacitances for a

typical TSP. This serves to underline the consistency of the simulation methodology and increases the experimentalist's confidence in it. It has even been shown how the subtle discrepancy in sensitivity within the unit cell can predict the exact location of a touching finger within the unit cell. These are some of the ways an engineer can optimize a TSP design using a computer simulation.

There were several unique contributions to the area of touch-screen simulation made in the course of this work. Never before has a DOE methodology been linked to FEM simulations. This methodology can be extended to emerging panel designs of high complexity in order to fast-track their appearance in the marketplace. With the right planning and agreement between vendors to freeze certain design parameters analytical equations generated by DOEs could eventually take the place of exhaustive simulation methodology, just as simulations once replaced exhaustive prototype testing. The use of axisymmetry is a well-known technique in the simulation of elastic materials among structural engineers. However, this is the first time it has been used in an electrostatic TSP simulation. Using this approach in moving finger simulations increases the unit-cell sensitivity resolution dramatically based on the principle that the more time is saved, the more data points can be collected within a limited amount of time. This is important as it allows for better touch detection through tuning data. Also, this work explored the effect of increasing simulation size which had not yet been investigated elsewhere. It provides the first benchmark in terms of reasonable computing constraints which will need to be addressed in order to achieve good convergence and the large simulation domains required.

Future work could be undertaken in the area of FEM vs MOM efficiency analysis to determine the optimal TSP simulation technique for a modern machine. In this work identical machines will run identical panel simulations and parameter sweeps using FEM and MOM. The comparison would also include the effect of increasing the domain size, from 3x3 to 5x5 to 7x7 etc. Only in this way could the superior method be determined with respect to TSP simulations. The refinement of hybrid techniques such as FEM-DBCI method could lead to improvements in computational efficiency. The possibility of using cloud-computing resources in order to increase the solution speed is also a worthwhile pursuit. Additionally, significant increases in computational resources would present a huge range of research possibilities. High resolution finger position studies could provide extremely detailed sensitivity data to the chip, allowing for ultra-fine tuning and touch resolution. Full-panel simulations would allow engineers to test individual electrode columns and rows within a full sensor layout instead of just the idealized central electrode case. This would allow for a high-precision comparison between simulation and prototype panels. Full-factor DOE projects would be

extremely useful to designers, as these are currently extremely time-consuming tasks with potentially huge benefits. Full-factorial DOEs could yield incredibly accurate numerical models which could characterize entire sensor designs instantly and dominate sensor design process flow.

Ultimately, the optimisation of a simulation is dependent on the management of limited resources available to the engineer. For every project undertaken there is a limited amount of time to complete the task, a limited amount of computational resources, a limited number of parameters that can be varied and a limited number of sweeps that can be made. The nature of simulations is that there is a constant tension between convergence and simulation time and best way an engineer can optimize his simulation is by making an informed decision based on all the information available to him. The trick is to be able to access the information when you need it by building up a vast repertoire of techniques, such as the techniques outlined in this research thesis.

CHAPTER 5

REFERENCES

- [1] G. T. Carlson and B.L. Illman, *Am. J. Phys.* 62, 1099 (1994).
- [2] Jianming Jin. “The finite element method in electromagnetics”. ISBN: 978-0-471-43818-2. June 2002, Wiley-IEEE Press.
- [3] S. P. Hotelling and B. R. Land, “Double-sided touch-sensitive panel with shield and drive combined layer,” U.S. Patent 7 920 129 B2, Apr. 5, 2011.
- [4] S. H. Bae et al., “Integrating multi-touch function with a large-sized LCD,” in *Soc. Inf. Display Symp. Dig.*, May 2008, vol. 39, no. 1, pp. 178–181.
- [5] R. Adler and P. J. Desmares, “An economical touch panel using SAW absorption,” *IEEE Trans. Ultrason. Ferroelectr. Freq. Control*, vol. UFFC-34, no. 2, pp. 195–201, Mar. 1987.
- [7] K. Lim et al., “A fast and energy efficient single-chip touchcontroller for tablet touch applications,” *J. Display Technol.*, vol. 9, no. 7, pp. 520–526, Jul. 2013.
- [8] I. Baharav and R. Kakarala, “Capacitive touch sensing: signal and image processing algorithms,” in *Proc. SPIE Conf. on Computational Imaging*, San Francisco, CA, USA, Jan. 2011.
- [9] T. Hwang et al., “A highly area-efficient controller for capacitive touch screen panel systems,” *IEEE Trans. Consum. Electron.*, vol. 56, no. 2, pp. 1115–1122, Jul. 2010.
- [10] Y. H. Tai et al., “Large-area capacitive active touch panel using the method of pulse overlapping detection,” *J. Display Technol.*, vol. 9, no. 3, pp. 170–175, Mar. 2013.
- [11] J. Y. Ruan et al., “A multi-touch interface circuit for a large-sized capacitive touch panel,” in *Proc. IEEE Sensors Conf.*, Nov. 2010, pp. 309–314.
- [12] M. Trend et al., “Electrode layout for touch screens,” U.S. Patent 2 011/0 025 639 A1, Feb. 3, 2011.
- [13] J. A. Harley, “Capacitive touch screen or touchpad for finger or stylus,” U.S. Patent 2010/0 026 655 A1, Feb. 4, 2010.
- [14] J. Lee, M. T. Cole, J. Chi Sun Lai, and A. Nathan. “An Analysis of Electrode Patterns in Capacitive Touch Screen Panels”. *IEEE Journal of Display Technology*, vol. 10, no. 5, May 2014, p 362 – 366.
- [15] S. Kim, W. Choi, W. Rim, Y. Chun, H. Shim, H. Kwon, J. Kim, I. Kee, S. Kim, S. Lee, and J. Park. “A highly sensitive capacitive touch sensor integrated on a thin-film-encapsulated active-matrix OLED for ultrathin displays”. *IEEE Transactions on electron devices*, vol. 58, no. 10, October 2011, p 3609 – 3615.
- [16] D.-U. Jin, T.-W. Kim, H.-W. Koo, D. Stryakhilev, H.-S. Kim, S.-J. Seo, M.-J. Kim, H.-K. Min, H.-K. Chung, and S.-S. Kim, “Highly robust flexible AMOLED display on plastic substrate with new structure,” *Soc. Inf. Display (SID) Symp. Dig.*, vol. 47, no. 1, pp. 703–705, May 2010.
- [17] S. An, J. Lee, Y. Kim, T. Kim, D. Jin, H. Min, H. Chung, and S. S. Kim, “2.8-inch WQVGA flexible AMOLED using high performance low temperature polysilicon TFT on plastic substrate,” *Soc. Inf. Display (SID) Symp. Dig.*, vol. 47, no. 2, pp. 706–709, May 2010.
- [18] S. Kim, H.-J. Kwon, S. Lee, H. Shim, Y. Chun, W. Choi, J. Kwack, D. Han, M. Song, S. Kim, S. Mohammadi, S. Kee, and S. Y. Lee, “Low-power flexible organic light-emitting diode display device,” *Adv. Mater.* [Online]. Available: <http://onlinelibrary.wiley.com/doi/10.1002/adma.201101066/full>
- [19] H. Shim, I. Kee, S. Kim, Y. Chun, H. Kwon, Y. Jin, S. Lee, D. Han, J. Kwack, D. Kang, H. Seo, M. Song, M. Lee, and S. Kim, “A new seamless foldable OLED display composed of multi display panels,” *Soc. Inf. Display (SID) Symp. Dig.*, vol. 41, no. 1, pp. 257–260, May 2010.
- [20] H. Kwon, H. Shim, S. Kim, W. Choi, Y. Chun, I. Kee, and S. Lee, “Mechanically and optically reliable folding structure with a hyperelastic material for seamless foldable displays,” *Appl. Phys.*

Lett., vol. 98, no. 15, pp. 15 194–15 196, Apr. 2011.

[21] M. Noda, N. Kobayashi, M. Katsuhara, A. Yumoto, S. Ushikura, R. Yasuda, N. Hirai, G. Yukawa, I. Yagi, K. Nomoto, and T. Urabe, “A rollable AM-OLED display driven by OTFTs,” Soc. Inf. Display (SID) Symp. Dig., vol. 41, no. 1, pp. 710–713, May 2010.

[22] S. Pietri, A. Olmos, M. Berens, A. V. Boas, and M. Goes, “A fully integrated touch screen controller base on 12b 825 kS/s SAR ADC,” in Proc. EAMTA, May 2008, vol. 39, no. 1, pp. 178–181.

[23] W. Buller and B. Wilson, “Measurement and modeling mutual capacitance of electrical wiring and humans,” IEEE Trans. Instrum. Meas., vol. 55, no. 5, pp. 1519–1522, Oct. 2006.

[24] Introduction to Capacitive Sensing, Microchip Technol. Inc., Chandler, AZ, 2007. [Online]. Available: <http://ww1.microchip.com/downloads/en/AppNotes/01101a.pdf>

[25] Capacitive Touch Sensors, Fujitsu Microelectron., Langen, Germany, 2010. [Online]. Available: <http://www.fujitsu.com/downloads/MICRO/fme/articles/fujitsu-whitepaper-capacitive-touch-sensors.pdf>. Accessed on 30/06/2014.

[26] H. Morimura, S. Shigematsu, and K. Machida, “A novel sensor cell architecture and sensing circuit scheme for capacitive fingerprint sensors,” IEEE J. Solid-State Circuits, vol. 35, no. 5, pp. 724–731, May 2000.

[27] G. Aiello, S. Alfonzetti, G. Borzi, E. Dilettoso and N. Salerno. “Comparing the FEM-BEM and FEM-DBCI for open-boundary electrostatic field problems”. Eur. Phys. J. Appl. Phys. Vol. 39, p 143 – 148 (2007).

[28] T. Steinmetz, N. Godel, G. Immer, M. Clemens, S. Kurz, and M. Bebandorf, “Efficient symmetric FEM-BEM coupled simulation of electro-quasistatic fields,” IEEE Trans. Magn., vol. 44, no. 6, pp. 1346–1349, Jun. 2008.

[29] S. Alfonzettia and N. Salerno, “A non-standard family of coundary elements for the hybrid FEM-BEM method,” IEEE Trans. Magn., vol. 45, no. 3, pp. 1312–1315, Mar 2009.

[30] G. Aiello, S. Alfonzetti, E. Dilettoso, and N. Salerno, “An iterative solution to FEM-BEM algrbraic systems for open boundary elevtrostatic problems,” IEEE Trans, Magn., vol. 43, no. 4, pp. 1249–1252, Apr. 2007.

[31] G. Aiello, S. Alfonzetti, G. Borzi, E. Dilettoso, and N. Salerno, “Efficient solution of skin-effect problems by means of the GMRES-Accelerated FEM-BEM method,” IEEE Trans. Magn., vol. 44, no. 6, pp. 1274–1277, Jun. 2008.

[32] V. M. Machado, “FEM/BEM hybrid method for magnetic field evaluation due to underground power cables,” IEEE Trans. Magn., vol. 46, no. 8, pp. 2876–2879, Aug. 2010.

[33] H. T. Yu, S. L. Ho, M. Q. Hu, and H. C. Wong, “Edge-based FEM-BEM for wide-band electromagnetic computation,” IEEE Trans. Magn., vol. 42, no. 4, pp. 771–774, Apr. 2006.

[34] G. Aiello, S. Alfonzetti, G. Borzi, E. Diletoso, and N. Salerno, “A modified FEM-DBCI method for static and quasi-static electromagnetic field problems” IEEE Trans. Magn. Vol. 46, no. 8, pp. 2803–2806, Aug. 2010.

[35] G. Aiello, S. Alfronzetti, and N. Salerno, “Improved selection of integration surface in the hybrid FEM-DCBI method,” IEEE Trans. Magn., vol. 46, no. 8, pp. 3357 – 3360, Aug. 2010.

[36] G. Aiello, S. Alfronzetti, E. Diletoso, and N. Salerno, “Improving the accuracy of the integral equation in the hybrid FEM-DBCI method for open boundary electrostatic problems,” IEEE Trans. Magn., vol. 42, no. 4, pp. 579–582, Apr. 2006.

[37] S. Alfronzetti, G. Aiello, E. Diletoso, and N. Salerno, “Numerical implementations of the FEM-DBCI integral equation,” COMPEL, vol. 27, no. 4, pp. 879–886, 2008.

[38] L. Shiqoung, W. Zezhong, P. Chao, “FEM-ACTual Charge Method for open boundary electrostatic fields,” Electromagnetic field problems and applications (ICEF), 2012 sixth international conference on, pp. 1–4, 19–21 June 2012.

[39] P. Bettles, “Infinite Elements,” Int. J. Numer. Methods Eng., vol. 11, pp. 53–64. 1977.

- [40] Charles S. Walker. "Capacitance, Inductance, and CrossTalk Analysis". ISBN-10: 0890063923. May 1990, Artech House.
- [41] George Box, "Statistics for experimenter: design, Innovation and Discovery," ISBN-10: 0471718130. Wiley IEEE Press, May 31, 2005.